The Multiple-Reflection Time-of-Flight Isobar Separator for TITAN and Direct Mass Measurements at the FRS Ion Catcher

von

Christian Jesch

aus Frankfurt am Main

Inaugural-Dissertation zur Erlangung des Doktorgrades der Naturwissenschaften

Zusammenfassung

Hochpräzise Massenmessungen an exotischen Nukliden sind unter anderem wegen ihrer Beiträge zur Aufklärung der Struktur des Kerns, zur Entwicklung von Massenmodellen sowie zum Verständnis und zur Modellierung von astrophysikalischen Nukleosyntheseprozessen wichtig. Bisherige Produktions-, Präparations- und Messmethoden für exotische Nuklide sind durch isobare Kontamination, ihren Bedarf an Messzeit sowie Anzahl der produzierten Kerne limitiert. Neben vorhandenen Optionen zur Umgehung der Limitierungen existiert eine neue Option, Multireflexions Flugzeitmassenspektrometrie (MR-TOF-MS). Im Rahmen dieser Arbeit wird ein neuartiges Gerät zur Isobarenseparation und zur direkten Massenspektrometrie an einer ISOL Einrichtung präsentiert sowie die erste direkte Massenmessung mit einem MR-TOF-MS an einer In-Flight Einrichtung.

Das TITAN MR-TOF-MS wird an ISAC des kanadischen TRIUMF zur Erzeugung von isobarenreinen Strahlen, als komplementäres Verfahren zur Massenmessung sehr kurzlebiger Nuklide und zur Optimierung des Aufbaus verwendet werden. Dargestellt werden das Konzept des Geräts sowie sein Aufbau, Inbetriebnahme und erste Ergebnisse in Deutschland und in Kanada. Bisher wurde ein Massenauflösungsvermögen (FWHM) von 47.000 sowie ein Separationsvermögen von 14.000 erreicht.

Durch Verdopplung der kinetischen Energie auf den Designwert sowie weitere Optimierung wird eine Massenauflösung von 100.000 sowie ein Separationsvermögen von 50.000 erreicht werden. Nach seiner Integration in das TITAN System wird das MR-TOF-MS einen wichtigen Beitrag zu Experimenten mit exotischen Kernen an TITAN liefern. Unter anderem sind Messungen an neutronenreichen Cadmium Isotopen in Planung.

Weiterhin wird der FRS Ion Catcher beschrieben. Als Pilotexperiment zum Niederenergie-Zweig LEB des Super-FRS der im Aufbau befindlichen Beschleunigeranlage FAIR wird hier die Anwendung eines MR-TOF-MS zur direkten Massenmessung von kurzlebigen, schweren Nukliden gezeigt. Im Rahmen dieser Arbeit wurden die Massen von ^{213}Fr und ^{213}Rn gemessen, hierbei ist dies die erste direkte Massenmessung von ^{213}Rn, einem Nuklid mit $19,5\,$ms Halbwertszeit. Erreicht wurde eine Genauigkeit von $1.2 \cdot 10^{-6}$ mit nur 27 gemessenen Teilchen.

Mit der entwickelten Datenauswertungsmethode und Verbesserungen an Elektronik und Einstellungen sind Genauigkeiten von $3 \cdot 10^{-7}$ in Reichweite. Messungen an exotischen Nukliden sind geplant, ebenso werden die Erkenntnisse zur Finalisierung des Designs der LEB-Instrumente verwendet.

Abstract

Highly accurate mass measurements of exotic nuclides are relevant for the investigation of the structure of the nucleus, the development of mass models and to understand and model astrophysical nucleosynthesis processes. Production, preparation and measurement methods for exotic nuclides are limited by isobaric contamination, required measurement time and number of produced particles. A new alternative to existing methods to circumvent these limitations exists: Multiple-reflection time-of-flight mass spectrometry (MR-TOF-MS). In this thesis, a novel device for isobar separation and direct mass measurement at an ISOL facility will be presented as well as first direct mass measurements of an MR-TOF-MS at an in-flight facility.

The TITAN MR-TOF-MS will produce isobarically clean beams, used as a complementary method for mass measurement of very short-lived nuclides and for optimization of the setup. The concept of the device will be presented as well as its design, commissioning and first results achieved in Germany and in Canada. A mass resolving power of $47,000$ and a separation power of $14,000$ have been reached.

By doubling the kinetic energy to its design value and further optimization, a mass resolving power of $100,000$ and a separation power of $50,000$ will be reached. After its integration into the TITAN setup, the MR-TOF-MS will play an important role in experiments with exotic nuclides in the TITAN setup. Measurements of neutron rich cadmium isoptopes are planned.

Furthermore, the FRS Ion Catcher is described. As a pilot experiment for the low-energy branch of the Super-FRS of the future facility FAIR, the direct mass measurement of short-lived, heavy nuclides is presented. In the scope of this thesis, the masses of ^{213}Fr and ^{213}Rn were measured. This is the first direct mass measurement of ^{213}Rn, a nuclide with a half-life of $19,5\,$ms. An accuracy of $\cdot 10^{-6}$ with just 27 measured particles has been achieved.

With the developed data evaluation method and improvements in the electronics and settings of the system, accuracies of $3 \cdot 10^{-7}$ are in reach. Measurements on exotic nuclides are planned, findings from the performed measurement will be used to finalize the design of the instruments of the LEB.

Contents

1. Introduction

Mass measurements of exotic nuclides are important because of their contributions to develop mass models, fundamental symmetry studies and astrophysical nucleosynthesis modeling. Established methods for high precision mass measurement are Penning trap, storage ring measurements and several others. In this thesis, a novel method, based on a multiple-reflection time-of-flight mass spectrometer (MR-TOF-MS), is presented and applied to precision mass measurement of exotic nuclides and their separation for other experiments, for example mass-selective decay spectroscopy.

Exotic nuclides are produced in nuclear reactions at accelerator facilities by fusion, fission, spallation and fragmentation reactions. These reactions produce a large variety of nuclides, not only the ones of interest. Therefore, separation is required after the production. For ISOL facilities, this separation is performed by magnetic mass separators. Their resolving power is typically sufficient to remove most contaminants but not the isobaric ones. To enhance the selectivity, various efforts are made, for example to combine mass separators with laser ionization or chemical methods, in order to provide mono-isotopic samples of ions, which are free of isobaric contaminants. At in-flight facilities, separation by projectile fragment separators allows separation of one species. To perform the mass measurement, either storage ring methods have to be employed or the ions have to be stopped in gas and transported into further measurement systems.

While Penning traps are very well understood and provide reliable high-accuracy measurements, they have a few shortcomings in terms of the required number of ions and the time required for a measurement. Methods like charge breeding or phase imaging TOF-ICR allow to mitigate these problems to some degree. A different and new approach is MR-TOF-MS which allows to perform mass spectrometry typically on the millisecond timescale as opposed to the tenth seconds timescales of Penning traps. Additionally, MR-TOF-MS can be used as a separator for beam purification for subsequent instruments.

This thesis deals with a novel MR-TOF-MS for isobar separation and direct mass measurement at an ISOL facility and first direct mass measurements performed with an MR-TOF-MS at an in-flight facility.

The first device is an instrument developed for the TITAN setup at TRIUMF's ISAC. It will be used as an isobar separator in order to provide cleaned beams for the various experiments. Additionally, direct mass spectrometry for very short-lived nuclides is possible. In this work, its design, setup and commissioning are

presented.

The second device is the MR-TOF-MS at the FRS Ion Catcher experiment. Here, the application of the instrument for the first direct mass measurement of short-lived heavy nuclides is shown.

2. Foundations of Modern Mass Spectrometry on Exotic Nuclides

2.1. The Interest in Mass Spectrometry of Exotic Nuclides

Thomson and Aston were able to measure masses of a large number of the naturally occurring elements including their isotopes [Aston, 1922]. The Whole Number Law, stating that the masses of atoms are multiples of the mass of a hydrogen atom, was found [Aston, 1920]. With improving spectrometers, a slight deviation from this rule was found. The masses appeared too low, this difference was called the mass defect [Eddington, 1920]. With the discovery of the neutron [Chadwick, 1932] it became apparent that the mass of the atom ^A_ZX can be written as

$$m\left(A, Z\right) = Z \cdot m_p + (A - Z) \cdot m_n - E_{B\mathrm{nuc}}/c^2 + Z \cdot m_e - E_{B\mathrm{e}}/c^2 \qquad (2.1)$$

with Z the number of protons and N the number of neutrons, $A = Z + N$ the mass number, m_p, m_n and m_e the masses of the proton, neutron and the electron respectively and $E_{B\mathrm{nuc}}$ and $E_{B\mathrm{e}}$ the binding energies for nucleons and electrons, respectively.

The binding energies reflect all interactions of the nucleons and electrons and therefore the Hamiltonian of these bound nuclear or atomic systems. Measurements of a series of nuclides with high accuracy allows information to be gained about binding energies and, by consequence, of the Hamiltonian in question.

The first approach to model the nuclear binding energies is the semi-empirical mass formula of Bethe and Weizsäcker [Weizsäcker, 1935]. Based on the macroscopic assumption of an electrically charged liquid drop, it assumes a force that scales with the volume ($a_{\mathrm{vol}}A$). On the surface, fewer nucleons are in reach to interact with, lessening the binding force ($a_{\mathrm{sf}}A^{2/3}$). Due to the positive charge of the protons, a repelling Coulomb term is needed as well ($\propto Z^2 A^{-1/3}$). As first quantum-mechanic modification, an asymmetry term ($a_{\mathrm{sym}}A$) and a pairing term (Δ_n, Δ_p) are added, resulting in the full formula of

Parameter		
a_{vol}	-15.697550	MeV
a_{sf}	17.662690	MeV
a_{sym}	26.308165	MeV
a_{ss}	-17.003132	MeV
r_0	1.221897	fm
δ	-1.250000	MeV
e^2	1.43985	MeVfm

Table 2.1.: Parameters for the Bethe-Weizsäcker formula derived by fitting the AME 2003 mass values with $N, Z \geq 8$ [Pearson, 2007].
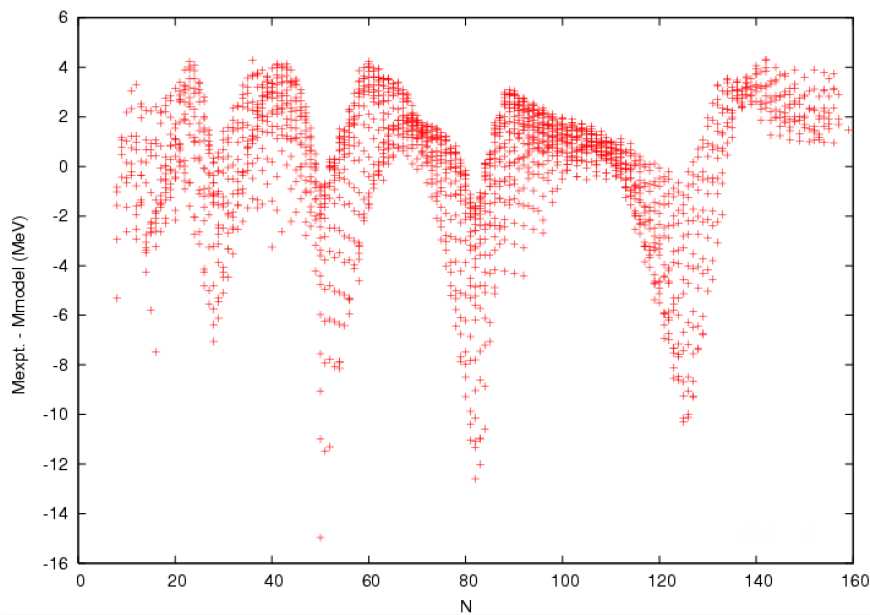
Figure 2.1.: Difference of measured mass and mass predicted by the Bethe-Weizsäcker formula in dependence on the neutron number for the AME 2003 nuclides with $N, Z \geq 8$. This reflects the microscopic contributions not considered in the Bethe-Weizsäcker formula, namely formation of shells [Pearson, 2007].

$$E_{B\mathrm{nuc}} = a_{\mathrm{vol}}A + a_{\mathrm{sf}}A^{2/3} + \frac{3e^2}{5r_0}Z^2A^{-1/3} + \left(a_{\mathrm{sym}}A + a_{\mathrm{ss}}A^{2/3}\right)I^2 + \Delta_n + \Delta_p \quad (2.2)$$

with $I = (N - Z)/A$, $\Delta_{n,p} = \pm\delta$ respectively for N and Z even or odd and including the modification of the asymmetry term by Myers and Swiatecki. By fitting a large number of measured masses, the free parameters of the Bethe-Weizsäcker formula can be determined, see Table 2.1 [Pearson, 2007].

While the Bethe-Weizsäcker approach already predicts quite a few effects correctly and is a rather good approximation, it has its limits. By subtracting
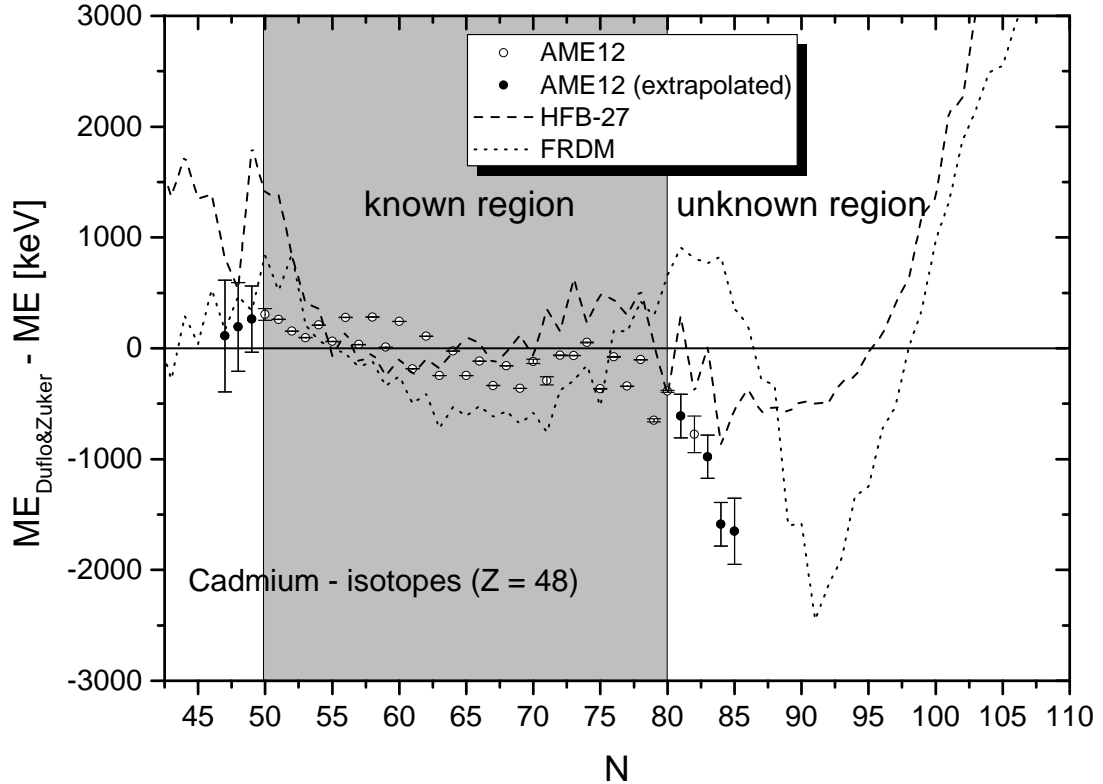
Figure 2.2.: Deviation of the AME12 values and the predictions of two selected models in relation to the Duflo-Zuker model. In the region of known masses, the models show good agreement. Where masses are unknown the models quickly deviate from each other, showing the need for experimental data [Diwisch, 2015].

the values generated by the Bethe-Weizsäcker formula from the measured values and plotting against the number of protons or neutrons, it can be seen in Figure 2.1 that the deviations from the liquid drop model have a systematic behavior. These observable shell closures suggest the need for more advanced, quantum-mechanical models.

Since solutions for ab-initio models currently are not possible in sufficient precision for larger nuclides [Pearson, 2007], semi-empirical approaches have to be employed. These can be grouped in combinations of the macroscopic Bethe-Weizsäcker model with microscopic corrections (Finite-Range-Droplet Model – FRDM [Möller et al., 1988]) and in simplification of sets of processes into mean fields (Hartree-Fock-Bogoliubov – HFB [Bender et al., 2003]).

Both approaches need experimental data in order to determine the parameters used in the respective model. The absence of data soon leads to deviations of the models from each other, signifying lower reliability as can be seen in Figure 2.2. Therefore, especially exotic nuclides are important for model improvement.

Without mass models, information about the shell structure can be gained by

Explosive Nucleosynthesis

$S_p = 0$

r-Process

rp-Process

^{100}Sn

Superheavy
Elements

$S_n = 0$

Locations of
p- and n-Driplines

Shell Structure
far-off Stability

Z

N

New Decay Modes
like 2p-Emission

Structure of Exotic Nuclides

Halo- and
Skin Nuclides
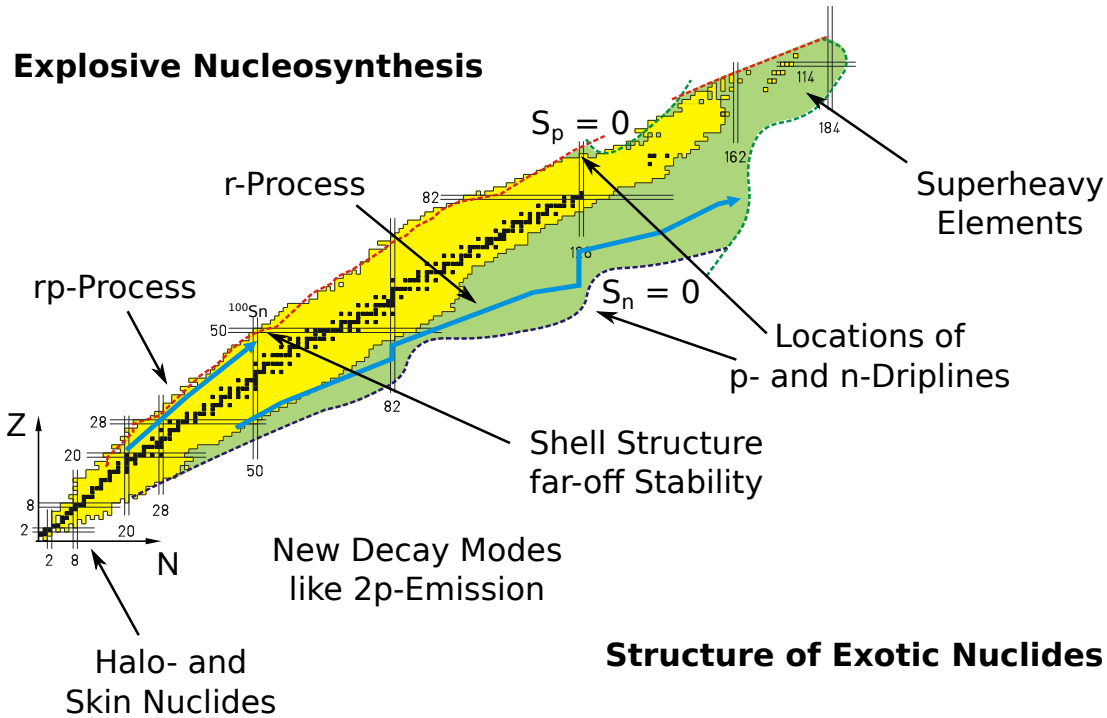
Figure 2.3.: Chart of Nuclides showing the measured nuclides in yellow and pre-
dicted nuclides in green. Shown as well are the areas of interest in
nuclear astrophysics and nuclear structure.

plotting sequences of two-proton and two-neutron separation energies for se-
quences of nuclides. Of interest are strength and location of shell gaps for exotic
nuclides. New decay modes like two proton emission become possible far off
stability.

Aside from the fundamental interest in understanding the structure of the nu-
cleus, reliable mass values are of high importance for nuclear astrophysics. Here,
modeling the processes in nucleosynthesis requires precise binding energies in or-
der to correctly portray the process path and therefore gain information about
the genesis of the elements making up our Universe. The explosive synthesis
mechanisms r- and rp-process mostly proceed in very exotic regions [Burbidge
et al., 1957, Wallerstein et al., 1997].

These areas of interest in nuclear masses can be seen in Figure 2.3.

2.2. Production of Exotic Nuclides – Radioactive Ion Beam Facilities

The basic production reactions for exotic nuclides in the laboratory are neutron
capture, nucleon transfer, spallation, fragmentation, fission, fusion-evaporation

Figure 2.4.: Schematic diagram of different approaches to produce radioactive ion beams. In ISOL, the reaction happens in a thick target which stops the produced nuclides. They are afterward extracted, ionized and separated by mass. For in-flight, the nuclides are produced in a thin target where the momentum after the reaction is sufficient to transport the ion to a momentum, velocity, energy loss separator or combinations of these. Hybrid methods catch the nuclides after in-flight production in matter [Fulton, 2011].

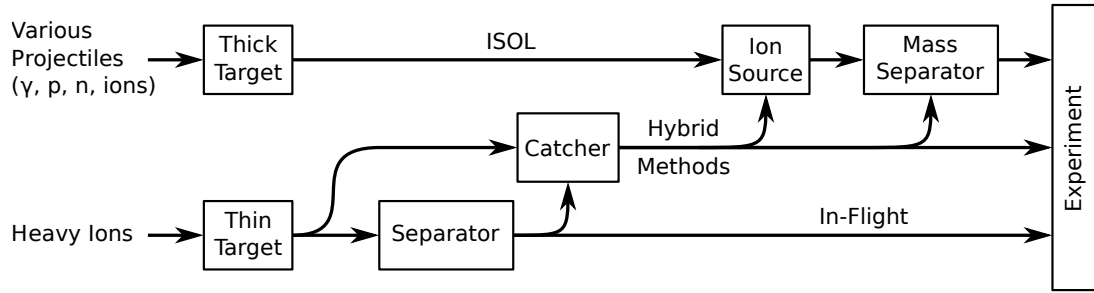and combinations of these reactions [Blaum, 2006, Schmidt et al., 2002]. Classically, samples are irradiated and removed from the flux. Then, the nuclides of interest are purified and prepared for the intended experiments. Going to more exotic nuclides, the low production rates and short half-lives make this method unfeasible, marking the need for an online method and radioactive ion beam (RIB) facilities [Fulton, 2011, Lunney et al., 2003].

The major distinction between the two major RIB preparation methods is the thickness of the target. The basic scheme of production can be seen in Figure 2.4. Facilities using a thin target in which the products of the reaction are sufficiently energetic to leave the target and traverse the setup afterward are said to use the *in-flight* method. The projectiles are heavy ions at medium to high energies, reactions in the target are fragmentation, fission, nucleon exchange and fusion. The scattered primary beam leaves the target together with a mixture of reaction products. This cocktail can then be separated, for example by means of electromagnetic rigidity and energy loss, and afterward delivered to experimental facilities while still at comparatively high kinetic energies [Lunney et al., 2003].

Conversely, exposing a thick target to various projectiles, the reaction products from spallation, fission and neutron capture are stopped in the target and thermalized. By heating the target, the products diffuse out of the target, are ionized in a selected ion source and transported to experimental facilities. Again, the cocktail of products must be separated. Due to the lower energies, different methods like magnetic mass separators are employed. This method is called *ISOL*, short for Isotope Separator OnLine.

Both methods have their respective advantages and disadvantages. In-flight is very fast, highly efficient, capable of producing highly pure beams with energies
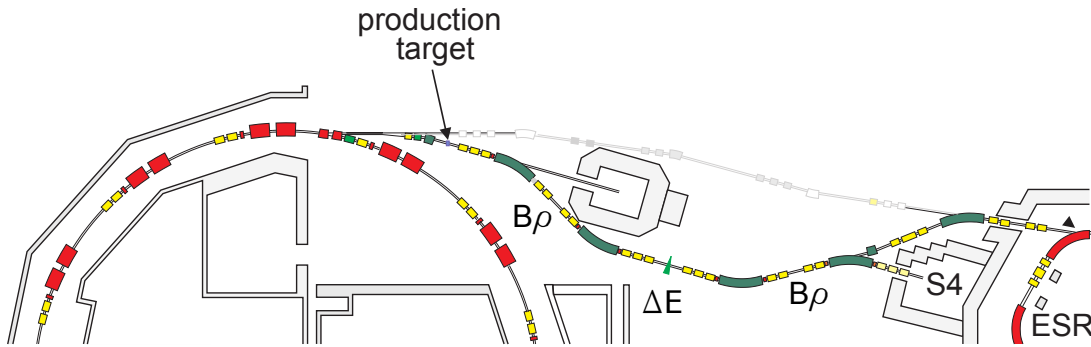
Figure 2.5.: Schematic overview of the FRS at GSI showing a section of the SIS, the production target and the separation by magnetic rigidity $(B\rho)$, energy loss (ΔE) and $B\rho$ as well as the connected experimental areas S4 and ESR [FRS Group at GSI, 2016].

near that of the primary beam. At the same time, increased emittances due to the reactions can make subsequent experiments difficult. Contamination from secondary products from interaction with matter after separation is possible.

ISOL, on the other hand, produces smaller emittance beams since the particles have been thermalized. This also allows fine control over the beam energy. Due to the time it takes the products to diffuse out of the target, access to very short-lived nuclides is problematic in ISOL facilities. Additionally, both diffusion transport time and effusion efficiency are dependent on the chemistry of the produced nuclides, taking parts of the elements out of reach for ISOL [Blaum, 2006].

An option to reach the desired low emittance beam characteristics that are inherent for the ISOL-approach at in-flight is to catch the produced ions in matter and extract them from the stopping material. A noble gas, typically helium, is mostly used since it mitigates the problems of slow diffusion and strong chemical dependency of the extraction time posed by solid state stoppers. The ions are dragged through the gas by means of electric fields, extracted from the stopping gas cell through a nozzle and transported to subsequent systems [Wada, 2013, Wada et al., 2003, Savard et al., 2003].

2.2.1. FRS at GSI as an Example of an In-Flight Facility

At GSI, an relativistic ion beam is generated by a sequence of a selected ion source, the linear accelerator UNILAC and the synchrotron SIS18. Available elements range from protons to uranium at selectable energies between $50\,\mathrm{MeV/u}$ and above $1,000\,\mathrm{MeV/u}$. The maximum number of particles per cycle depends on the element, for U^{73+} close to 10^{10} particles are possible. The magnet cycle without extraction takes about three seconds, the extraction speed can be chosen depending on the need of the connected experiment. By providing UNILAC-

beam to experiments during the SIS acceleration cycle and switching between experiments on a cycle-to-cycle base, multiple experiments can be provided with beams of different elements and energies.

In Figure 2.5 a diagram of the FRS at GSI can be seen, an example of an in-flight facility. The SIS18 beam is transported to a production target. The mixture of primary beam and products enters the fragment separator *FRS*. Here, the most common method of separation is a combination of magnetic rigidity dispersion, energy loss in a shaped degrader and again magnetic rigidity dispersion. This allows to select single nuclides from the product cocktail, to identify and transport them to several different locations for subsequent experiments [Geissel et al., 1992]. The FRS will be further explained in section 6.1.

The Facility for Antiproton and Ion Research (FAIR) will continue along this path with higher intensities and energies from the upgraded UNILAC and SIS 18, the new synchrotron SIS100 and the Super-FRS. The Super-FRS is a combination of two $B\rho$-ΔE-$B\rho$-separator stages (pre-separator and main-separator) and three branches connecting the storage rings, a high energy experimental area and, including an energy buncher, the low energy experimental area [Geissel et al., 2003].

2.2.2. ISAC at TRIUMF as an Example of an ISOL Facility

At TRIUMF, ISAC, the Isotope Separator and ACcelerator [Bricault et al., 1997, Dilling et al., 2014b], is using the ISOL method to produce the desired nuclides. The main accelerator of TRIUMF is an isochronous H$^-$ cyclotron, delivering proton beams of up to $500\,\mathrm{MeV}$ and $100\,\mu\mathrm{A}$ to ISAC. ISAC's structure is shown in Figure 2.6. The beam impinges on a thick target made from stacks of the selected materials, mostly in the form of oxides and carbides, producing the nuclides by means of spallation and fission. The target is heated by the deposited proton energy with additional electric heating, diffusing the products to the surface and effusing out of the target material.

A selection of ion sources [Bricault et al., 2014] can be coupled to the target, commonly available are hot surface ionization, Forced Electron Bombardment Arc Discharge (FEBIAD) and the TRIUMF Resonant Ionization Laser Ion Source (TRILIS). While surface ionization and discharge source have different ionization probabilities depending on ionization potentials, they ionize wide ranges of the produced elements. Resonant laser ionization conversely is element-specific due to the need for tuned laser frequencies fitting the atomic transitions.

With the source held at a potential of some $10\,\mathrm{kV}$, the ions are accelerated to a kinetic energy suitable for electrostatic transport to experiments and accelerators. In order to select the nuclei of interest from the mixture, a magnetic mass separator is included. The RIB is then transported to a yield station, in which
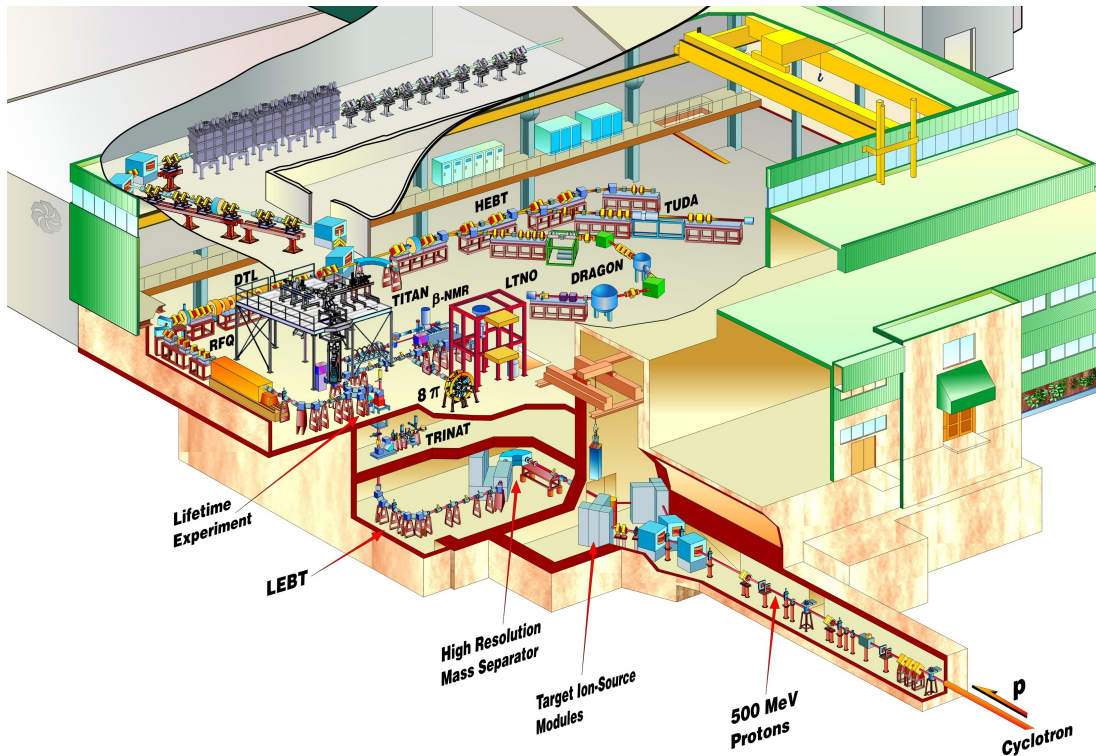
Figure 2.6.: An overview of the ISAC facility at TRIUMF. A proton beam of 500 MeV and up to 100 μA impinges on a thick target, forming exotic nuclei by means of spallation. These nuclei diffuse out of the target, are ionized and transported in electrostatic beamlines to several experiments. A magnetic mass separator with a mass resolving power of 2,000 and the choice of the ion source allow the selection of a range nuclei. In the ISAC I hall shown in the schematic, several low and mid energy experiments are located, TITAN being one of them. A second stage of acceleration delivers higher energy RIB to ISAC II shown in the upper part of the picture [TRIUMF, 2016].

the particles in the beam are identified and quantified by means of decay spectroscopy. Finally, the beam is either directly delivered to a set of experiments at low kinetic energies or further accelerated for experiments requiring higher energies.

TRIUMF's Advanced Rare IsotopE Laboratory (ARIEL) is a planned extension to the existing ISAC facility, adding a 50 MeV, 10 mA continous beam electron linear accelerator as a photo-fission driver for an ISOL target, a second proton ISOL target, their corresponding mass separators and transfer beam lines to ISAC. This extension will allow access to more neutron rich nuclides as well as allowing parallel operation with up to three targets [Dilling et al., 2014a].
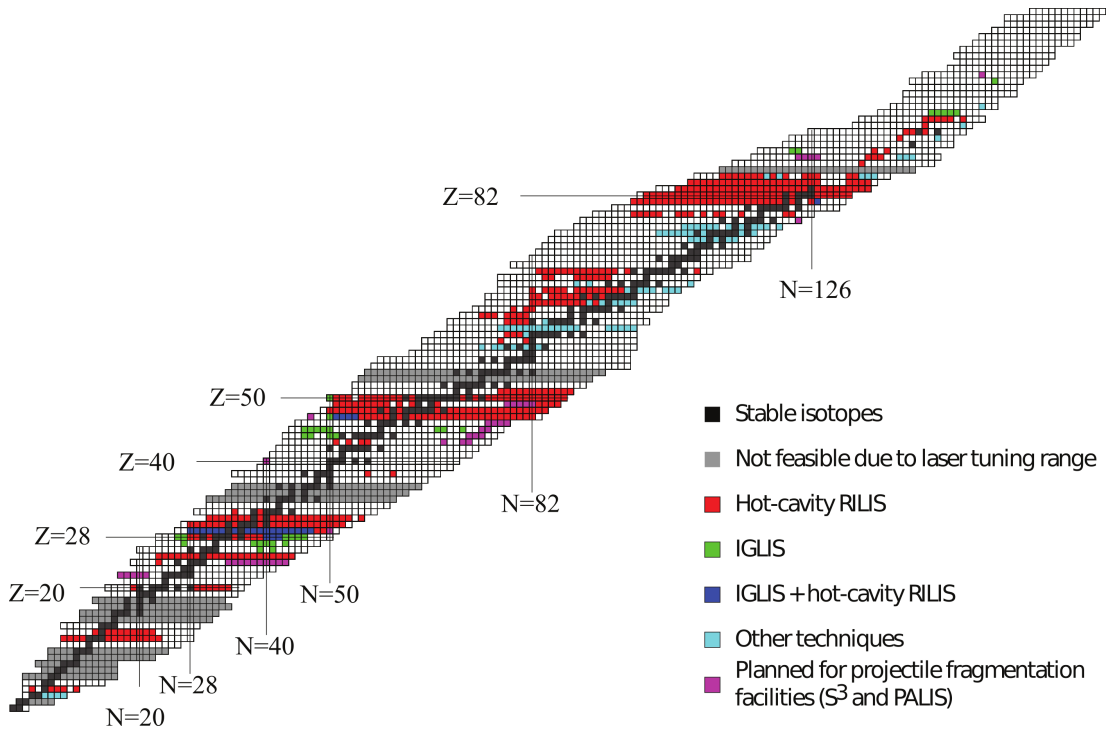
Figure 2.7.: Chart of nuclides showing RIB produced by resonant ionization worldwide [Marsh, 2014].

2.2.3. Isobaric Contamination of Radioactive Ion Beams

As discussed before, the production mechanisms for RIB always generate a mixture of different nuclides. Several options are available to select the desired nuclides from this mixture.

For in-flight systems, selection by momentum and energy loss allow very narrow separation. Unfortunately, every window or degrader in the beam path produces secondary products in the already cleaned beam, causing impurities and requiring multiple stages of cleaning [Rodríguez et al., 2010]. At lower kinetic energies, below a few hundred MeV/u, the products are not fully ionized making isobarically clean separation impossible.

In the case of ISOL facilities, magnetic separators at kinetic energies of some ten keV are commonly used [Kugler et al., 1992, Bricault et al., 1997]. Their resolving power of a few thousand is able to resolve isobars at lower masses but not sufficient for higher masses. Here, only separation of particles with larger mass differences is possible.

Due to the stopped and neutral particles using a selective ionization technique is possible. A common method is resonant laser ionization. Here, several lasers are tuned to a sequence of transitions specific to the element of interest, exciting those atoms into either auto-ionizing or very lightly bound Rydberg states. In this way, only atoms of one element are ionized and separation of the mixture of
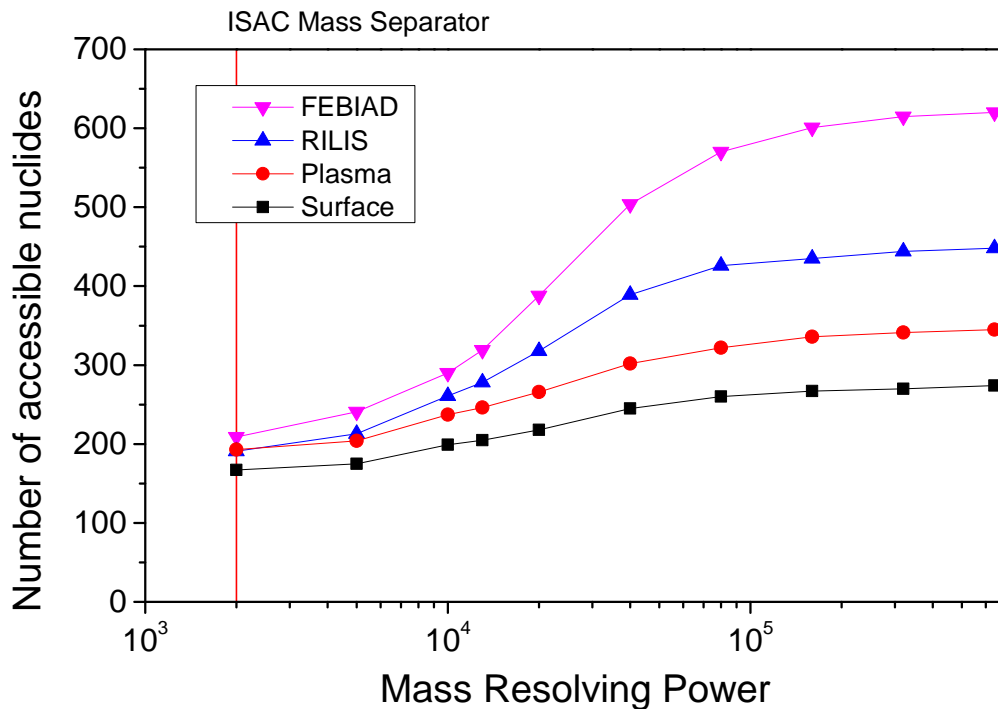
Figure 2.8.: Accessible nuclides for an ISOL facility depending on ion source and separator mass resolving power. The data is taken from the ISOLDE yield database. A nuclide is defined as accessible if the nuclide of interest makes up more than $50\,\%$ of the transported ions after the separator. Gaussian peak shapes are assumed. Marked is the mass resolving power of the ISAC mass separator [Greiner, 2015].

isotopes afterward is rather simple since mass resolving powers of a few hundred are already sufficient [Marsh, 2014].

Unfortunately, laser ionization requires element-specific ionization schemes. For some elements, no scheme is available (Figure 2.7). Also, getting high separation and high efficiency at the same time is impossible. In order to achieve a strong interaction between laser beams and atoms, the interaction region is designed as a tube and heated like the target in order to prevent adsorption. In this case, the hot surface contributes to ionization, reducing the suppression of unwanted species. It is possible to repel the surface generated ions with a suitable electrode and ionize only the neutral particles after passing the electrode. This significantly reduces the efficiency though [Marsh, 2014].

Therefore, an element-independent method to produce isobarically clean beams at low energies is needed. The solution are fast, high-resolving mass spectrometers.

In order to estimate a required resolving power, production yields from the ISOLDE facility at CERN for the four main ion sources have been taken. A

nuclide is defined as accessible if it makes up more than $50\,\%$ of the transported ion current after the separator. Further more, Gaussian transmission peak shapes are assumed.

Figure 2.8 shows the accessible nuclides in relation to the separator mass resolving power for various ion sources. It can be seen that with a separation power of $50,000$, the number of accessible nuclides increases strongly.

2.3. Mass Spectrometry in Nuclear Physics

Mass spectrometry can play two significant roles in nuclear physics. Either as the experiment itself, yielding mass values that are of interest as described before, or as means of purification of the nuclides of interest for subsequent experiments. A short overview over relevant techniques follows.

2.3.1. Deflection in Magnetic Fields

Already the first mass spectrometers used by Thomson and Aston [Aston, 1920] employed the deflection of ions in a magnetic field. The radius ρ of ions traveling in a homogenous magnetic field is

$$\rho = \frac{m}{Q}\frac{v}{B} \qquad \frac{m}{Q} = \frac{B\rho}{v} \tag{2.3}$$

For ions with identical speed v, the deflection is therefore proportional to their mass-to-charge ratio. Ions of differing speeds can be focused by employing a combination of electrostatic and magnetic fields. Further, several geometries have been found that allow double-focusing, achieving a focus both for differing speeds as well as directions [Audi, 2006].

Resolving powers of several 10,000 are achievable with instruments of this kind as well as large dynamic ranges. Disadvantage is the need for very narrow slits in order to achieve highest resolving powers, limiting the efficiency of the instrument.

2.3.2. Mass Determination in Nuclear Reactions

If all kinetic and internal energies of particles in nuclear reactions and all but one masses are known, the unknown mass can be determined via the Q value

$$Q = \left(\sum_i m_i^{\mathrm{i}} - \sum_j m_j^{\mathrm{f}} \right) c^2 = \sum_i K_i^{\mathrm{i}} - \sum_j K_j^{\mathrm{f}} \tag{2.4}$$

with m_i^{i} and K_i^{i} the masses and kinetic energies of the initial state and m_i^{f} and K_i^{f} the parameters of the final state, respectively.

While this method is suitable for all nuclear reactions, especially the α-decay allows precise measurements. This is due to just one and two particles involved in the initial and final states, respectively, resulting in a line-type spectrum. Also, identification is possible by correlated measurement of a chain of α-decays [Hofmann and Münzenberg, 2000].

The possibility of unrecognized excited states involved in the decay adds some uncertainty to masses deduced by α-spectroscopy.

2.3.3. Storage Ring Mass Spectrometry

Storage ring mass spectrometry measures the revolution frequency of relativistic ions confined in a storage ring [Bosch, 2003]. In first order approximation, the revolution frequency behaves as

$$\frac{\Delta f}{f} = -\frac{1}{\gamma_t^2} \frac{\Delta(m/Q)}{m/Q} + \frac{\Delta v}{v} \left(1 - \frac{\gamma^2}{\gamma_t^2} \right) \tag{2.5}$$

With the first term containing the mass information, the second term contributes only to peak broadening and has to be minimized. Shown in Figure 2.9, the two obvious choices are either to reduce the velocity spread of the ions $\Delta v/v \to 0$ (Schottky Mass Spectrometry, SMS) or operate the ring at its transition point γ_t and inject ions with relativistic $\gamma \approx \gamma_t$, achieving isochronicity for a range of velocities and one m/q (Isochronous Mass Spectrometry, IMS).

In the first case, electron cooling, sometimes in combination with fast stochastic pre-cooling, is used to reduce the velocity spread of the ions stored in the ring. Pickups in the ring measure the Schottky noise of passing ions over the course of several turns. This signal is then Fourier-transformed, leading to a frequency spectrum where each peak corresponds to the m/q of a species trapped in the ring.

For IMS, cooling is not required as the ring is in an isochronous mode. In a TOF detector, the ions pass a carbon foil ejecting electrons from the foil, which are then accelerated and guided with electric and magnetic fields onto MCP detectors. By measuring the timestamp of each ion's passing through the foil, revolution frequencies are determined and therefore the mass.
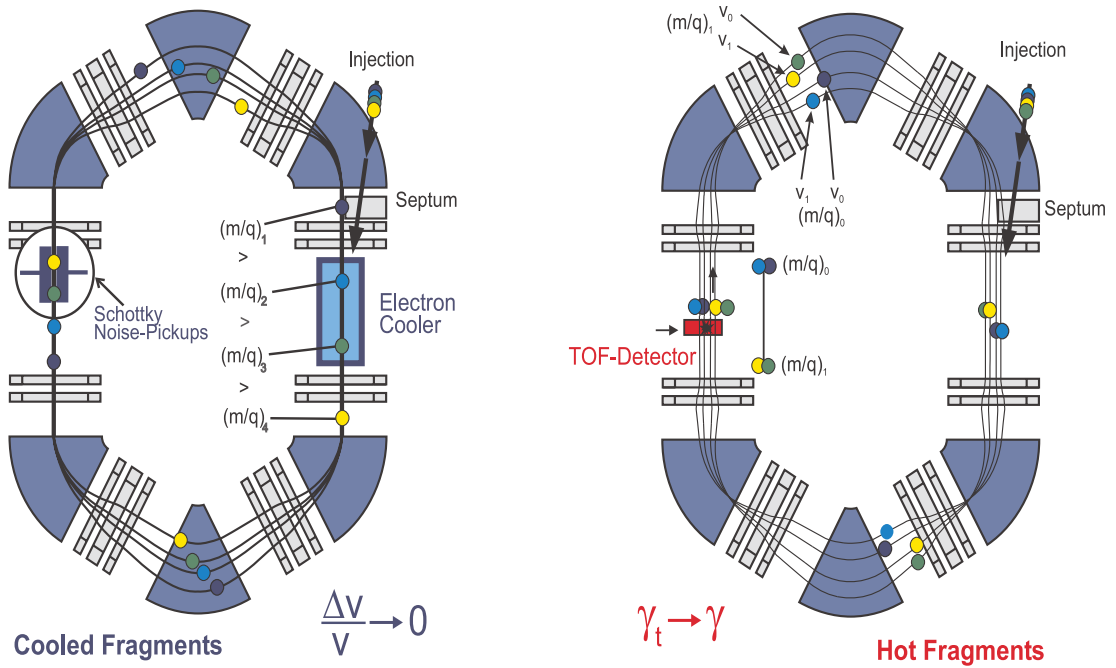
Figure 2.9.: Schematic view of the experimental storage ring ESR at GSI showing two methods of mass spectrometry relying on revolution frequencies applied there. On the left, Schottky mass spectrometry (SMS), employs an electron cooler to reduce the velocity differences between the ions to achieve a precise relationship between flight time and m/q. A disadvantage is the time required for the cooling (a few seconds), making the method unsuitable for very short-lived nuclides. On the right, the ring is tuned so that the revolution frequency becomes independent of the velocity over a certain range and the TOF detector detects ions passing. This method is capable of measuring nuclides with half-lives down to below the millisecond range [Bosch, 2003].

Resolving powers are in the region of $5 \cdot 10^5$ for SMS and $1 \cdot 10^5$ for IMS. An advantage of Schottky MS is the wide mass range and the ability to continuously measure the masses and life-times of ions and (if they fall into the acceptance of the ring) their decay products over several minutes. Conversely, IMS is capable of measuring ions with lifetimes in the order of $10\,\mu$s.

While it is possible to separate ions depending on their mass in SMS mode by inserting scrapers in the ring, separation by magnetic rigidity and energy loss is a better suited method. IMS is not capable of separating ions.

2.3.4. Penning Trap Mass Spectrometry

The most commonly used method for high accuracy mass spectrometry is Penning trap mass spectrometry [Bollen et al., 1996]. In a homogenous magnetic field, the ions move on a circular path in the orthogonal plane to the magnetic field

with a cyclotron frequency of

$$\omega_c = \frac{Q}{m} B \qquad (2.6)$$

Penning trap mass spectrometry measures this frequency. Unfortunately, any velocity component in longitudinal direction results in the ion leaving the trap. Therefore, a Penning trap uses an additional static electric quadrupole field to confine the ion in this direction as well. In this combination of fields, the ion now shows three modes of oscillation with the frequencies ω_z (longitudinal oscillation), ω_+ (modified cyclotron motion) and ω_- (magnetron motion).

By measuring these frequencies, mass determination is possible. In analytical chemistry, Fourier transform ion cyclotron resonance (FT-ICR) is the method of choice [Marshall et al., 1998]. Image currents induced into the segmented electrodes forming the electric field of the trap are measured and, by performing a Fourier transformation, the frequency components are derived. Unfortunately, the image currents are too small for current technology if just one ion is present in the trap. Loading larger amounts of ions into the trap reduces the precision by space charge effects.

A method to circumvent this is the time-of-flight ion cyclotron resonance method (TOF-ICR). Here, the motion of the ion in the trap is excited by applying an additional RF potential with the frequency ω_{RF} on a segmented middle electrode, generating an additional quadrupole field. This excitation, if tuned to the sum frequency $\omega_c = \omega_+ + \omega_-$, is capable of converting magnetron motion into modified cyclotron motion and vice versa. After exciting the ion in the trap for a set time, the ions are ejected from the trap onto a detector outside of the strong magnetic field of the trap. The energy stored in the cyclotron motion is converted in the magnetic gradient into additional velocity, shortening the time of flight from the trap onto the detector. By scanning ω_{RF}, the minimum for the TOF can be found at $\omega_{RF} = \omega_c$ and, with Equation 2.6, the mass of the stored ions [Bollen et al., 1996].

$$\frac{\delta m}{m} \propto \frac{Q \cdot B}{m} \cdot T_{RF} \cdot \sqrt{N} \qquad (2.7)$$

Main limitations to this method are the need to scan the excitation frequency, requiring 100 to 1000 ions for a mass measurement. Excitation times of fractions of a second are needed to achieve sufficient resolving powers. Also, the needed excitation time scales with the mass, aggravating this limitation for heavier nuclides. This limits the nuclides that can be measured with this method to those with longer half-lives and higher production rates [Bollen, 2001]. Choosing highly charged ions for measurement, the mass precision can be increased at the cost of ionization efficiencies and time required for this process.

Penning traps can also be used to spatially separate ions with high resolving powers. This is performed by mass-selective cooling [Bollen et al., 1996]. This method is limited by cooling times of $\approx 100\,\text{ms}$ and ion capacities of $\approx 1,000$ ions per cycle.

2.3.5. Time-of-Flight Mass Spectrometry

Ions accelerated to a certain kinetic energy will travel with a velocity that is dependent on their mass-to-charge ratio. Therefore, measuring the time the ion requires to traverse a distance allows to measure the ions' mass-to-charge ratio. With multiple-reflection time-of-flight mass spectrometry (MR-TOF-MS), resolving powers of $\approx 10^5 - 10^6$ within about $10\,\text{ms}$ are possible. A more in depth treatment will be given in section 2.4.

Limitations are collisional losses with residual gas, the need for long flight paths and high voltage stability requirements to achieve high resolving powers.

2.3.6. Comparison of Different Methods

Method	Time	Res. Power	Mass Range	Req. Ions	Sep.
SMS	a few seconds	$\approx 5 \cdot 10^5$	Large	Single ions	$\approx$
IMS	$\approx 10 - 100\,\mu\text{s}$	$\approx 1 \cdot 10^5$	Moderate	Single ions	No
TOF-ICR	$\approx 0.1 - 10\,\text{s}$	$\approx 10^6 - 10^7$	Very narrow	$\approx 100 - 1000$	Yes
MR-TOF	$\approx 10\,\text{ms}$	$\approx 10^5 - 10^6$	Moderate	≈ 10	Yes

Table 2.2.: Possible mass spectrometry methods for exotic nuclides.

Table 2.2 shows a comparison of the discussed four modern methods for RIB mass spectrometry. Indicated are typical measurement time, resolving power, mass range, required ion counts for a measurement and availability as a separation method.

For separation of isobars, only Penning traps and MR-TOF-MS are available. MR-TOF-MS is desirable for both mass spectrometry and, in combination with an ion gate or similar device, for isobar separation of short lived heavier nuclides [Plaß et al., 2008].

2.4. Time-of-Flight Mass Spectrometry

Time-of-flight mass spectrometry is a method of electrostatically manipulating ions in a way that their different mass-to-charge ratios result in a temporal distribution which can be used to measure those masses or separate the ions spatially.

2.4.1. Electrostatic Ion Optics

In order to describe the properties of ion optical devices and to aid in their design and optimization, several methods are available. Two were mainly used in this work, the matrix method with its description of ion optic aberrations and particle tracing.
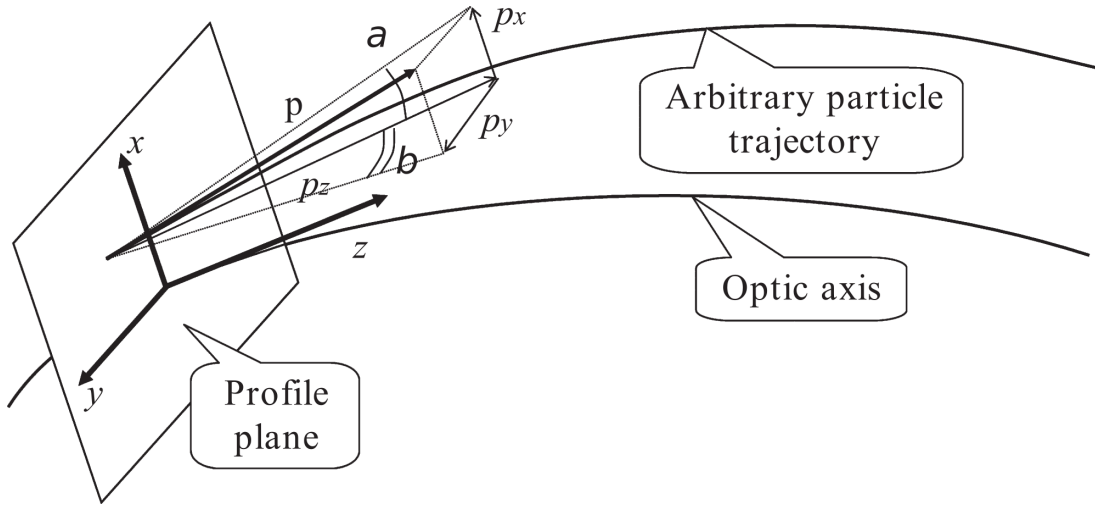
Matrix Method

Figure 2.10.: Definition of trajectory differences to the reference optical axis [Yavor, 2009].

Using an arbitrarily defined reference path, also called optical axis, of a particle with path length z along the reference path, kinetic energy $K^{\mathrm{ref}}(z)$, mass m^{ref} and charge Q^{ref}, paths of further particles can be described [Yavor, 2009, Wollnik, 1987] by, as shown in Figure 2.10, assuming a plane perpendicular to the reference path at position z with the parameters

$x(z), y(z)$	Distances to reference path
$a(z) = dx/dz$	Angle to reference path in $x - z$ plane
$b(z) = dy/dz$	Angle to reference path in $y - z$ plane
$T(z) = t - t^{\mathrm{ref}}$	Deviation of flight time
$\delta(z) = \frac{K/Q}{K^{\mathrm{ref}}/Q^{\mathrm{ref}}} - 1$	Relative deviation of kinetic energy to charge ratio
$\gamma = \frac{m/Q}{m^{\mathrm{ref}}/Q^{\mathrm{ref}}} - 1$	Relative deviation of mass to charge ratio

For static optics, at an arbitrary position z the vector of the parameters $\vec{\chi}(z) = (x, a, y, b, T, \delta, \gamma)$ is a function of the particle parameters at some initial position z_0, namely $\vec{\chi}(z) = f(\vec{\chi}(z_0), z)$. Assuming that the parameters of $\vec{\chi}(z_0)$ are small, a power series, called the aberration expansions, for the parameters is justified. For the example x the expansion reads

$$x(z) = (x|x)x_0 + (x|a)a_0 + (x|y)y_0 + (x|b)b_0 + (x|T)T_0 + (x|\delta)\delta_0$$
$$+(x|\gamma)\gamma_0 + (x|xx)x_0^2 + (x|xa)x_0a_0 + (x|xy)x_0y_0 + (x|xb)x_0b_0 \qquad (2.8)$$
$$+(x|xT)x_0T_0 + (x|x\delta)x_0\delta_0 + (x|x\gamma)x_0\gamma_0 + (x|aa)a_0^2 + ...$$

with $(...|...)$ the expansion coefficients, for example $(x|xa)$ describing the dependency of x on $x \cdot a$.

The first order coefficients typically describe the intended behavior of the instrument and are called paraxial coefficients. The higher orders are called aberration coefficients and describe the deviations from the intended behavior. Considering only the paraxial coefficients, e.g. setting all other coefficients to zero, is the paraxial approximation.

Several of the coefficients are known due to inherent properties. In time-independent fields, all dependencies on T_0 vanish, so all coefficients containing T are 0 beside $(T|T)$. In purely electrostatic systems, the path of the ions does not depend on the mass-to-charge ratio, only its time-of-flight does. So, all position coefficients containing γ are zero aside from $(T|...)$. Again for time-independent fields and if both initial and final plane are in field free regions, the energy is only dependent on itself, $(\delta|...) = 0$ for all coefficients beside $(\delta|\delta)$. By designing systems with certain symmetries, additional components can be removed, too.

In the paraxial approximation, the changing ion parameters between two profile planes 0 and 1 can be described with a transfer matrix of the form

$$\mathbf{T}_{01} = \begin{pmatrix} (x|x) & (x|a) & (x|y) & (x|b) & (x|T) & (x|\delta) & (x|\gamma) \\ (a|x) & (a|a) & (a|y) & (a|b) & (a|T) & (a|\delta) & (a|\gamma) \\ (y|x) & (y|a) & (y|y) & (y|b) & (y|T) & (y|\delta) & (y|\gamma) \\ (b|x) & (b|a) & (b|y) & (b|b) & (b|T) & (b|\delta) & (b|\gamma) \\ (T|x) & (T|a) & (T|y) & (T|b) & (T|T) & (T|\delta) & (T|\gamma) \\ (\delta|x) & (\delta|a) & (\delta|y) & (\delta|b) & (\delta|T) & (\delta|\delta) & (\delta|\gamma) \\ (\gamma|x) & (\gamma|a) & (\gamma|y) & (\gamma|b) & (\gamma|T) & (\gamma|\delta) & (\gamma|\gamma) \end{pmatrix} \qquad (2.9)$$

Transport of ions between those planes becomes

$$\vec{\chi}_1 = \mathbf{T}_{01}\vec{\chi}_0 \qquad (2.10)$$

Consequently, the transport through a sequence of planes becomes product of several matrices

$$\vec{\chi}_n = \mathbf{T}_{(n-1)n}...\mathbf{T}_{23}\mathbf{T}_{12}\mathbf{T}_{01}\vec{\chi}_0 \qquad (2.11)$$

For higher orders the same formalism can be used, both vectors and matrices have to be modified to contain the higher orders as well.

Particle Tracing

Another method to derive the behaviour of an instrument is particle (ray-) tracing. For this method, a given set of electrodes and their potentials is taken as Dirichlet boundary condition to solve the Laplace equation

$$\Delta\phi\left(\vec{r}\right) = \nabla\vec{E}\left(\vec{r}\right) = 0 \tag{2.12}$$

with the electric potential $\phi\left(\vec{r}\right)$ and the electric field $\vec{E}\left(\vec{r}\right)$ on a grid, yielding large potential arrays. This is called the finite difference method. Solving the Laplace equation is typically done in an iterative approach. Due to the needed large number of calculations, both due to high precision required to get a good approximation to reality and the typically large number of grid points, these calculations are quite time consuming.

While it would be possible to redo these calculations for every combination of potentials that might be needed for optimization or due to time dependent potentials, a different approach is usually employed. The potential arrays are computed once for every set of connected electrodes while every other electrode is kept at ground potential. The electrode of interest is usually set to 1 Volt in order to gain the ability to calculate the potential array for arbitrary applied voltages by $\phi_n\left(\vec{r}, U_n\right) = U_n\phi_n^{1V}\left(\vec{r}\right)$. Due to the property that the solutions of the Laplace equation are additive, the potential for each grid point and for n electrodes can be calculated as

$$\phi_n\left(\vec{r}\right) = \sum_n U_n\phi_n^{1V}\left(\vec{r}\right) \tag{2.13}$$

By interpolation, potentials surrounding arbitrary positions in space can be calculated, from which the gradient and therefore the electric field is derived. The trajectories of particles with chosen start conditions can then be computed using numerical methods, usually 4th order Runge-Kutta. By choosing a random population, this approach becomes a Monte Carlo method of estimating the transfer properties that can be again expressed in the aberration coefficients as introduced before.

This method allows the introduction of non-stationary fields like they are used in RFQs or for ion gates as well as statistic processes like ion-gas interactions or ion-ion interactions making it highly suitable for simulation of time of flight mass spectrometry.
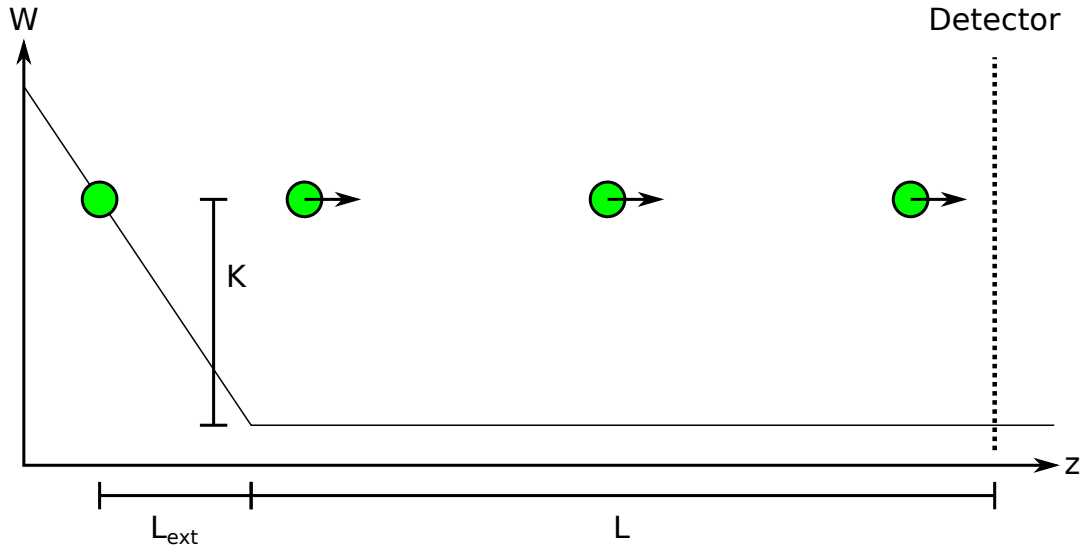
Figure 2.11.: Linear TOF-MS with acceleration from rest.

2.4.2. Basics of Time-of-Flight Mass Spectrometry

In its most basic approach, time-of-flight mass spectrometry uses the fact, that the kinetic energy of ions that started at a certain potential and were accelerated due to a potential difference is independent of the mass of the particle. Due to

$$K = Q\Delta U = \frac{1}{2}mv^2 \qquad v = \sqrt{\frac{Q}{m}2\Delta U} \tag{2.14}$$

the time to traverse a path with the length of L is

$$t_{\mathrm{drift}} = \frac{L}{v} = \sqrt{\frac{m}{Q}\frac{L^2}{2\Delta U}} \propto \sqrt{\frac{m}{Q}} \tag{2.15}$$

As can be seen, particles with a lower mass-to-charge ratio reach the end of the path earlier than those with higher m/Q. Usually, a particle detector like a MCP or channeltron is situated at the end of the ion path [Yavor, 2009]. Since there is no non-destructive, highly efficient method to derive a timestamp for ions passing a plane at low energies, start signals are given from chopping a continuous beam, pulsed ionization of the particles of interest or pulsed extraction of previously stored ions. In the case of an instrument for rare ion beams, the options to chop a continous beam is not desirable due to the loss of efficiency that is connected with this. The particles are also already ionized so pulsed ionization is also no option.

In a linear TOF mass spectrometer with pulsed extraction, the moment, in which

an extraction field as shown in Figure 2.11 is applied, is taken as the start signal for measurement of the time-of-flight. Assuming a linear field E over the acceleration length L_{ext}

$$QE = ma \qquad t_{\text{ext}} = \sqrt{\frac{m}{Q}\frac{2L_{\text{ext}}}{E}} = \frac{\sqrt{2m}}{QE}\sqrt{K} \qquad (2.16)$$

with the kinetic energy $K = QEL_{\text{ext}}$ and for the full time of flight for the particle from extraction until detection in the

$$t_{\text{TOF}} = t_{\text{ext}} + t_{\text{drift}} = \frac{\sqrt{2m}}{QE}\sqrt{K} + L\sqrt{\frac{m}{2}}\frac{1}{\sqrt{K}} \qquad (2.17)$$

So for particles at rest, at a singular position, in a perfectly linear acceleration field and no aberrations in the drift region, a perfect mass spectrum can be expected.

Time Focus

The spatial distribution of ions in the acceleration region has not been taken into account yet. Since the kinetic energy of the ions is directly proportional to the path length, in which they experience acceleration, the deviation of the start position Δz_0 contributes directly to the final kinetic energy

$$K = QEL_{\text{ext}} = QE\left(L_{\text{ext}}^{\text{ref}} - \Delta z_0\right) = \left(1 - \frac{\Delta z_0}{L_{\text{ext}}^{\text{ref}}}\right)K^{\text{ref}} = (1+\delta)\,K^{\text{ref}} \qquad (2.18)$$

With Equation 2.17, the time-of-flight then becomes

$$\begin{aligned}
t_{\text{TOF}} &= \frac{\sqrt{2m}}{QE}\sqrt{K^{\text{ref}}(1+\delta)} + L\sqrt{\frac{m}{2}}\frac{1}{\sqrt{K^{\text{ref}}(1+\delta)}} \\
&= \sqrt{\frac{2m}{K^{\text{ref}}}}\left(L_{\text{ext}}^{\text{ref}}\sqrt{(1+\delta)} + \frac{L}{2}\frac{1}{\sqrt{(1+\delta)}}\right)
\end{aligned} \qquad (2.19)$$

Doing a Taylor expansion, one can see that the first order coefficient $(T|\delta)$ vanishes for $L = 2L_{\text{ext}}^{\text{ref}}$. This is the position called the primary time focus, illustrated in Figure 2.12. In this position, ions that started a bit farther from the detector but gained a bit more velocity, reached the reference ions. This setting is yielding
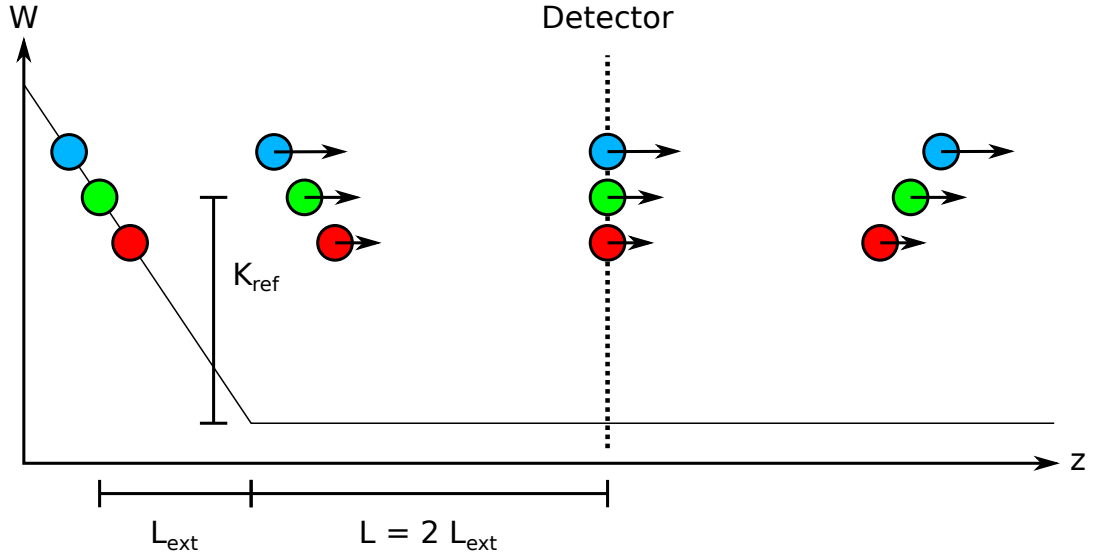
Figure 2.12.: Spatial distribution of ions in the acceleration region causes a difference in path length to the detector as well as different energies. In first order, the effects cancel each other out for $L = 2L_{\text{ext}}^{\text{ref}}$.

the highest resolving power achievable for a configuration with a single linear acceleration gradient [Yavor, 2009].

In first order approximation, the flight time to the primary time focus becomes

$$t_{\text{TOF}} = 2L_{\text{ext}}^{\text{ref}}\sqrt{\frac{2m}{K^{\text{ref}}}} \tag{2.20}$$

The second order coefficient obtained as well from Equation 2.19 reads

$$(T|\delta\delta) = \frac{L_{\text{ext}}^{\text{ref}}}{2}\sqrt{\frac{m}{2K^{\text{ref}}}} \tag{2.21}$$

By using a two-stage acceleration scheme as shown in Figure 2.13, an additional degree of freedom is gained. The location of the primary time focus here is

$$L = 2L_{\text{ext}}\left(\frac{K^{\text{ref}}}{K_{\text{ext}}}\right)^{3/2} - 2L_{\text{acc}}\sqrt{\frac{K^{\text{ref}}}{K_{\text{ext}}}}\frac{1}{1 + \sqrt{K_{\text{ext}}/K_{\text{ref}}}} \tag{2.22}$$

This allows to shift the primary time focus at a given geometry by selecting the ratio of $K_{\text{ext}}/K_{\text{ref}}$ or to eliminate the second order TOF aberration $(T|\delta\delta)$ [Wiley and McLaren, 1955].
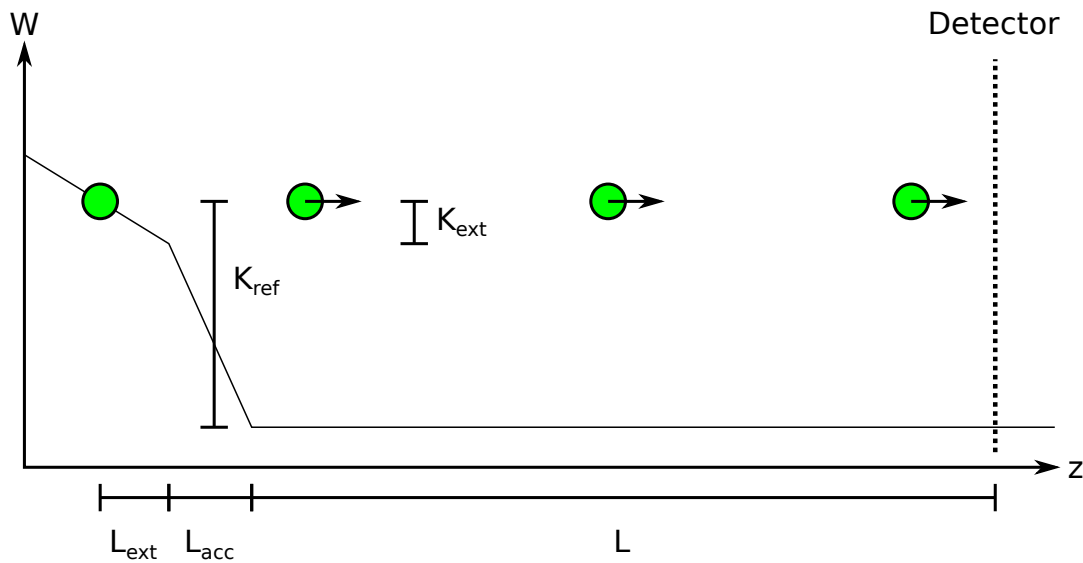
Figure 2.13.: Using a two-staged scheme with an extraction region and a separate acceleration region allows to eliminate the second order coefficient $(T|\delta\delta)$.
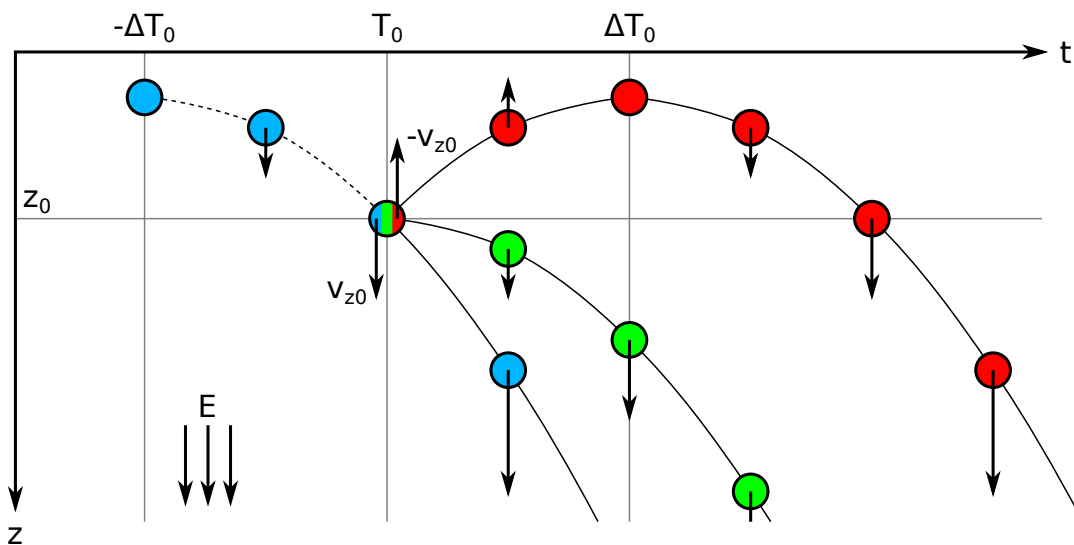
Figure 2.14.: Ions starting with differing velocities in z direction will behave as if started at slightly different positions at different times.

Turn-Around Time

Due to thermal movement, the ions possess a distribution of velocities. Velocities orthogonal to the optical axis result in the requirement for focusing and therefore aberrations. Velocities in z direction however directly enter into the time-of-flight. An elegant treatment to describe this effect is to project the velocities into a combination of deviation in start position and start time as shown in Figure 2.14.

Assuming a particle that is, at T_0, in the reference position and moving in opposite direction to the extraction with $-v_{z0}$. It will decelerate in the electric extraction field until it is at rest and afterward accelerate. Compared to the reference particle which started at rest, it will lag behind by the turn-around time

$$\Delta T_0 = -\frac{m}{QE} v_{z0} \tag{2.23}$$

and virtually start at a slightly larger distance of

$$\Delta z_0 = -\frac{m}{2QE} v_{z0}^2 \tag{2.24}$$

A particle already moving in the direction of extraction behaves as if it had a head start by ΔT_0 and also a slightly longer distance Δz_0.

While the starting velocity distribution is therefore transformed into both a spatial as well as a temporal deviation to the reference particle, the spatial distribution is typically not significant for an energy-isochronous system while the turn around time presents a lower limit for peak widths and therefore resolving power [Yavor, 2009].

Assuming a thermalized population of ions of the temperature T, the velocities are distributed around zero in form of a Gaussian distribution with

$$\sigma_v = \sqrt{\frac{k_B T}{m}} \tag{2.25}$$

And with Equation 2.23 and FWHM $= \sqrt{8ln(2)}\sigma$ the FWHM deviation resulting from the turnaround time is

$$\Delta T_0^{\text{FWHM}} = \frac{\sqrt{8\ln(2)mk_B T}}{QE} \tag{2.26}$$

While the differing position is typically insignificant, the time it takes an ion to reverse its velocity in the accelerating field can't be compensated in the case of extraction from a trap and is the limit peak width for instruments that are otherwise without aberrations.

Mass Resolving power

Mass resolving power is defined as

$$R_m = \frac{m/Q}{\Delta(m/Q)} \tag{2.27}$$

where $\Delta(m/Q)$ is the smallest resolvable mass difference. For approximately Gaussian-shaped peaks of equal height, two peaks at a distance of their full width at half maximum (FWHM) results in a dip of the sum peak making FWHM an often quoted reference for resolving powers. For peaks strongly differing in height, lower heights for the measurement of the width can be used, for example at 10%.

The mass resolving power R_m is related to the time resolving power R_t with

$$R_m = \frac{m/Q}{\Delta(m/Q)} = \frac{1}{2}R_t = \frac{t_{\mathrm{TOF}}}{2\Delta t} \tag{2.28}$$

due to the square root behaviour of the flight time versus the mass-to-charge ratio. Contributing to the peak width Δt are the turn around time, ion optical aberrations and broadening caused by detector and data acquisition system [Yavor, 2009].

Assuming a simple system with one stage extraction in first order approximation, Equations 2.20, 2.26 and 2.28 the mass resolving power is

$$R_m = \sqrt{\frac{1}{4ln(2)}} \sqrt{\frac{K^{\mathrm{ref}}}{k_B T}} \tag{2.29}$$

Assuming $K^{\mathrm{ref}} = 25\,\mathrm{keV}$ and $k_B T = 0.025\,\mathrm{eV}$, the mass resolving power is $R_m \approx 600$. This overestimates the real resolving power due to higher order aberrations not considered here.

Generally higher extraction field strengths lead to a shorter turn-around time while at the same time increasing the energy distribution and therefore the aberrations.

2.4.3. Single-Reflection Time of Flight Mass Spectrometry

A way to achieve higher resolving powers is to extend the isochronous flight path. This can be achieved by a retarding field in which the ions reverse their direction, shown in Figure 2.15 [Mamyrin et al., 1973]. Ions of higher kinetic energy travel farther in the field, leaving it later than the slower ions. Time of flight from the primary time focus is
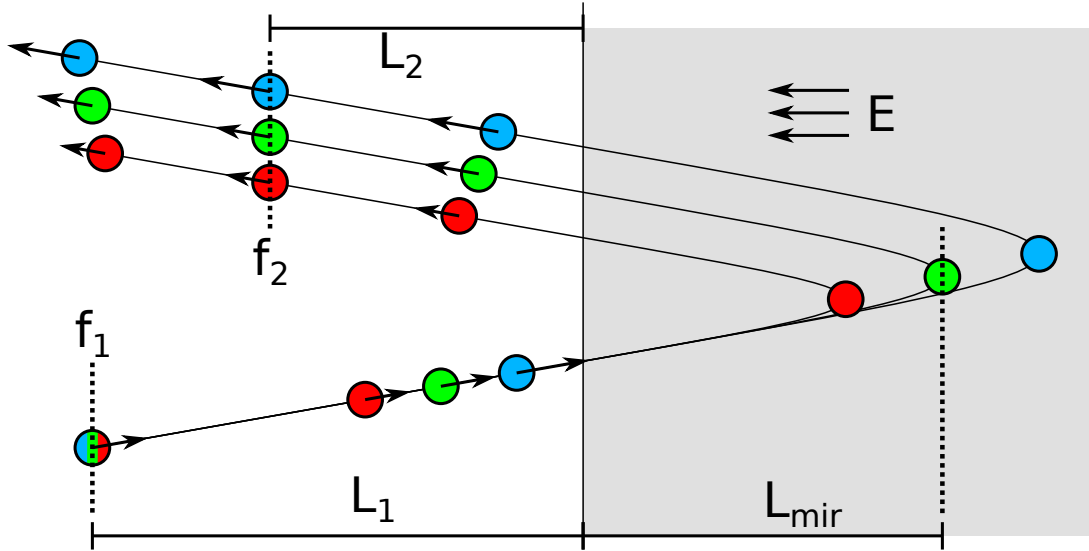
Figure 2.15.: Principle of operation for an ion mirror producing the second time focus.

$$t_{\mathrm{mir}} = \sqrt{\frac{m}{K^{\mathrm{ref}}}} \left(\frac{L_1 + L_2}{\sqrt{1 + \delta}} + 4L_{\mathrm{mir}}\sqrt{1 + \delta} \right) \tag{2.30}$$

In first order approximation, this forms a secondary time focus at

$$L_1 + L_2 = 4L_{\mathrm{mir}} \tag{2.31}$$

As shown in Figure 2.15, a reflectron mass spectrometer usually injects the ions into the mirror at an angle, allowing the placement of the detector without interfering with the incoming beam. Similar to the extraction, the second order aberration $(T|\delta\delta)$ can be eliminated by a two stage approach [Yavor, 2009]. Reflectron mass spectrometers reach resolving powers of several thousand.

Achieving linear fields as assumed here is only feasible using grids as boundaries for the different field regions. In the case of a two stage mirror, this means the ions have to pass grids four times. This reduces efficiency. It is possible to design grid-less mirrors, though the behavior becomes so complex that numerical methods are needed for optimization.

2.4.4. Multiple-Reflection Time-of-Flight Mass Spectrometry

By employing optimized ion mirrors, the aberrational contribution to peak widths can be minimized. Even though this allows to increase extraction field strengths in order to reduce the turn around time, due to technical limitations it is difficult

to achieve turn around times below one nanosecond. Assuming a peak width due to turn around time of 5 ns and no aberrational contribution, the flight time to achieve a mass resolving power of 100,000 can be calculated via Equation 2.28 as

$$t_{\text{TOF}} = 2R_m \Delta t = 1 \, \text{ms} \tag{2.32}$$

For a kinetic energy of 1 keV and ions of mass 100 u this results in a required flight path length of about 44 meters. A compact way to achieve flight paths of several 10 or 100 meters is to fold the path using a set of mirrors.

General requirements for a device of this type are [Yavor, 2009]

- Low TOF aberrations due to energy and spatial spreads

- Stable confinement along the path

- Grid-less mirrors due to high number of passes

A device of this type separates the full path of the ions into N identical cells. Assuming a peak width ΔT_0 due to turnaround time and aberrations outside of the multiple reflection analyzer. Further assuming that the additional aberration per turn, ΔT_{turn}, is independent of turn number and additional, the resolving power becomes

$$R_m = \frac{T_0 + NT_{\text{turn}}}{2\sqrt{\Delta T_0^2 + N^2 \Delta T_{\text{turn}}^2}} \tag{2.33}$$

with T_0 the flight time outside of the reflectors and T_{turn} the flighttime for one pass of a cell. As can be seen in Equation 2.33, the behaviour is asymptotic against

$$R_m\left(N \to \infty\right) = \frac{T_{\text{turn}}}{2 \cdot \Delta T_{\text{turn}}} \tag{2.34}$$

Achieving such a system is possible as shown in Figure 2.16: Either by injecting ions onto a closed path in a set of mirrors and extracting them again after a selected number of turns or by using a spatially separated path [Plaß et al., 2013].

An advantage of closed path instruments is the theoretically unlimited path length and therefore very high resolving powers achievable while keeping the device compact. In contrast, for open path systems the path length is limited by the
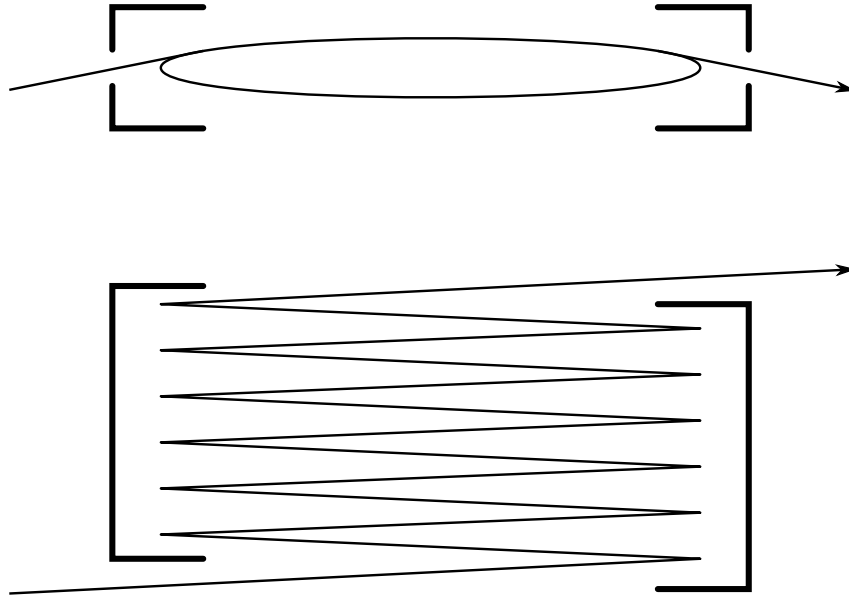
Figure 2.16.: Closed and open path multiple reflection system principles.

size and number of mirrors. Also, optimization can be tricky since the number of turns can not be reduced easily. For the closed path method, there are two main disadvantages, fluctuations introduced by injection and a mass range limit.

In order to inject ions into the analyzer, some switched potentials have to be employed. Switched potentials inevitably introduce dynamic deviations from the intended potentials on neighboring electrodes, introducing detrimental effects on the ions in the instrument.

To show the maximum unambiguous mass range, two species are assumed in the analyzer, m_1 and m_2. Their flight time is $T = L\sqrt{m/2K}$. Injected at the same time and moving at the same kinetic velocity, this results in $L_1\sqrt{m_1} = L_2\sqrt{m_2}$. In the analyzer, the flight path can be expressed as multiples of the reference path length L_{ana}. To keep the spectrum unambiguous, no ion is allowed to lag behind by more than one L_{ana} so $L_1 = N L_{\mathrm{ana}}$ and $L_2 = (N-1) L_{\mathrm{ana}}$ which results in

$$\frac{m_{\max}}{m_{\min}} = \left(\frac{N}{N-1}\right)^2 \tag{2.35}$$

In reality, the extraction from the analyzer requires pulsing of electrodes. There are two basic methods to transfer a population of ions into and out of a MR-TOF analyzer: By pulsing endcaps after passage by the ions or by pulsing the middle section of the analyzer and thereby shifting the reference potential [Plaß et al., 2013]. Disadvantage of the pulsed drift tube method is the smaller mass window that can be detected without disturbance by the pulsing.

In order to keep particles undisturbed during the changing potentials due to puls-
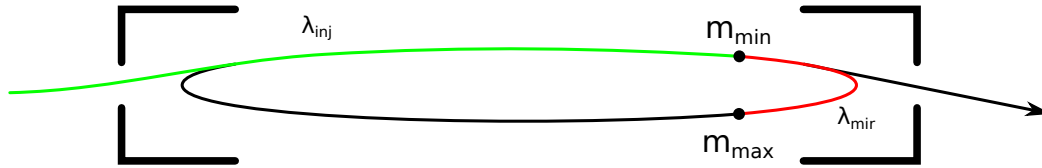
Figure 2.17.: Limit of the mass range for closed path analyzers due to pulsed electrodes.

ing, particles have to be kept in a portion of the analyzer that is safe from fields of the pulsed electrodes (Figure 2.17). Defining the ratio of flight time in which an ion is in the region of influence of the pulsed mirror $\lambda_{\mathrm{mir}} = t_{\mathrm{influenced}}/L_{\mathrm{turn}}$. Defining as well the time, relative to the time of one turn, it takes ions to reach the region of influence $\lambda_{\mathrm{inj}} = t_{\mathrm{injection}}/L_{\mathrm{turn}}$. Then the mass range diminishes to [Yavor et al., 2015]

$$\frac{m_{\mathrm{max}}}{m_{\mathrm{min}}} = \left(\frac{N + \lambda_{\mathrm{inj}}}{N + \lambda_{\mathrm{inj}} - (1 - \lambda_{\mathrm{mir}})} \right)^2 \tag{2.36}$$

Assuming $r_{\mathrm{usable}} = 75\%$, the mass range for $N = 10$ is $m_{\mathrm{max}}/m_{\mathrm{min}} \approx 1.17$, and $m_{\mathrm{max}}/m_{\mathrm{min}} \approx 1.015$ for $N = 100$. For the application as isobar separator or for nuclear physics mass measurements, this limitation isn't particularly problematic, the ability to achieve very high resolving powers in compact space outweighs it easily.

2.5. Ion Preparation for Time-of-Flight Mass Spectrometry

As discussed before, the performance of a time-of-flight mass spectrometer strongly depends on the ion population injected due to turn-around time and remaining aberrations. Additionally, ions from the RIB facility have to be captured, mixed with calibrant ions, in the case of separator setups recaptured and ejected to the further experiments.
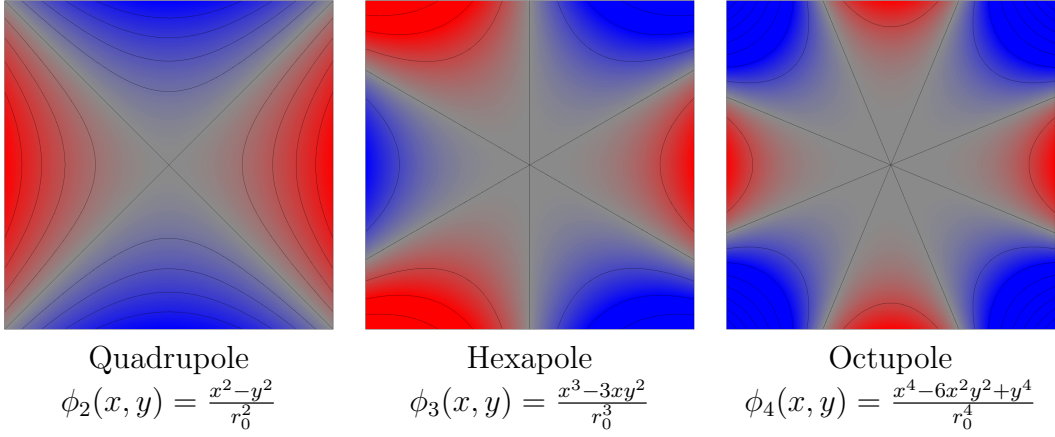
The standard method for this task are radio frequency quadrupoles (RFQ) since they allow storage, transport and thermalisation of ions as well as their injection into electrostatic systems.

2.5.1. Ion Storage in Radio Frequency Quadrupoles

Since confinement of ions is needed in two dimensions while allowing for transport in the third, only the case of two-dimensional fields will be considered. In Cartesian coordinates, 2D electric potentials $\Phi(x, y)$ can be expanded as

$$\Phi(x, y) = \sum_{N=0}^{\infty} A_N \phi_N(x, y) \tag{2.37}$$

where A_N is the amplitude of the multipole $\phi_N(x, y)$ [Douglas et al., 2005]. The cases ϕ_0 and ϕ_1 are a constant potential and a dipole and are not able to store ions. For the intended use, the most relevant potentials are quadrupole, hexapole and octupole potentials.

Quadrupole	Hexapole	Octupole
$\phi_2(x, y) = \frac{x^2 - y^2}{r_0^2}$	$\phi_3(x, y) = \frac{x^3 - 3xy^2}{r_0^3}$	$\phi_4(x, y) = \frac{x^4 - 6x^2y^2 + y^4}{r_0^4}$

Trapping with higher orders is also possible, up until to structures like the RF funnel or carpet which is used for example in gas-filled stopping cells [Savard et al., 2003, Neumayr et al., 2006]. Disadvantageous in the case of a system for ion preparation for a TOF mass spectrometer is the progressively flatter potential in the storage area of the ions, leading to a broader ion population and therefore a larger phase space. This, combined with the need for more electrodes to generate the required fields, leads to the use of quadrupolar potentials.

To generate the required quadrupole potential, electrodes in a chosen minimal distance r_0 from the origin and in the shapes given by the equipotential contours $\phi_2(x, y) = \pm 1$ can be used. In practice, especially in applications where ion transport and not quadrupole mass spectrometry is the focus, round rods are widely used due to ease of manufacturing and positioning. This adds higher orders to the quadrupole potential. The best approximation has been found to be for $r_e/r_0 \approx 1.13$ [Douglas and Konenkov, 2002, Gibson and Taylor, 2001]. Since the electrode surface was defined as being $\phi_2(x, y) = \pm 1$, A_2 is the potential applied to the electrodes.

The electric field corresponding to the quadrupole potential is given by

$$\vec{E}(\vec{r}) = -\nabla\Phi(\vec{r}) \qquad (2.38)$$

and the non relativistical equation of motion is

$$m\frac{d^2\vec{r}}{dt^2} = Qe\vec{E}(\vec{r}) \qquad (2.39)$$

Using Equation 2.38, the equation of motion becomes

$$m\frac{d^2\vec{r}}{dt^2} = \frac{2QeA_2}{r_0^2}\begin{pmatrix} -x \\ y \\ 0 \end{pmatrix} \qquad (2.40)$$

For the applied potential, two components are used, a constant and a sinusoidal.

$$A_2 = (U - V\cos(\Omega t)) \qquad (2.41)$$

Defining

$$a_x = -a_y = \frac{8QeU}{m\Omega^2 r_0^2} \quad ; \quad q_x = -q_y = \frac{4QeV}{m\Omega^2 r_0^2} \quad ; \quad \xi = \frac{\Omega t}{2} \qquad (2.42)$$

the equation of motion becomes the form of Mathieu equations

$$\frac{d^2u}{d\xi^2} + (a_u - 2q_u\cos(2\xi))u = 0 \qquad \text{with} \qquad u \in x, y \qquad (2.43)$$

The properties of the Mathieu equation are well understood. The trajectories can be expressed by

$$u = \alpha'e^{\mu\xi}\sum_{n=-\infty}^{\infty}C_{2n}e^{2in\xi} + \alpha''e^{-\mu\xi}\sum_{n=-\infty}^{\infty}C_{2n}e^{-2in\xi} \qquad (2.44)$$

where the integration constants α' and α'' depend on the initial conditions u_0, $\dot{u}_0$ and ξ_0 while the coefficients of the sums C_{2n} and the exponent μ are only dependent on a_u and q_u but not on the initial conditions. Therefore, a_u and q_u are sufficient to describe the general nature of the ion motion in the RFQ [Dawson, 1976].
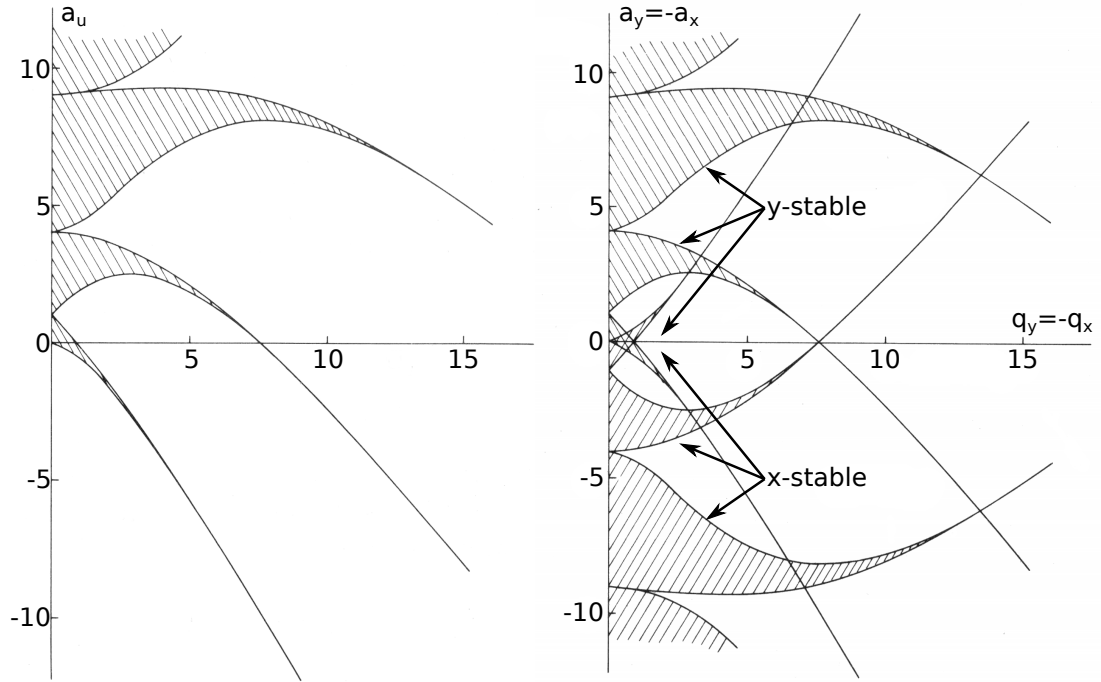
Figure 2.18.: Stability diagram for one coordinate and the combination of both coordinates in a linear RFQ. Figure modified from [Dawson, 1976].

Defining 'unstable' as having trajectories with finite amplitudes, for $Re(\mu) \neq 0$, the trajectories become unstable due to the $e^{\pm\mu\xi}$ factors. For purely imaginary $\mu = i\beta$ with β non-integer, periodic and stable solutions can be found. Integer β give periodic but unstable trajectories.

The simplest approximation for β is given in

$$\beta = \sqrt{a + \frac{q^2}{2}} \tag{2.45}$$

Plotting regions with stable trajectories in respect to a_u and q_u, the stability diagram for one direction can be generated. Since $q_x = -q_y$ and $a_x = -a_y$ for the linear RFQ, the resulting stability diagram for the second direction is mirrored along the axes (Figure 2.18). Where both stability regions overlap, ion trajectories are stable in both x and y and therefore stored. For practical reasons, the first region of stability with $q \leq 0.908$, shown in Figure 2.19, is almost exclusively used. The upper q limit gives the low mass cutoff for storage. Higher masses do not experience a cut off, their storage is limited by the depth of their pseudopotential as discussed in the next section.

As can be seen in Equations 2.42 and 2.44, the ions oscillate in the RFQ with a superposition of the frequencies
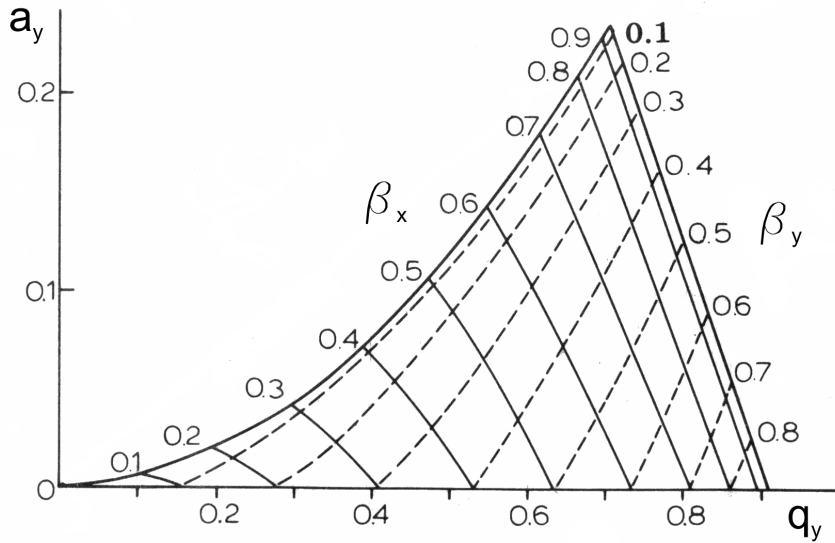
Figure 2.19.: Stability diagram of the first stability region for the linear RFQ. Shown are also iso-β-lines. Figure modified from [Dawson, 1976].

$$\omega_n = \left(n + \frac{\beta}{2}\right)\Omega \qquad \text{with} \qquad n \in \mathbb{Z} \qquad 0 \leq q \leq 1 \tag{2.46}$$

The fundamental mode with $n = 0$ usually has the largest coefficients resulting in large amplitude but slow macromotion and a small amplitude but fast micromotion with the higher frequency orders.

2.5.2. Pseudopotential

In the case of low q and $a = 0$, the coefficients for higher harmonics than $n = 0$ get insignificant against the fundamental mode and the ions' motion can be approximated [Dehmelt, 1967] as a harmonic oscillation with the frequency

$$\omega_0 \approx \frac{q\Omega}{\sqrt{8}} \tag{2.47}$$

Using this approximation, the ions can be seen as if confined in a pseudo-potential of the form

$$V_{\text{pseud}}(r) = D_{\text{pseud}}\left(\frac{r}{r_0}\right)^2 \tag{2.48}$$

with

$$D_{\mathrm{pseud}} = \frac{qV}{4} \qquad (2.49)$$

This pseudopotential approach allows several insights into the behaviour of ions in an RFQ. Comparing the pseudopotential with the electrostatic potential generated by the trapped charge allows to gauge ion capacity. While catching ions in an RFQ, the maximum permissible kinetic energy of the ions can be estimated. For high masses, the pseudopotential is decreasing with $D_{pseud} \propto m$ which explains why also high masses are lost from the RFQ even though the stability boundaries seem to allow their storage.

2.5.3. Buffer Gas Cooling

As can be seen from Equation 2.44, the parameters of the stable ion motion inside of the RFQ are not time dependent, meaning a bunch of ions injected into the RFQ will keep their average kinetic energy. Reduction of average kinetic energy is important in order to stop the ions after electrostatic transport, highly efficient transport through small apertures and to achieve high phase space densities for injection into an TOF analyzer and therefore high resolving powers. There are several techniques to achieve this goal [Itano et al., 1995]. In the case of ions trapped in an RFQ, collisional cooling is the fastest and easiest option.

For cooling, a controlled amount of a selected buffer gas is introduced into the RFQ, reaching an equilibrium pressure. In the case without RF introduced into the system, the ions would interact with the gas, thermalize and reach the temperature of the gas. As is to be expected, the effect of the collisions on the ions is dependent on the relative velocity in the collisions and the masses of ion and gas particle. Due to the high momentum exchange, large gas masses lead to fast cooling. Considering applied RF, the equilibrium temperature is higher than the temperature of the buffer gas due the forced motion of the ions in the gas by the RF (RF heating). The mass of the ions has to be larger than the mass of the gas particles [Moriwaki et al., 1992]. The velocities, at which the collisions occur, are generally lower for low q values due to the smaller contribution of micromotion to the ion velocities. For large ion populations, due to space charge effects, more ions can be found in higher distance of the trap center and therefore higher fields and higher velocities [Plaß, 2001].

Charge exchange reactions between the neutral buffer gas and the ions in the trap usually lead to the loss of the trapped particle. This limits the use of collisional cooling to ions of low charge states and contributes to a loss of ions over time. Since the probability for charge exchange depends on the ionization potential, buffer gases of high ionization potential are preferred. Usually noble gases are selected, for some applications nitrogen or even dry air can be considered too.

Aside from the higher charge exchange probability, contamination of the gas (for example by water or hydrocarbons) can lead to adducts on the particles of interest.

Advantages of collisional cooling are its universal applicability, its relative ease of application and fast cooling times. Disadvantages are the need for axial potential gradients to move the ions around (see next section), charge exchange reactions and the need for differential pumping stages between RFQs and electrostatic transport sections.

2.5.4. Longitudinal Ion Control in Gas-Filled RFQs

In an RFQ in vacuum, the axial component of motion is preserved. The effect of the introduction of a buffer gas can be seen as some coupling of the RF induced motion into the z direction and drag reducing the initial ion motion to rest. While ion transport without an additional field is still possible in case of relatively high ion currents due to space charge introduced by newly arriving ions, this method would be slow, only works for high currents and is prone to local potential minima in inhomogenous sections of the RFQ in which ions would be trapped and can be lost.

The solution to this problem is the introduction of a longitudinal electric field that drags the ions through the gas. As the electrostatic force on the ion is constant but the strength of the ion-gas interaction increases with velocity, the ions reach a mean velocity, the drift velocity [Tolmachev, 1997].

$$v_d = \mathcal{M} E_d \tag{2.50}$$

$\mathcal{M}$ is called the electrical mobility. The mobility is dependent on the ion and gas selected and inversely proportional to the gas pressure.

Selection of the gas parameters requires weighing the parameters of the gases, especially pressure, relative molecular weight to the ions, ionization potential (influences the charge exchange probability) and its diffusion coefficient, with the requirements in the experiment. A high drift velocity is beneficial for fast transport of ions over longer distances, while it also results in higher kinetic energies which requires higher stopping potentials at apertures. Additionally the cooling time

$$\tau = \frac{m\mathcal{M}}{Q} \tag{2.51}$$

that is required for ions to asymptotically reach an equilibrium is a limit for
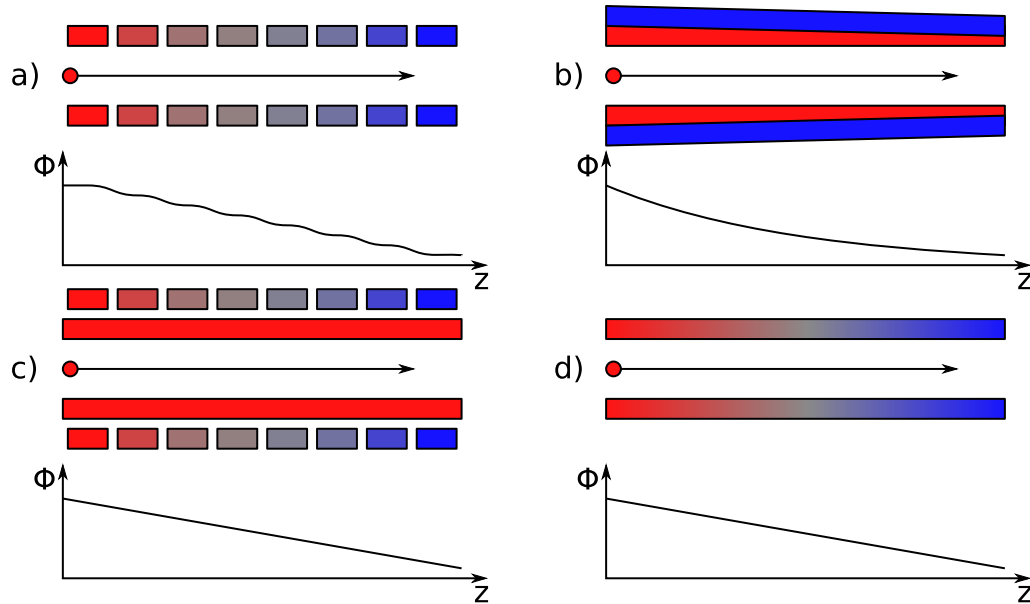
Figure 2.20.: Schematic of the four presented methods for generation of a longitudinal gradient in a RFQ: a) Segmented RFQ b) LINAC electrodes c) Outer DC electrodes d) Resistive RFQ.

operation cycle times [Tolmachev, 1997]. For reduction of transport times, it is of course also possible to increase the dragging field. This has the disadvantage that the potential drop across the instrument increases which might be problematic depending on the method for gradient production. An additional disadvantage of increasing gas pressures is the proportional increase in gas load for the differential pumping stages, leading to either need for larger pumps or pressures in UHV-regions with the associated decrease in performance.

There are several methods to implement a longitudinal electric field along a RFQ (Figure 2.20). The probably most commonly used method is to segment the RFQ rods into smaller pieces and to apply a different DC offset to each segment [Dodonov et al., 1997, Javahery and Thomson, 1997]. In order to achieve a constant field in the center of the RFQ, the segment size has to be small against the r_0 of the RFQ. Since production and alignment of many segments and the corresponding contacts or voltage divider is cumbersome, typically larger segments are selected. This leads to field fluctuations.

Another common method is the introduction of a set of additional *Linac* electrodes into the RFQ [Loboda et al., 2000, Mansoori et al., 1998]. Those electrodes are usually four narrow strips of metal that are brought between the RFQ rods in a way that they reach into the RFQ a bit further on one end of the RFQ than on the other. When the potential of the Linac electrodes is selected differently than the DC potential of the RFQ rods, the differing field penetration into the RFQ generates a DC gradient on axis. In the case of straight electrodes, the DC potential on axis becomes approximately quadratic. By shaping the electrodes, this effect can be reduced. Unfortunately, manufacturing for a robust system is

requires very tight tolerances, even more so for small r_0. The quadrupole field is also altered by the electrodes, one end will experience smaller RF amplitudes, influencing the RFQ parameters slightly. The potentials are highly dependent on electrode positions so that the exact potentials on axis are usually not fully known and relatively large steps on entrance and exit of the Linac RFQ are required, introducing ion heating.

A further method relies on the field penetration through the RFQ rods by placing additional electrodes outside of the RFQ [Thomson and Jolliffe, 1998]. Advantage are the high field linearities and relative ease of manufacturing, disadvantage are required high voltages, unknown center potential and problems in interfacing several instrument parts.

Resistive RFQs are a new method [Takamine et al., 2007, Simon, 2008] using a material with suitable resistance that is connected on both ends and fed with differing DC offsets but the same RF instead of the low resistance electrodes of classic RFQs with typically just one contact. This can be seen as the limit of the segmented RFQ solution with infinitely short segments. Since the voltage division is done internally in the rods, the cumbersome contacting of 10s to 100s of segments is not needed. Also a large variety of RFQ forms can be produced at relative ease. Bends or, in the case of this work, the RFQ switchyard, are very difficult to achieve using segmented RFQs or Linac systems. The disadvantage of this technique is the need for special materials in vacuum to achieve the needed resistance which is given due to the DC-RF-mixing, gradient power supplies and power dissipated in vacuum. Additionally, inhomogeneities in the rods can lead to non-linear fields. Fortunately, possible DC quadrupole components due to inhomogeneities are not significant against the RF due to their low strength.

3. Conception of an Isobar Separator for TITAN

3.1. The TITAN Setup

TRIUMF's Ion Trap for Atomic and Nuclear science (TITAN) [Dilling et al., 2003] is a combination of different types of ion traps situated in the low energy section of ISAC. It currently consists of an RFQ cooler and buncher, an EBIT and a Penning trap (Figure 3.1.

The RFQ cooler and buncher [Brunner et al., 2012] is a segmented RFQ to which RF and DC potentials can be applied to exert radial and longitudinal confinement. The DC beam from ISAC is slowed down electrostatically to a few eV and injected into the RFQ which sits at ISAC source potential. Buffer gas dissipates the residual energy and thermalizes the ions, after which they can be ejected either backwards (i) to setups like the laser spectroscopy [Mané et al., 2011] or, with adjustment of the reference potential by a pulsed drift tube, further into the TITAN setup.

Here, direct transport (ii) into the high precision 4 T measurement Penning trap (MPET) is possible. The MPET is the main instrument for mass measurements. TOF-ICR is used as a measurement scheme.

As shown in Equation 2.7 and Figure 3.2, increase in charge state reduces the required measurement times in a Penning trap. This can be achieved with an Electron Beam Ion Trap (EBIT). An EBIT uses a constant magnetic field to confine ions radially and a set of electrodes to generate an electric field for longitudinal confinement. A strong electron beam (several $100\,\text{mA}$ and $10s\,\text{keV}$) can be introduced into the trap and increases, due to its space charge, the radial confinement. In collisions with the electrons at kinetic energies of up to 70 keV, the electrons of the confined ions are sequentially stripped away in collisions, forming a population of highly charged ions which can serve for spectroscopy experiments (iii) or transported further for mass measurement (iv). Required time for charge breeding, losses during breeding and the charge state distribution reduce efficiency in comparison to direct mass measurement. Another mode for the EBIT setup is as an open frame Penning trap to study decays of the trapped species [Gallant et al., 2010].

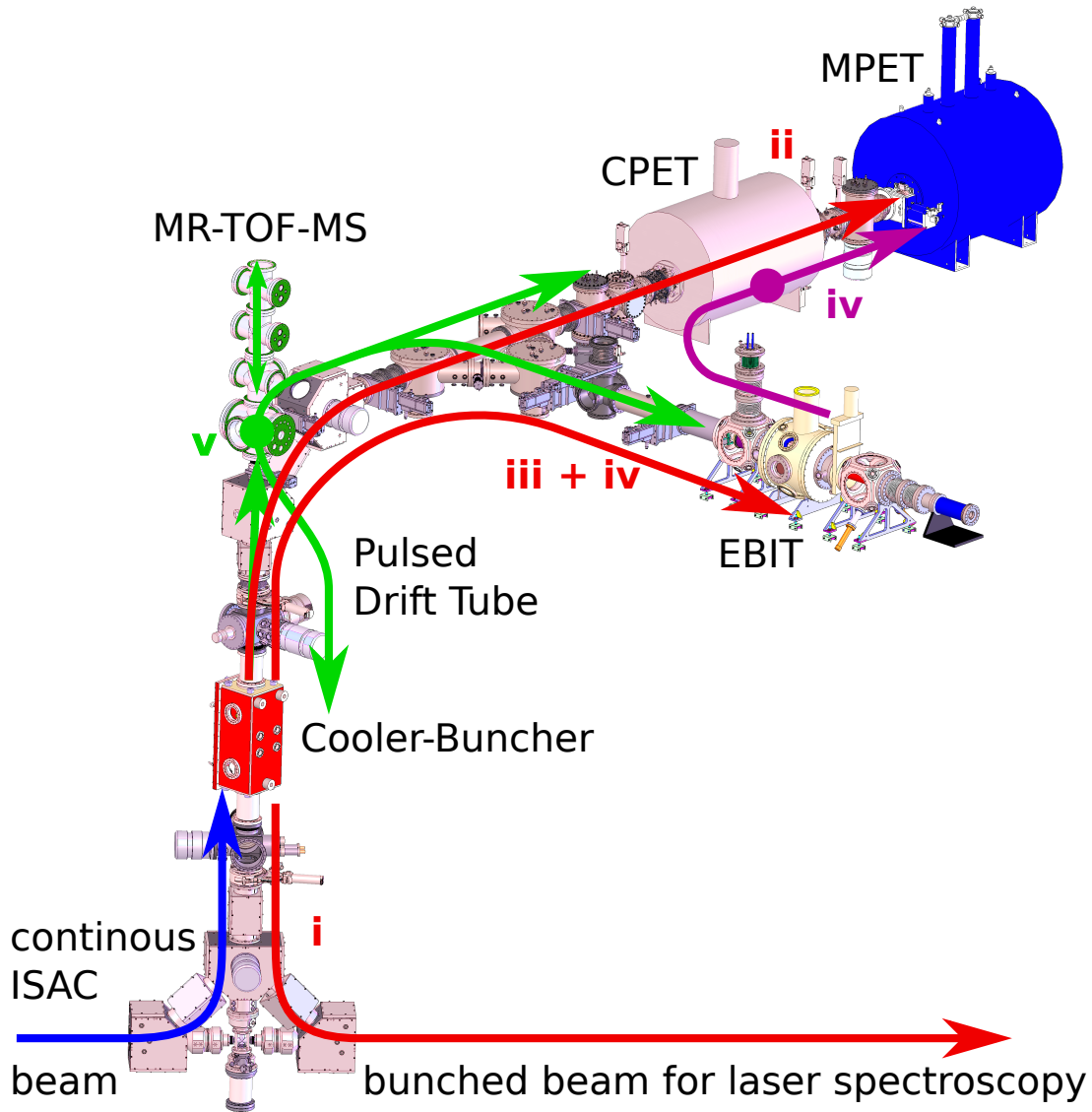The breeding process generates energy spreads of the ions of tens of electronvolt

Figure 3.1.: Layout of the TITAN facility including the upgrades of MR-TOF-MS
and the CPET. Continuous beam is shown in blue, singly charged
bunched ions are shown red, highly charged ions in purple. Singly
charged ions processed by the MR-TOF-MS are shown in green. De-
scription of the different modes in the text. Not shown are the racks
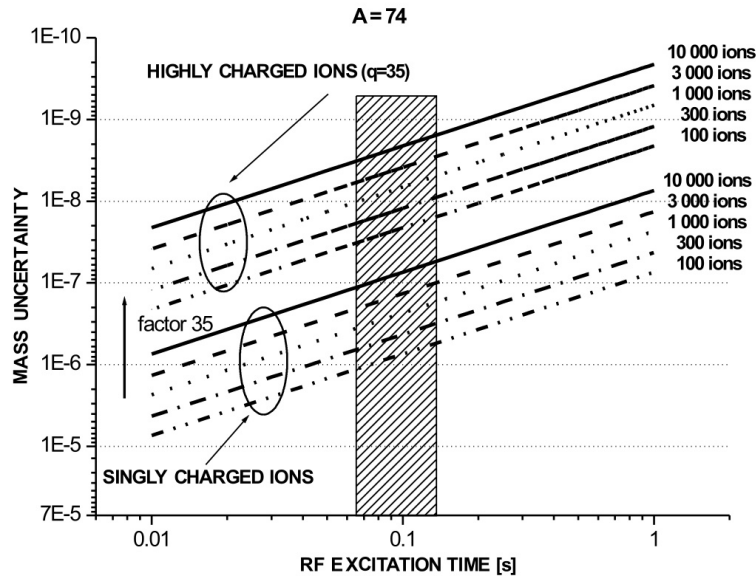and Faraday cages on the TITAN platform needed for operation.

Figure 3.2.: Mass uncertainty in a Penning trap measurement in dependence on RF excitation time, number of detected ions and their charge state [Dilling et al., 2003].

which is detrimental to the measurement precision in the Penning trap. It is intended to cool the ions in an further Penning trap using sympathetic cooling with protons or electrons. Again, charge exchange reactions reduce efficiency [Simon et al., 2011].

3.2. Choice of Separation Method and Integration of the new MR-TOF-MS into TITAN

As discussed in section 2.1, MR-TOF-MS allows fast isobaric separation at high capacities and additionally non-scanning, fast mass spectrometry for very short lived nuclides. Therefore, MR-TOF-MS is an ideal addition to the TITAN setup.

The following features and performance parameters are required for the new instrument:

- Isobar separation with a resolving power of $\geq 20,000$ after $10\,\mathrm{ms}$. This will bring a large percentage of nuclides from the yield tables that were previously not available into reach (see Figure 2.8)

- Mass spectrometry resolving power $\geq 100,000$ in order to perform direct mass measurement for very short lived nuclei

- Ion capacity of $\geq 10^4$ ions per cycle allowing for large ratios of contamination to nuclide of interest

- Operating frequency up to $100\,\mathrm{Hz}$ resulting in short measurement times for short lived species and, in combination with the ion capacity per cycle, high throughput

- A mass range of $15 - 230\,\mathrm{u}$

- Transmission efficiency $\geq 20\%$

- Residual gas pressure $\leq 3 \cdots 10^{-6}$mbar in the RFQs of the MR-TOF-MS, resulting in a storage time of Argon of $T_{1/2} = 10\,\mathrm{ms}$. This prevents large losses due to charge exchange reactions

- Input potential for ions from the TITAN RFQ buncher of about 1510 V, output potential of about 1490 V to be able to integrate into the TITAN beamline

Additional requirements are imposed from the current setup of the TITAN facility. Positioning the MR-TOF-MS behind the RFQ cooler and buncher and the pulsed drift tube allows to work at lower potentials, simplifying the electronics needs. The needed racks and Faraday cages located on the TITAN platform further limits the options for placement.

Possible spaces for inclusion on the platform would be between the 45° bends onto the platform and around the electrostatic switchyard between the mentioned bend, EBIT and the Penning traps. The area of the 45° bends was chosen since here an inclusion with very little modification of the beamline is possible and a larger distance between the additional buffer gas introduced by the system and the highly charged ions allows better differential pumping.

Placement as shown in Figure 3.1 allows the use of of the MR-TOF-MS for isobar separation in all modes available on the TITAN platform: (i) Delivering bunched beams for laser spectroscopy (ii) Mass measurement in the MPET without charge breeding (iii) X-ray spectroscopy or decay measurements in the EBIT (iv) Charge breeding in the EBIT, cooling in the CPET and mass measurement of highly charged ions in the MPET. (v) Additionally, direct mass measurement in the MR-TOF-MS is available for very short lived nuclides or for diagnostic purposes.

The already implemented MR-TOF-MS devices use a fast ion gate to spatially separate the temporally separated ions [Dickel et al., 2015]. In order to apply this concept in the TITAN MR-TOF-MS, a second ion transport from the analyzer into the TITAN beamline would be needed. The constraints set by the existing setup make this all but impossible. By using the novel concepts of the RFQ switchyard and mass-selective retrapping, it becomes possible to use the path already used for transport into the analyzer also for transport of the ions back

into the TITAN beamline. In combination with the multiple reflection analyzer, the time-focus shift mode and the mass range selector, a powerful instrument can be built.

3.3. The Essential Techniques of the TITAN MR-TOF-MS

3.3.1. RFQ Switchyard

Bent metallic RFQs [Plaß et al., 2007] and bent resistive RFQs [Simon, 2008] allowing axial fields have been produced before. In those, selection of ion paths is possible by mechanical movement of RFQ paths. Also injection of ions through an electrode into the RFQ of a bent RFQ has been performed. This allows transport of ions to different detectors as well as the introduction of reference ions.

A consequential development is an RFQ device capable of directing the ions from arbitrary input ports to arbitrary output ports at high efficiencies. Additional options might be distributing ions with variable ratios and mixing several input ports.

This is achievable by connecting several RFQs leading into an intersection. Application of RF fields then generates a pseudopotential confining the ions to connected paths in the middle. Additional DC gradients along the RFQs then allow the selection of transport directions.

The solution implemented for the TITAN MR-TOF-MS uses a structure with square profile resistive RFQs. By applying the appropriate potentials on the RFQ ends, different paths across the switchyard can be selected [Greiner, 2013, Plaß et al., 2015]. In Figure 3.3, a simulation of ion transport around a right angle bend can be seen.

Standard orientation of RFQs in the system are 'on point'. Unfortunately this geometry is not possible for the switchyard since, as shown on Figure 3.4 (i). For this geometry, two RFQs would have only one phase of RF applied. While a four-port solution would be possible, this was deemed one port less than required as input, output, transfer, source and detector need to be coupled to the switchyard. A feasible solution is the (ii) 'on edge' orientation which results in three-legged RFQ segments that also have the advantage of providing better mechanical stability.

Options were to either reorientate all other RFQ structures in the system or to couple RFQs with 45 degree differing angles. Simulations with the program IT-SIM [Plaß, 2001] have shown that minimal ion heating is present at the transitions
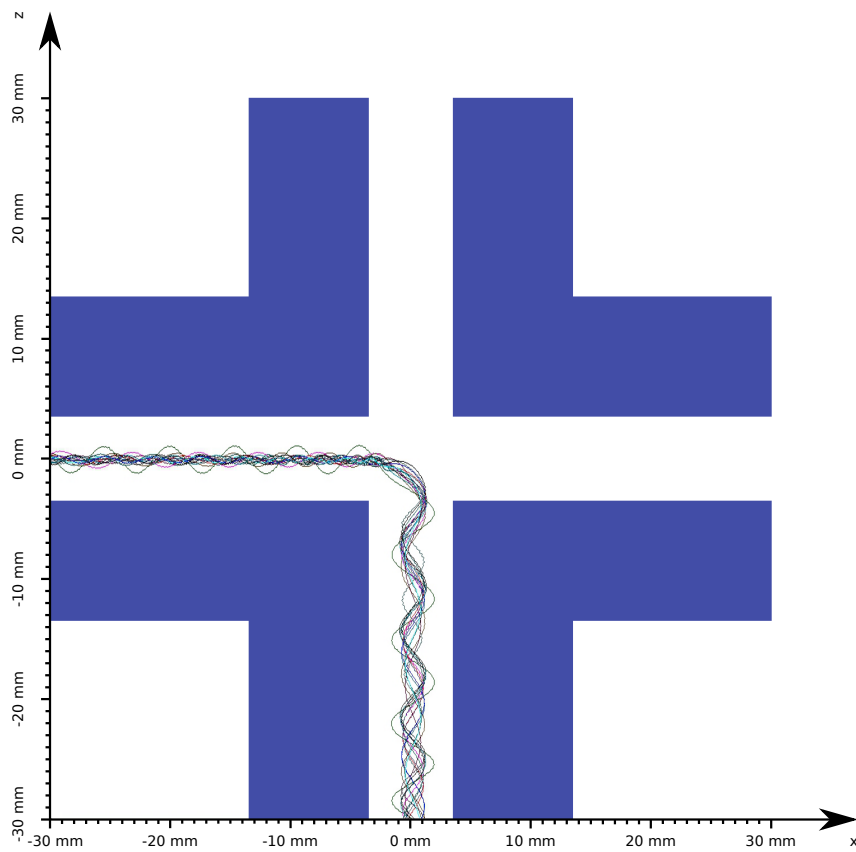
Figure 3.3.: Simulation of ions in the switchyard, being transported around a right angle bend.
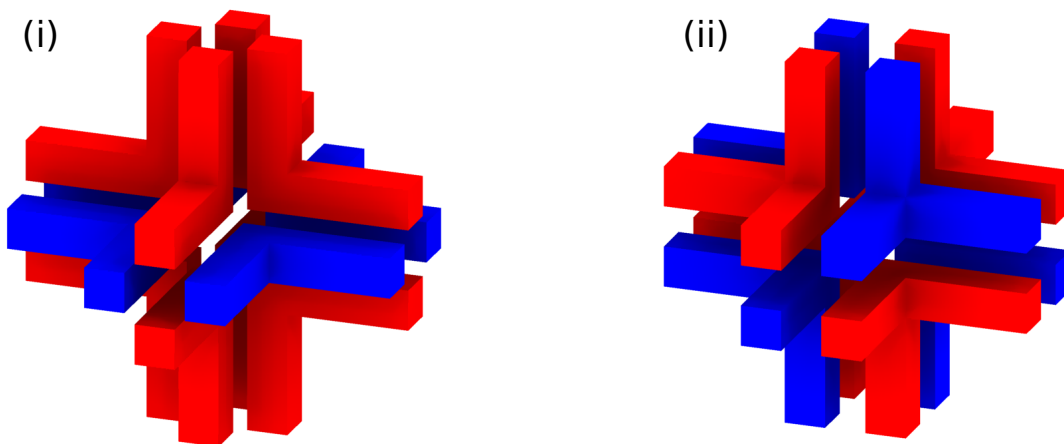

Figure 3.4.: The conceivable options for the coupling of six RFQs into a switchyard. The (i) 'On Point' structure does not allow six RFQs since both top and bottom RFQ only receive one phase of RF. The (ii) 'On Edge' structure is suitable though.
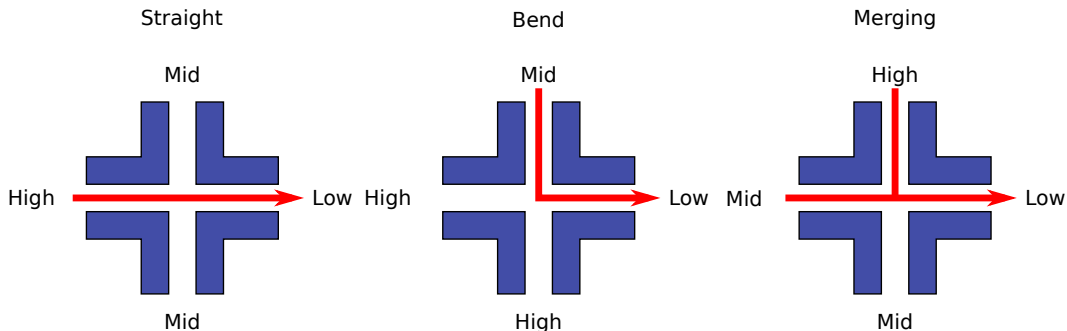
Figure 3.5.: Potentials required for the modes straight, bend and merge.

so the solution of coupling RFQs or different orientations was chosen.

While optimal solutions could be obtained by feeding separate DC potentials to all three contacts of each of the 8 electrodes. However this increases the amount of needed feedthroughs and potentials and is unpractical. By combining the DC potentials of all four contacts per side of the switchyard, the complexity can be reduced and the results are still sufficient. For operation, three potentials are needed in order to generate a dragging field without potential pockets for all possible cases as can be seen in Figure 3.5. By switching the DC potentials on the switchyard, cycle-based selection of input and output ports is possible.

Ports of the switchyard are additionally equipped with large apertures in order to apply strong blocking potentials since the potential gradients of the switchyard have to be chosen relatively small due to limitations of electronics and available resistive material.

3.3.2. Analyzer

As discussed in subsection 2.4.4, multiple-reflection TOF analyzers consist of two or more reflectors that confine ions on a path while keeping the isochronicity of the ions. The analyzer of the TITAN MR-TOF-MS is a rebuild of the analyzer for a mobile MR-TOF-MS for applications in analytical mass spectrometry [Lang, 2016, Dickel et al., 2013] which in turn is a scaled version of the MR-TOF-MS analyzer used in the Ion Catcher Setup [Dickel et al., 2015]. It employs the closed path technique with two gridless, rotationally symmetric electrostatic mirrors and in- and ejection through pulsed endcaps.

For one reflection of an ion from the middle plane of the analyzer with the inital parameters $x_0, a_0, ...$, the aberration expansions read

$$x = (x|x)x_0 + (x|a)a_0 + (x|x\delta)x_0\delta + (x|a\delta)a_0\delta \ ... \tag{3.1}$$
$$a = (a|x)x_0 + (a|a)a_0 + (a|x\delta)x_0\delta + (a|a\delta)a_0\delta \ ... \tag{3.2}$$
$$y = (y|y)y_0 + (y|b)b_0 + (y|y\delta)y_0\delta + (y|b\delta)b_0\delta \ ... \tag{3.3}$$
$$b = (b|y)y_0 + (b|b)b_0 + (b|y\delta)y_0\delta + (b|b\delta)b_0\delta \ ... \tag{3.4}$$
$$\begin{aligned}
t = \ & (t|\delta)\delta + (t|\delta\delta)\delta^2 + (t|\delta\delta\delta)\delta^3 + (t|\delta\delta\delta\delta)\delta^4 \\
& + (t|xx)x_0^2 + (t|xa)x_0a_0 + (t|aa)a_0^2 + (t|yy)y_0^2 + (t|yb)y_0b_0 + (t|bb)b_0^2 \\
& + (t|xx\delta)x_0^2\delta + (t|xa\delta)x_0a_0\delta + (t|aa\delta)a_0^2\delta \\
& + (t|yy\delta)y_0^2\delta + (t|yb\delta)y_0b_0\delta + (t|bb\delta)b_0^2\delta \ ...
\end{aligned} \tag{3.5}$$

By optimizing electrode geometry and potential [Yavor et al., 2015], energy focusing up to the third order can be achieved:

$$(t|\delta) = (t|\delta\delta) = (t|\delta\delta\delta) = 0 \tag{3.6}$$

When the reflector is tuned to parallel-to-point imaging

$$(x|x) = (y|y) = 0 \tag{3.7}$$

the first order aberrations for the angles disappear due to the mirror symmetry of the system

$$(a|a) = (b|b) = 0 \tag{3.8}$$

Then, the second order aberrations of the flight time can be tuned to a focus

$$(t|xx) = (t|aa) = (t|yy) = (t|bb) = 0 \tag{3.9}$$

After completing a full turn, two reflections, additionally the dependencies of position to angle and vice versa disappear

$$(x|a) = (a|x) = (y|b) = (b|y) = 0 \tag{3.10}$$

and with them the remaining second order flight time aberrations
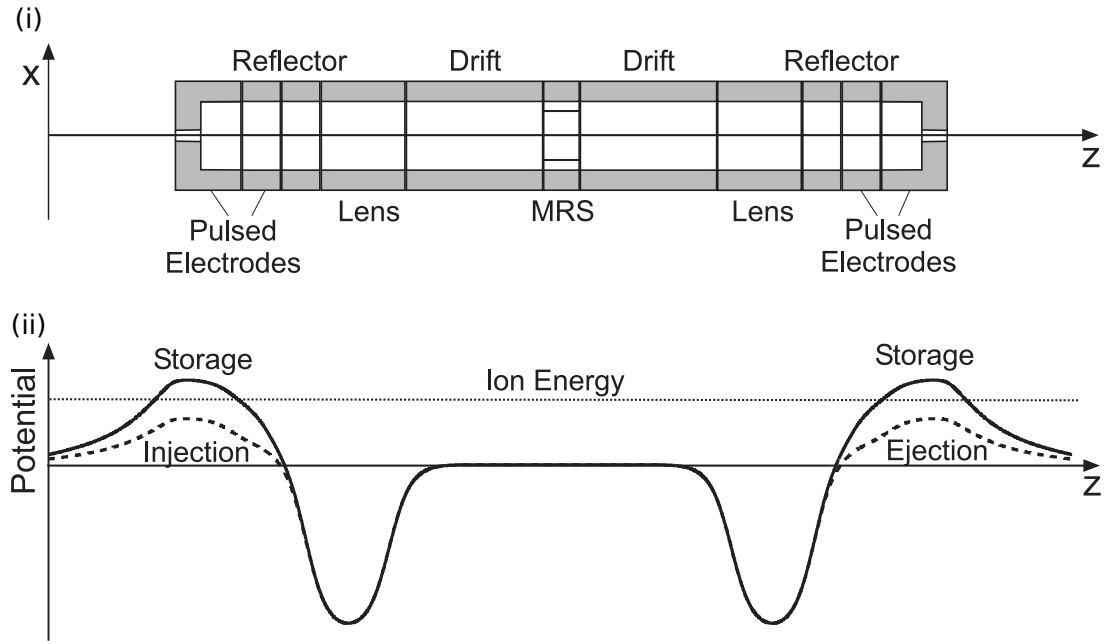
$$(t|xa) = (t|yb) = 0 \tag{3.11}$$

Figure 3.6.: (i) Schematic of the analyzer. (ii) Potentials on the optical axis for storage and injection of ions [Dickel et al., 2015].

Fulfilling the conditions in Equations 3.7 to 3.11 results in cancellation of

$$
\begin{aligned}
(x|x\delta) = (x|a\delta) = (a|x\delta) = (a|a\delta) = \\
(y|y\delta) = (y|b\delta) = (b|y\delta) = (b|b\delta) = 0
\end{aligned}
\tag{3.12}
$$

due to the symplectic conditions [Wollnik and Berz, 1985].

The main remaining aberrations to the time of flight after optimization are the fourth order aberration in energy $(t|\delta\delta\delta\delta)$ and the third order mixed aberrations $(t|xx\delta), (t|aa\delta), (t|yy\delta), (t|bb\delta)$.

The structure of the analyzer found by optimization of geometry and potentials is then a symmetric system of two mirrors consisting of 4 electrodes each, the end cap (E1) which forms the mirror potential together with two ring electrodes (E2 and E3) and the lens electrode (E4). The drift electrode (E5) connects the mirrors, the naming scheme is then continued for the second mirror with lens (E6) and the electrodes up to the endcap (E7, E8, E9). A schematic of the analyzer and the potential inside can be seen in Figure 3.6.

3.3.3. Time-Focus Shift

Achieving a time focus on the detector is requirement for narrow peaks and hence high resolving powers as described in section 2.4.2. Usually, separate tuning of the analyzer is required for changed numbers of turns in the analyzer. This makes optimization and successive increase of the resolving power cumbersome. A solution for this problem is the use of an additional Post Analyzer Reflector (PAR) [Plaß et al., 2008].

This method is applied in the MR-TOF-MS of the FRS Ion Catcher which will later be discussed in chapter 6. Here, the time focus is tuned so that it rests in the middle of the analyzer for every turn. In order to reach high resolving powers at the detector or ion gate location, an additional reflector, the Post Analyzer Reflector, is placed behind the analyzer. It projects the time focus from the middle of the analyzer in the required plane of detector and ion gate [Yavor et al., 2015].

The solution of the PAR requires positioning the detection and separation electrodes to the side of the analyzer and quite some additional space for a second RFQ system, transporting the ions back out of the instrument. For setups limited in size as the MR-TOF-MS for in situ applications AmbiProbe [Lang, 2016, Dickel et al., 2013] and the TITAN MR-TOF-MS, this is impossible. Here, a different solution has been found.

The analyzer is kept in a mode were the location of the time focus is preserved independent on the number of turns for a selectable number of turns. This setting is called the multiturn mode (MT). For a fixed time in every cycle, the analyzer is switched to a different set of potentials. Serving the same purpose as the PAR, the additional set of potentials shift the time focus onto the detector. This mode is called the time focus shift mode (TFS).

3.3.4. Mass Range Selector

As shown in subsection 2.4.4, closed path multiple-reflection instruments suffer from a limited unambiguous mass range. While it is in principle possible to disentangle the mass spectra of different turn numbers by acquisition of several spectra at varied flight times, the more reliable and, especially for isobar separation, advantageous solution is to limit the mass range that can be transmitted in the analyzer.

This is performed by the mass range selector (MRS), a set of four electrodes in the center of the analyzer. By putting a deflection potential on opposing electrodes, the beam in the analyzer can be deflected out of the acceptance of the analyzer. If this is performed periodically in phase with the motion of the ions in the analyzer, ions of strongly differing masses from the mass range of interest are continuously
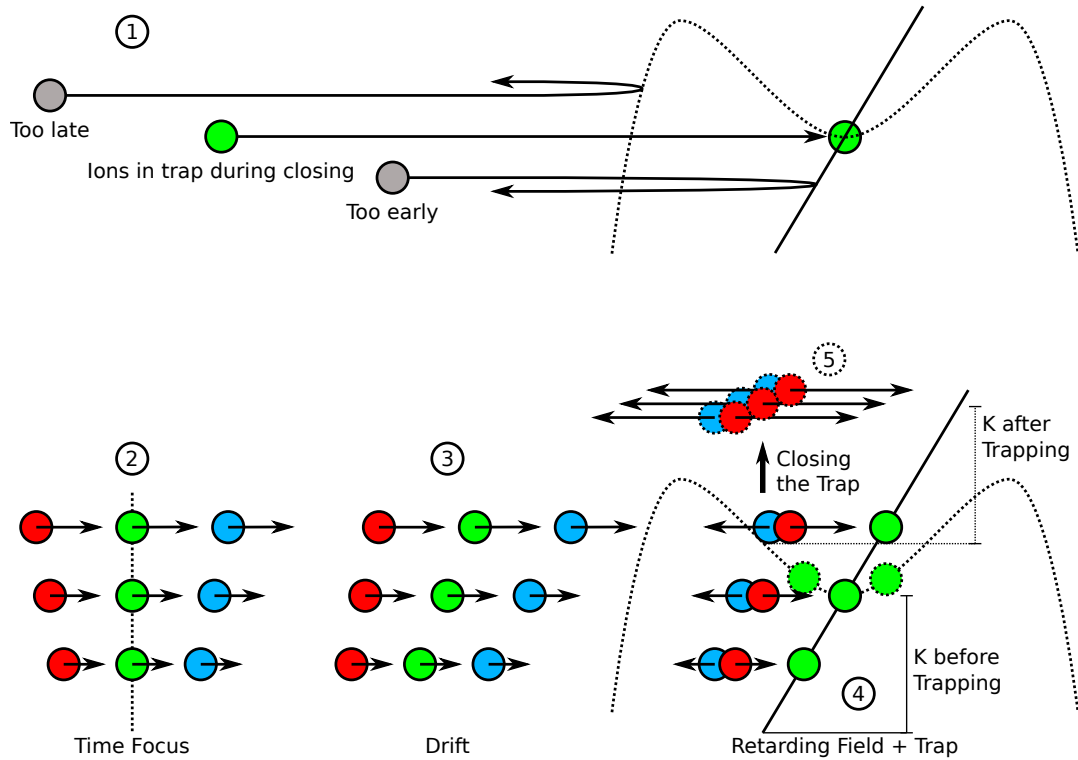
Figure 3.7.: Concept of mass-selective retrapping. (1) Ions at closing time, that have not entered the trap region or already left it again after reflection, are reflected back into the system. For ions that are in the trap region while closing the trap, further consideration is required. Past their last time focus (2), the ions travel a certain distance (3) and, in first order approximation, come to rest in the linear field of the trap at a certain time (4). Other ions, shown here in red and blue, still posses kinetic energy and have not reached the center of the trap. By switching to the storage field, the ions of interest stay almost at rest while ions before and with their residual energy are not stored anymore and lost (5). The separation capability therefor depends on the dispersion of the analyzer, the trap depth and the parameters of the retarding field in which the ions come to rest.

removed from the analyzer. In order to maximize the mass range available for measurement and reduce influence on the ions of interest, the MRS is switched off a few turns before the ejection of the ions from the analyzer. This way, the ions can expand for those last turns in the analyzer [Dickel et al., 2015].

Additionally, the MRS electrodes can be used as steerers in the case of misalignments of the instrument.

3.3.5. Mass-Selective Retrapping

Placement of a fast ion gate like a Bradbury Nielsen gate [Bradbury and Nielsen, 1936] in a time focus is the method of separation used in the MR-TOF-MS of the FRS Ion Catcher. In the TITAN setup, implementation of a setup like this with additional ion mirror, BNG and retrapping RFQ is not possible due to space constraints. Due to the availability of the switchyard, using the same RFQ for transport to and from the analyzer becomes an option. The solution intended for spatial separation of the temporally separated ions is mass-selective retrapping in the injection trap.

Intuitively, this separation method can be understood as shown in the top part of Figure 3.7: Three ions of different species are temporally separated in the analyzer. Both ions that arrive too early or too late are reflected by the trap potential and are not present in the trap region during closing. This gives a minimum resolution as can be seen. In reality, the achievable resolution is even higher. Ions of higher energy travel further in the retarding field. This is, assuming conservative potentials between ejection and retrapping, the reverse of the effect of the ejection, see section 2.4.2.

In first order approximation, at each time of closure for the trap, a certain mass is at rest in the trap, at different locations. Particles of heavier and lower masses are still in the process of slowing down in the retarding field or accelerated out again. After closing the trap, this results in a distribution of ions that are almost at rest inside the trap region or still possess higher kinetic energies, depending on their arrival time and, via the dispersion of the analyzer, on their mass. By choosing a shallow trapping potential, ions with kinetic energies above the potential are not stored and lost, remaining in the trap are the ions of interest. Beside selecting the trap potential, the field strength of the retarding field is also relevant since it influences the amount of potential change and residual kinetic energy at closing time [Yavor, 2011, Lang, 2016].

3.4. Conceptual Design of the TITAN MR-TOF-MS

As a result of these conceptual considerations, a new device, the TITAN MR-TOF-MS, has been designed. Ions are injected into the system from the cooler-buncher below. Here, they are transported with RFQs and the RFQ switchyard. In the trap system, they are cooled and bunched and then injected into the analyzer were time of flight separation is performed. Afterward, they can be ejected onto the MCP detector for mass measurements or mass-selectively retrapped in the trap system. From there, they can be transported in a further trapping region and ejected into the TITAN beamlines for further experiments.

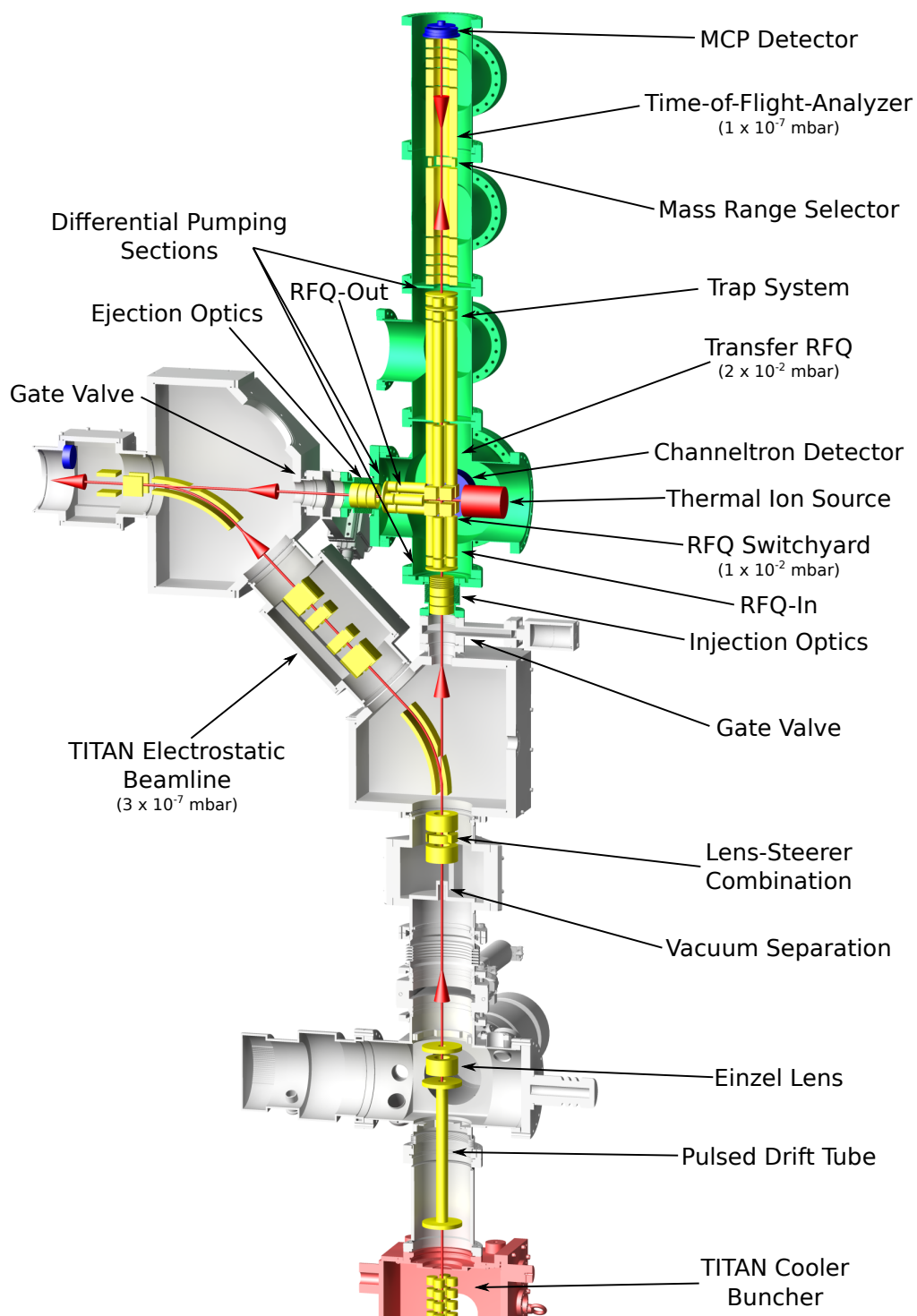Figure 3.8 shows the instrument structure with relation to the partially shown

Figure 3.8.: Schematic layout of the MR-TOF-MS at TITAN. Shown is also the beamline between the TITAN cooler buncher including and the entrance of the electrostatic switchyard leading to EBIT and the Penning traps.

TITAN beamline. In the beamline, the former steerer is replaced by a lens-steerer combination. Diagnostic elements are added at the same time. Two gate valves allow installation, repair work and optimization of the TITAN MR-TOF-MS without influencing the operation of TITAN. Additionally, mounting and supply structures (electrical, vacuum, gas) have to be added on the platform.

The injection and ejection optics consist each of a lens and a steerer to compensate for misalignment and allow high efficiency capture of the ions. In the RFQ switchyard, ions can be transported in selected directions. A channeltron detector allows to optimize the capture process while a thermal ion source produces ions for optimization tasks while the instrument is not able to receive ions from the TITAN cooler buncher, for example when the instrument is shut off via the gate valves or other parts of TITAN are in independent operation.

The transfer RFQ transports ions to the trap system, from which they are injected into the time-of-flight analyzer. A set of steerer electrodes in front of the analyzer and the mass range selector allow to compensate for misalignment, the mass range selector additionally serves to remove ions outside the unambiguous mass window. An MCP detector is used in mass spectrometry modes.

After separation, the ions are mass-selectively retrapped in the trap system and transported downwards to the switchyard and into the accumulation trap. Here, several shots from cooler and buncher can be accumulated after separation and collectively ejected to the further TITAN systems. Also, a transport back into the analyzer for a second stage of separation is possible.

Separate buffer gas supplies are used for the switchyard cross and the trap system in order to be able to optimize for different operation requirements.

Not shown in the figure is the support frame that allows to mount and align the instrument on the TITAN platform. It also houses most of the electronics to operate the instrument in order to reduce cable lengths and required recabling for moving the instrument. Overall size is $0.8\,\mathrm{m} \cdot 1.0\,\mathrm{m} \cdot 1.5\,\mathrm{m}$.

Figure 3.9 shows the available operation modes of the MR-TOF-MS in a condensed way. For diagnostic purposes, the ions from the RFQ cooler buncher can be transported to the channeltron detector or ejected onto the TITAN platform. The ions from the internal ion source can be routed identically to the ions from the RFQ cooler buncher. As a low resolution mass spectrometer using no or just a few reflections in the analyzer, the TITAN MR-TOF-MS can be used for diagnosis of the RFQ cooler buncher as well as other parts of the ISAC setup. Performing high resolution mass spectrometry allows mass measurement of very short lived nuclei. By retrapping ions previously temporally separated in the analyzer, spatial separation of ions dependent on their mass-to-charge-ratio is possible. For diagnosis, the separated ions can be ejected to the MCP detector. By transporting them to the ejection trap, they are available to the rest of the TITAN setup. Several shots from the RFQ cooler buncher can be accumulated
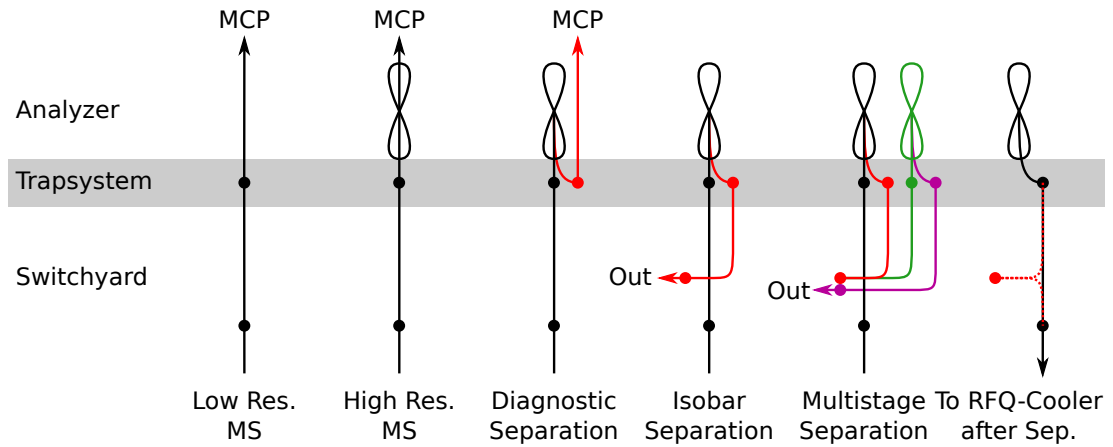
Figure 3.9.: Possible operation modes of the TITAN MR-TOF-MS. Dots represent places where ions are trapped.

here, allowing for slower measurement cycles in the Penning traps while keeping space charge effects low in the analyzer. For very high contamination ratios, performing multiple accumulated separation cycles and afterwards a second separation of the accumulated ions is possible too. Additional to the transport on the TITAN platform, transport back into the RFQ cooler buncher is possible too in order to supply isobarically clean beams to laser spectroscopy.

4. Design and Setup of the TITAN MR-TOF-MS

An ion-optical overview of the instrument is shown in Figure 4.1. Shown are as well the vacuum separations and the mixing PCBs (described in subsection 4.5.3). In the following, the ion optical design of the instrument will be detailed.

After being designed in Autodesk Inventor, the ion-optical parts and their support were produced by Häuser Metall- und Vorrichtungsbau (Biebertal, Germany) and Weber CNC Zerspanung (Homberg Ohm, Germany). Required minor modifications and some additional parts were made in the physics department workshop. Custom vacuum vessels, flanges and bellows were manufactured by Vacom (Jena, Germany) and COMVAT (Haag, Swiss). The support frame including alignment devices was designed and produced at TRIUMF.

4.1. Vacuum Setup

4.1.1. Encapsulated RFQs

The different sections of the MR-TOF-MS impose different requirements for the vacuum. While the pressure in the analyzer has to be as low as possible in order to reduce collisional losses, the same is true for the TITAN beamlines. Oppositely, the RFQs need buffer gas, usually helium, at a controlled pressure for operation. Overall the cleanliness of the helium is of importance. In the RFQs, charge exchange reactions occur at a much higher rate with gases of lower ionization potentials than helium.

This leads to the need of differential pumping sections. Since the factor of pressure reduction with typical pumps and typical aperture sizes that still permit efficient ion transport is limited to about two orders of magnitude, the need for multiple stages arises. There are two general options shown in Figure 4.3: Either to have separate outer vessels including pumps for each stage or to encapsulate the RFQ, generating a first differential pumping stage from the inside of the encapsulation to the pumped vessel and a second stage from the vessel to the next pumped vessel.

Advantage of separate vessels is the ability to evacuate the RFQ with high con-
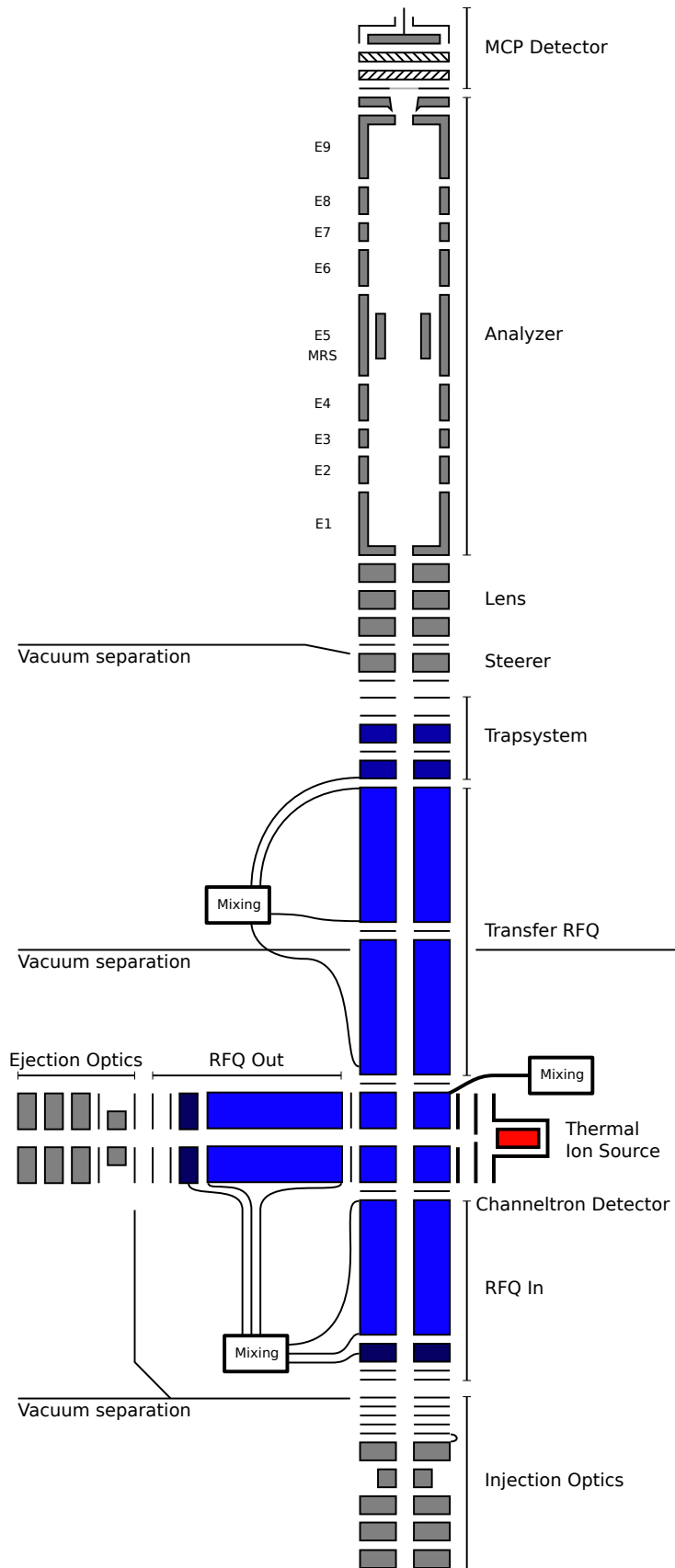
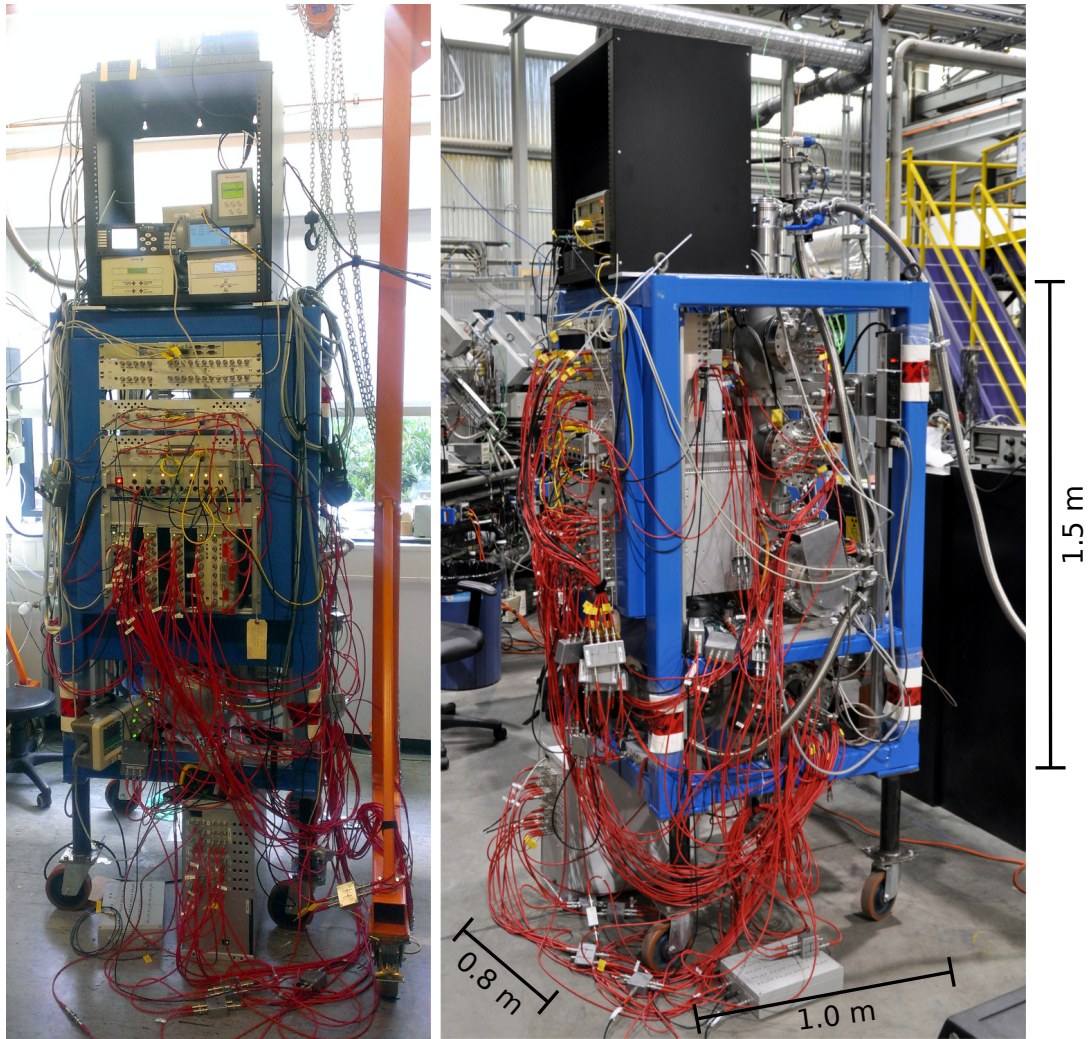Figure 4.1.: Ion-optical overview of the instrument and its subgroups.

Figure 4.2.: The TITAN MR-TOF-MS setup in the laboratory in Germany and in the ISAC hall at TRIUMF, Canada. The size of the setup is indicated. Coaster extensions will be removed for installation on the TITAN platform.

ductivity to the pumps, resulting in low residual gas pressures. Disadvantage are cost for pumps and space requirements. Conversely, encapsulated RFQ systems are typically smaller and need a lower number of pumps. Since the inside of the encapsulations are just connected to the pumps via narrow apertures, the residual gas pressure stays rather high, resulting in contaminants. This can be circumvented by implementing vent valves in the encapsulation that can be opened when the system is not in operation to allow for faster pumping.

Additionally, measuring the pressure is harder in encapsulated RFQs. They require either large conductance tubing to a vacuum gauge on the outer vessel or in-vacuum gauges. For the TITAN MR-TOF-MS, the second approach was chosen. A mini ion gauge and a micro Pirani gauge are mounted on the encapsulation. This was combined with the vent valve and the gas inlet to form buffergas
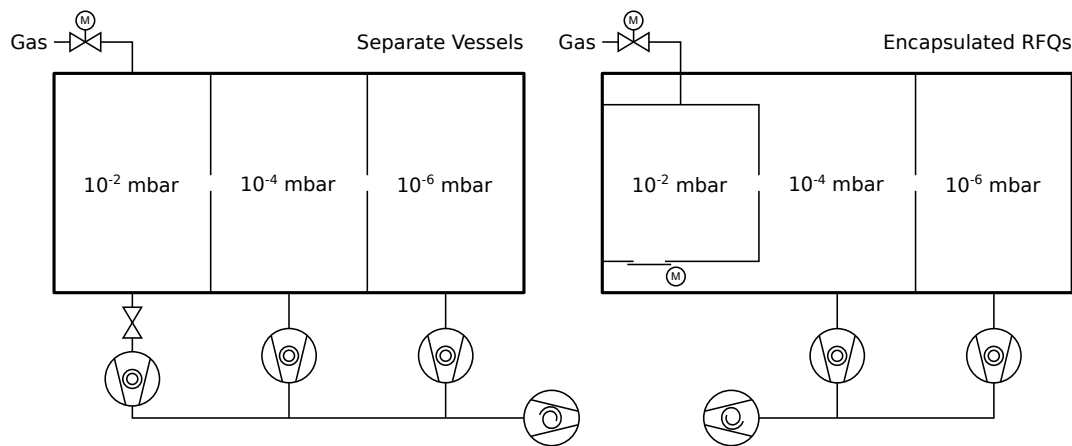
Figure 4.3.: Schematic of differential pumping for RFQs in separate vessels or by use of encapsulated RFQs.

control blocks of which two are used in the instrument.

4.1.2. Vacuum System Design

Figure 4.4 shows the vacuum setup of the TITAN MR-TOF-MS. The vacuum vessel consists of a custom 6 way cross with two times each CF 160, CF 200 and CF 250, a 5 way CF 160 cross and two 4 way CF 160 crosses. Connected are three turbomolecular pumps which are backed by a scroll pump. Pumping speed is limiting the final pressure under gas load so a multi-stage backing setup is not needed. The flanges through which ions are transported into and out of the instrument are equipped with membrane bellows to allow for alignment and tolerances. The remaining flanges are closed with a set of CF 250 and CF 160 flanges with several CF 40 and CF 16 connections to allow for gauges and feedthroughs. Unused connections are blanked off. Currently, a mixture of copper and VITON gaskets is used. For commissioning, two additional chambers were connected to the switchyard cross containing an additional source and a particle detector. They were only pumped through the apertures of the system, resulting in rather large pressures in these chambers.

The following electrical feedthroughs were used: Triple SHV double ended on CF 40, 7 pin high voltage on CF 16, 19 pin low voltage on CF 40 and floating shield SMA double ended. Two gas 1/8 inch feedthroughs introduce buffer gas into the encapsulated RFQs and are used for venting as well. Two Pfeiffer EVR 116 regulation valves allow to set the pressure inside the encapsulated RFQs. Additional ball valves are included to safely shut off the gas feed.

(U)HV pressure measurement is performed with Agilent UHV-24 ion gauges on CF 40 flanges, roughing pressure and backing pressure is measured with a Pirani gauge in the backing line. For leak checking, it is possible to include a leak checker
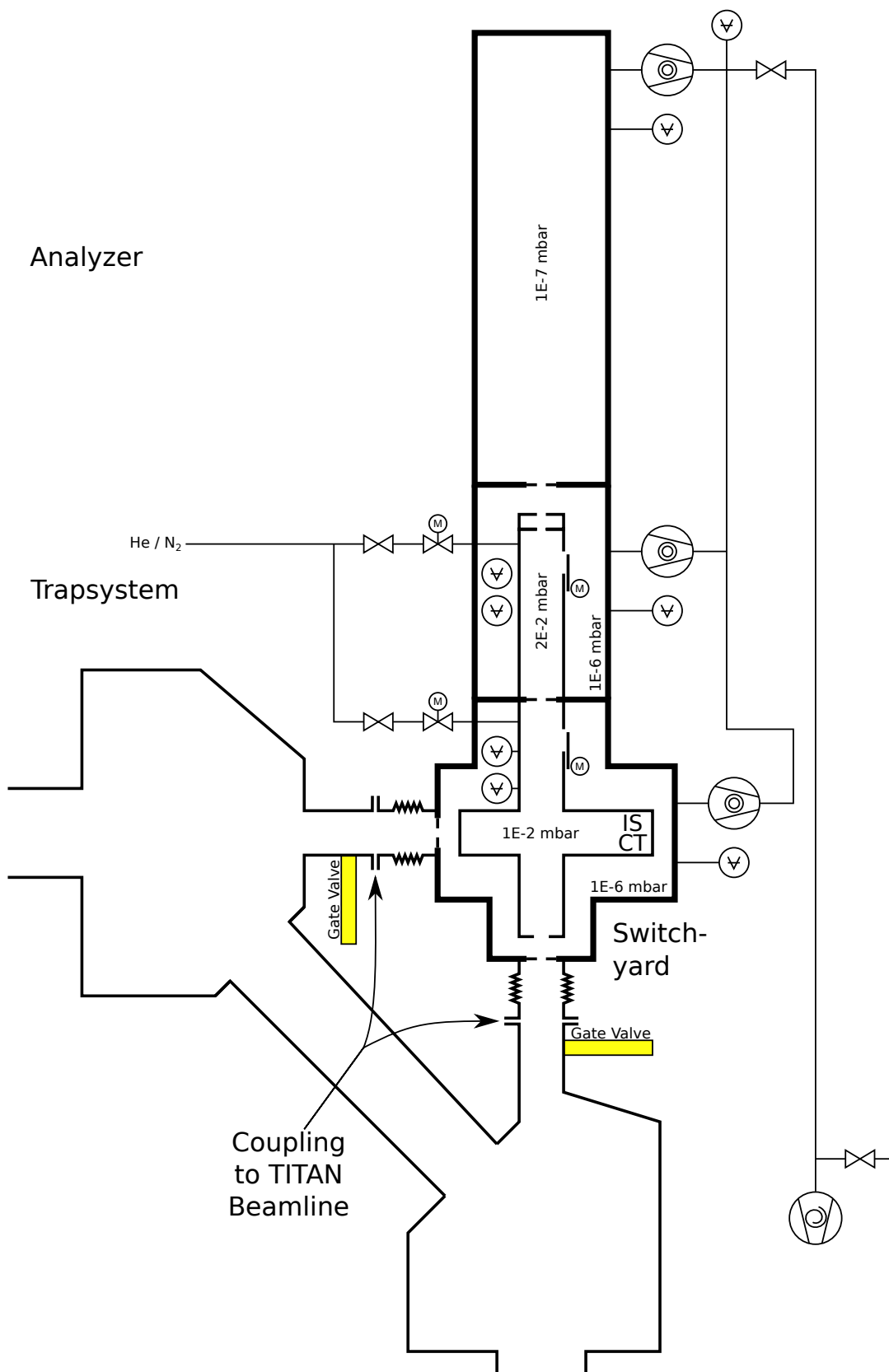
Analyzer

1E-7 mbar

He / N₂

Trapsystem

2E-2 mbar

1E-6 mbar

1E-2 mbar

IS
CT

1E-6 mbar

Switch-
yard

Gate Valve

Gate Valve

Coupling
to TITAN
Beamline

Figure 4.4.: Schematic of the vacuum setup.

in the backing line.

The system is intended to be serviceable without interuption of TITAN operation. Two gate valves block the injection and ejection beamlines. In this way, both optimization as well as at-air work is possible without interfering with the rest of TITAN.

A maximum pressure increase of $3 \cdot 10^{-7}$ mbar in the bender boxes was defined in operation. Pressures without the instrument are $3 - 5 \cdot 10^{-7}$ mbar, resulting with the installed pumping speed of $1200\,\mathrm{l/s}$ in a gas load of $3 - 5 \cdot 10^{-4}$ mbar l/s and a permissible additional gas load of about the same value. The pressure in the RFQs has to be about $10^{-3} - 10^{-2}$ mbar for operation. Minimum diameters of apertures is limited by achievable focusing, distribution in traps and achievable alignment. For the pumping barrier of the switchyard cross to beamline, a single aperture with a 2 mm diameter for the injection optics and a double aperture of 2 mm result in a total conductance of $0.92\,\mathrm{l/s}$, assuming free molecular flow. This limits the pressure in the switchyard cross to $3 \cdot 10^{-4}$ mbar).

For the analyzer, a low pressure is important to reduce collisional losses during the separation. The lower the conductance into the analyzer and out of the trap system and the higher the pumping speed on both crosses, the lower the pressure. There are no limits in this case aside from defining a maximum loss ratio and consequentially the pumping speeds.

4.2. Switchyard Chamber

The switchyard chamber is a custom designed vacuum cross with two CF 160, two CF 200 and two CF 250 flanges, each on opposing ends. The two CF 250 serve as access and main feedthrough flanges including space for extension. The CF 160 hold the flange containing mounting points for the injection optics and the alignment groove for the main ion optics of the switchyard cross, shown in Figure 4.5, while the top connects to the trap system. The CF 200 flanges connect to the turbo pump and to the exit flange on which the ejection optics are mounted as well as alignment devices for the RFQ out.

4.2.1. Injection Into and Ejection From The System

The capture optics focus and steer the beam from the RFQ cooler buncher to a set of three apertures, the first being part of the injections optics, the other two are mounted on the RFQ-in. A set of apertures with voltage divider produce a linear retarding field to slow down the ions with minimal focus size.

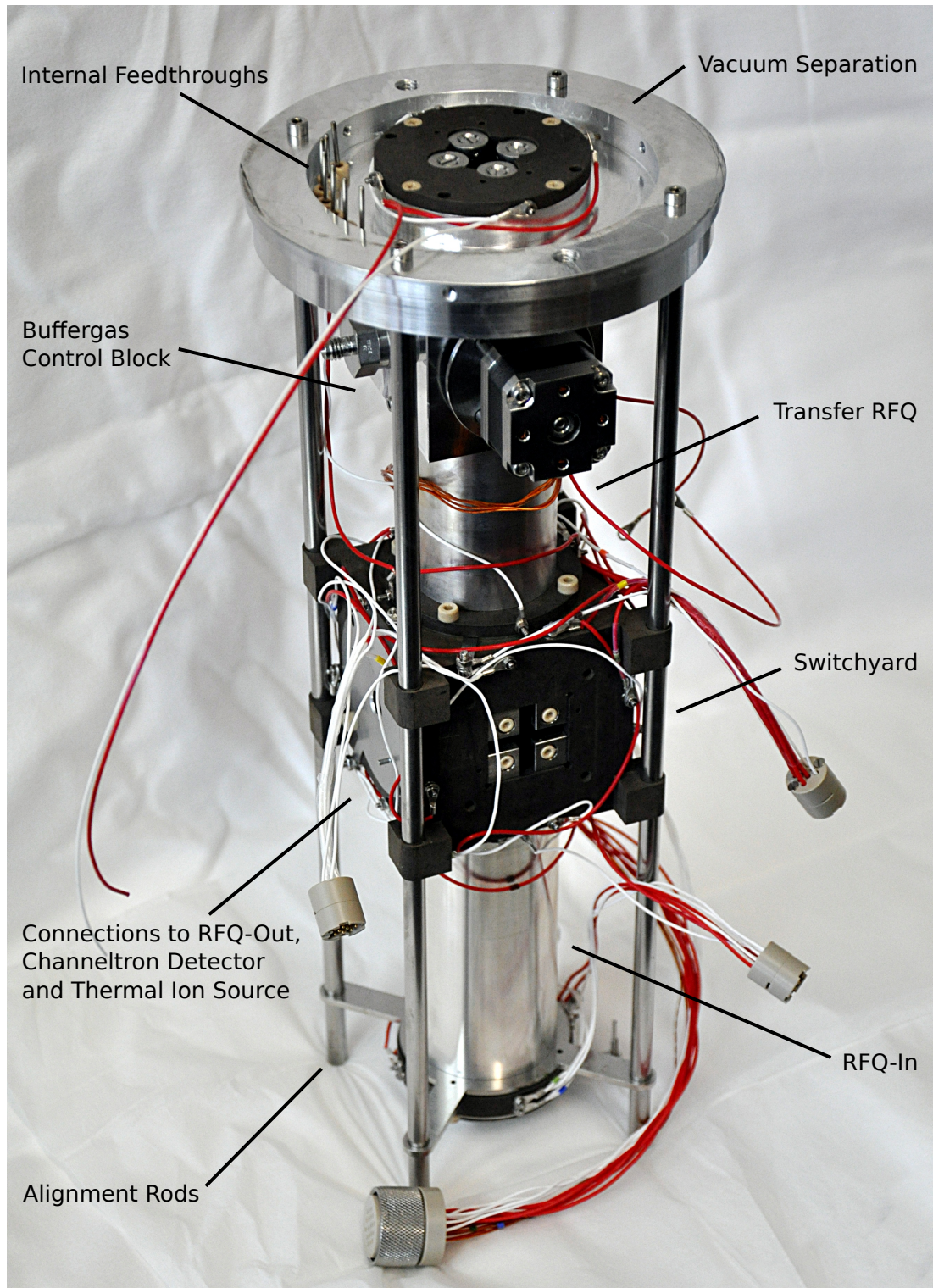Figure 4.6 shows the simulations performed with the program SIMION. They re-

Figure 4.5.: Assembly of part of the ion optical elements for the switchyard Chamber with RFQ-in, switchyard, lower half of the transfer RFQ including buffergas control block and connections to RFQ-out, channeltron detector and the thermal ion source. Alignment rods, the inset separating the vacuum volumes, internal connectors and feedthroughs can be seen as well.
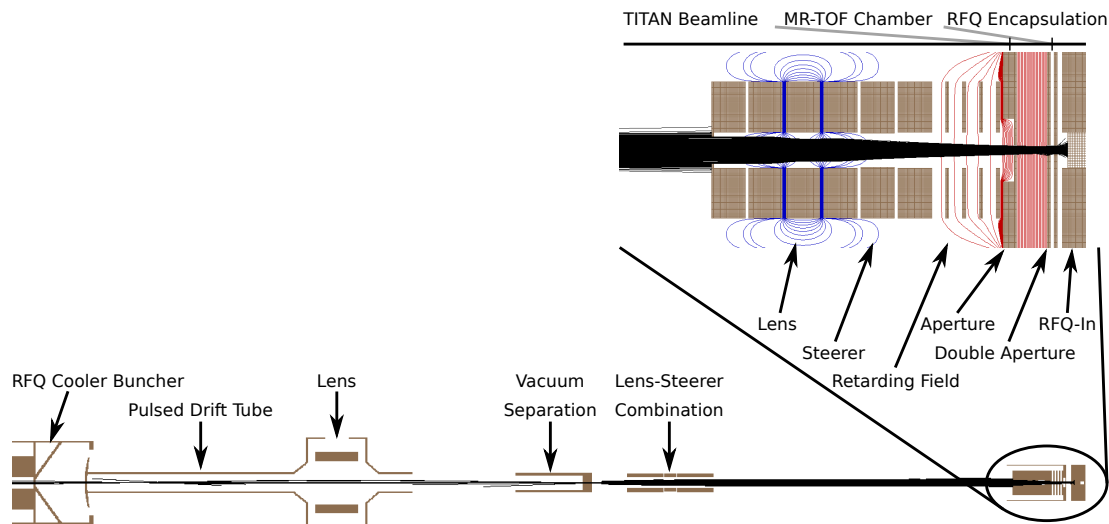
Figure 4.6.: Simion simulation of the injection optics, showing the transport of ions from the TITAN RFQ Cooler Buncher to the RFQ-In of the MR-TOF-MS.

vealed the need for an additional lens-steerer combination in place of the currently installed steerer in the TITAN beamline in order to achieve high transmission efficiencies.

The double aperture structure of the RFQ-In allows for additional focusing through the apertures. The injected ions are then stored by closing both entrance aperture and the aperture leading into the switchyard, allowed to cool and then transported further into the system. An additional RFQ segment was added to allow backwards ejection in case of future plans to transport isobarically clean ions to the laser spectroscopy setup.

The setup of the RFQ-Out is similar to the injection setup, an RFQ with additional segment, two apertures. Due to controlled start conditions, acceleration of the ions is performed with just one setup. Also a smaller steerer is employed containing a double aperture. The lens is set up identically to the injection optics. Both allow attachment of sources or detectors as well.

RFQ segments without axial field were made from stainless steel while the RFQs with axial field were made from carbon filled polyphenylene sulfide (PPS). RFQ diameters are 13 mm with a field radius of 5 mm. The rod diameter is chosen relatively large in order to reduce field penetration. RFQ-In is about 140 mm in length, RFQ-Out 90 mm.

In order to test injection into the MR-TOF-MS during commissioning, a second thermal ion source was added attached to the injection optics. Similarly, a high pressure tolerant secondary electron multiplier (MagneTOF [ETP electron multipliers, 2006]) was positioned in front of the ejection optics to test ejection.
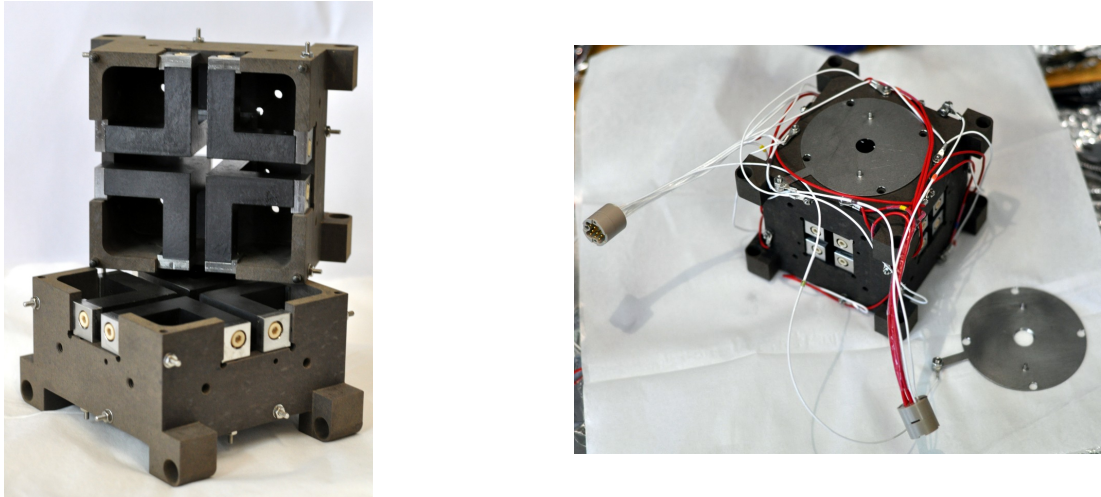
Figure 4.7.: Photographs of the switchyard in open state and assembled and cabled with apertures attached.

4.2.2. Switchyard

The principles of the switchyard were already discussed in subsection 3.3.1. The practical implementation can be seen in Figure 4.7. The electrodes are as well made from carbon filled PPS and have a size of 32 mm each. They are held in the PPS shell (A cube with 80 mm width) with metallic contact blocks that are attached to electrodes and tightened against the shell. In order to achieve gas separation for adaption to the encapsulated RFQ scheme and to support and align the electrodes, a switchyard shell was designed in which the electrodes are mounted and aligned by means of the contact blocks. Alignment holes and threads allow to connect adjacent system parts. [Greiner, 2013, Plaß et al., 2015]

4.2.3. Internal Source and Channeltron Detector

Two diagnostic devices are included in the switchyard cross, the internal thermal ion source and a channeltron detector. Both are shown in Figure 4.8.

The internal thermal ion source allows independent optimization from other platform operations. It consists of a resistively heated porous tungsten disc, in which a metal salt is deposited in an aluminosolicate matrix [HeatWave Labs, 2002]. The ions emitted from the source are accelerated through an aperture with a second aperture added for field optimization. The same type of source was also installed in front of the injection optics for the offline tests.

To allow optimization and quantification of the injected beam without operating the TOF analyzer, a channeltron detector was included. In it, the beam is post-accelerated and can be steered onto a conversion dynode to reduce the position dependency of the channeltron's signal [Reiter, 2011]. By choosing a channeltron
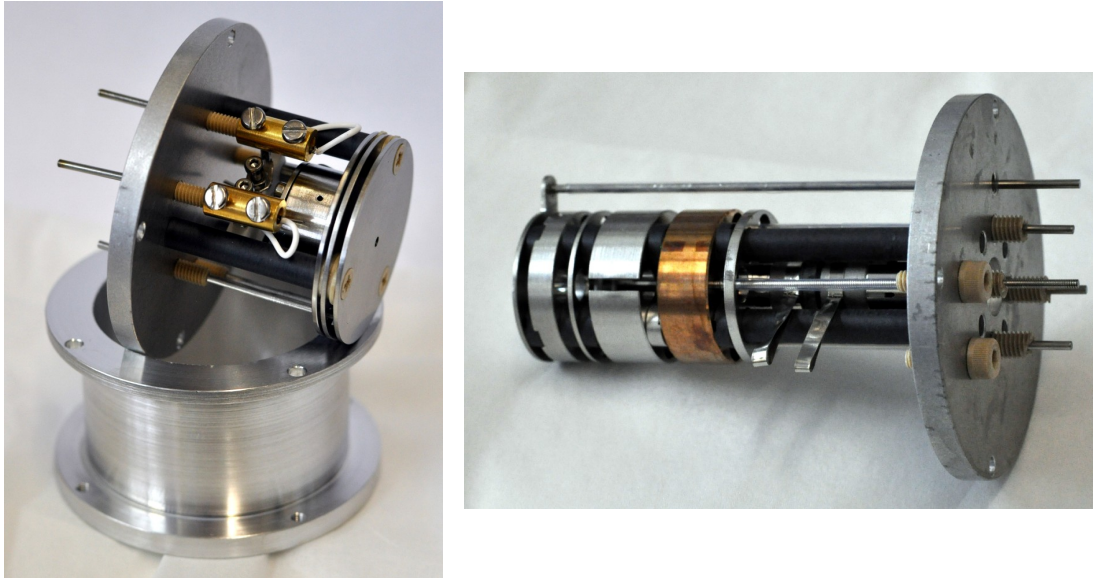
Figure 4.8.: Internal ion source and channeltron detector setups.

instead of MCPs, operation is possible inside the encapsulated RFQ at up to 10^{-3} mbar without differential pumping.

4.2.4. Transfer RFQ

The transfer RFQ connects the switchyard to the trap system via an aperture to allow different pressures in the two regions. Due to space limitations, it is also the location of the buffer gas control blocks for the switchyard cross and the trap system cross. Behind the aperture used for pressure separation, an RFQ with variable length allows to handle position differences due to construction of the vacuum vessel from several crosses. The total length of the transfer RFQ is about 450 mm.

4.3. Trap System

Ions are transported to a pre-trap RFQ segment behind which the trap itself is positioned. The injection trap consists of a RFQ segment and two apertures. In order to achieve a small size in axial direction of 7 mm, the RFQ has to be designed smaller in order to achieve sufficient storing fields in the trap. The segment diameter is therefore 8 mm with a field radius of 5.5 mm. A shielding electrode reduces field penetration from outside. The trap is mounted directly on the steerer in the flange separating trap system and analyzer. The analyzer is mounted to the steerer as well, allowing precise positioning.
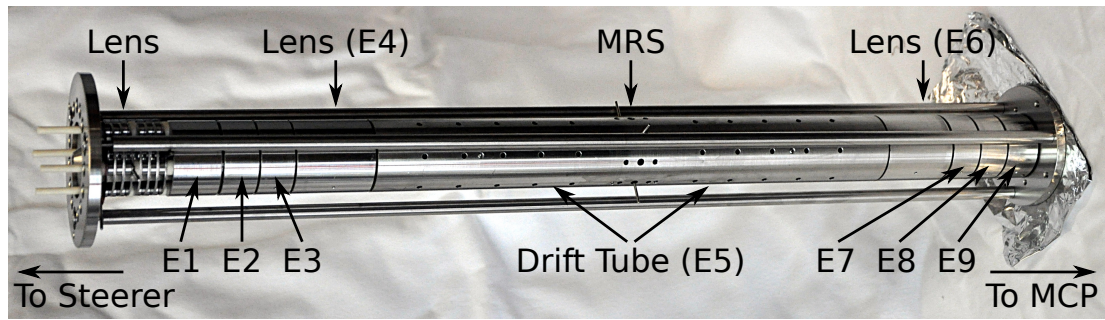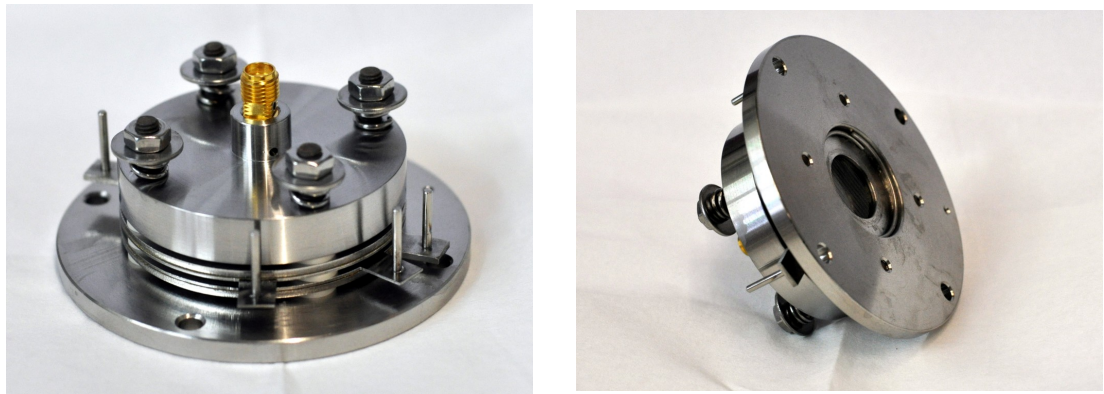
Figure 4.9.: Photograph of the analyzer.

Figure 4.10.: Photograph of the MCP detector.

4.4. Analyzer and MCP Detector

The analyzer's ion optical properties have already been discussed in subsection 3.3.2. The electrodes are made from INVAR steel in order to reduce thermal expansion effects. Distancing and alignment are performed by precision ground ceramic balls between the turned electrodes. Three rods between the steerer in front of the analyzer and the mounting plate for the MCP detector serve to tighten the assembly. In the central drift tube two apertures assure that ions colliding with electrodes are not reflected back in, contributing to background. The mass range selector electrodes are situated in the central drift tube as well.

Between the steerer and the analyzer, a series of electrodes form a single lens. Alignment between the steerer, the lens and the analyzer is performed by a set of four ceramic rods. The mechanical realization can be seen in Figure 4.9.

The micro-channel plate (MCP) detector is shown in Figure 4.10 and consists of an entrance grid, a chevron stack of two micro-channel plates (Photonis Long-Life Detection, 18 mm, 40:1 EDR), the detection anode and mounting and shielding hardware. An in-vacuum voltage divider generates the needed potentials for the MCPs.
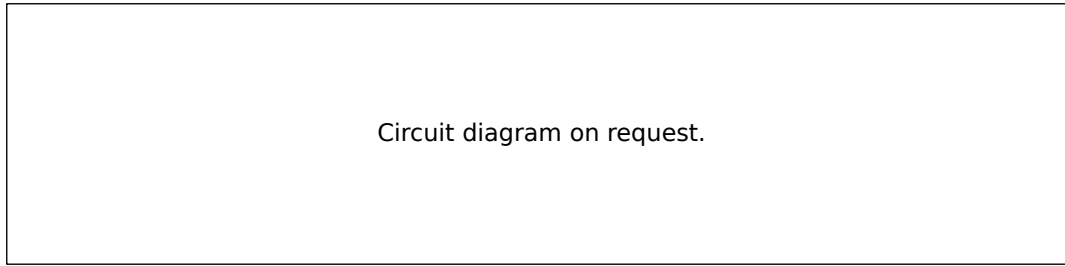
Circuit diagram on request.

Figure 4.11.: RF generation diagram. In the generator box, two sets of excitation electronics, toroidal coil, a resistive load to reduce the Q-factor and a RF analyzer are combined. Shown as well are parasitic loads of the cable, the RF-DC-mixing (here with resistors) and the electrodes, forming the final load.

4.5. Electrical Design

4.5.1. DC Potential Generation

The required DC potentials for the ion optical elements are generated using ISEG high voltage power supply modules (ISEG EHS and EBS) in a W-IE-NE-R MPOD 2H crate controlled over Ethernet. A W-IE-NE-R low voltage module supplies the RF generation (see next section) with selectable DC potentials to control the RF amplitude.

The resistive RFQs require higher currents ($\approx 20 - 100\,\text{mA}$) than the ISEG power supplies can provide. Sinking the current would be problematic as well for the ISEG HV modules. Therefore, an additional W-IE-NE-R MPOD Mini crate houses further low voltage modules. This crate can then be placed inside a Faraday cage and isolated with a transformer and fiber-optical Ethernet links in order to provide the potentials for resistive RFQs and surrounding apertures.

4.5.2. Radio Frequency Generation

The RFQs require a symmetric RF with a frequency of about 1 MHz and a peak-to-peak amplitude of a few hundred Volt. The way this RF is generated in this work is by exciting an LC circuit in the middle of a toroidal coil by switching the coil centerpoints [Konradi, 2013]. Since the capacity of the electrodes is mostly insignificant compared to the capacity of the coaxial cables used in the setup, the frequency defining parts are the coil inductance and the cable and feedthrough capacities. Advantage of the toroidal coil is the relative insensitivity to the presence of ferromagnetic materials in the surroundings which, for linear coils, can result in asymmetric systems having different amplitudes and wrong phase relations. Symmetry can be achieved by taking care that cable lengths and
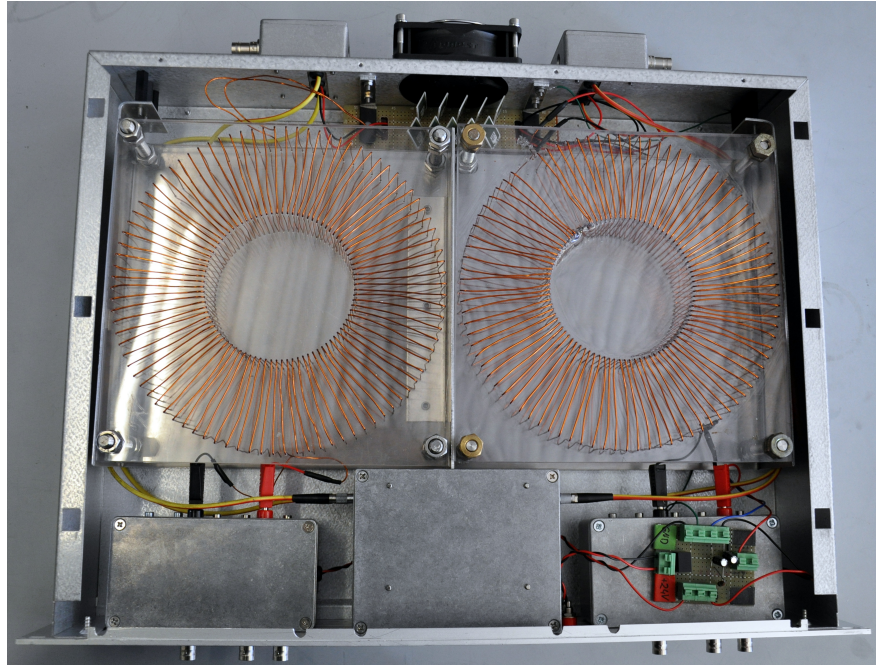
Figure 4.12.: RF generation box. Two channels side by side. Excitation electronics in the lower left and right box, a toroidal coil, Q-factor reducing resistors and connectorbox including a voltage divider for the RF analysis box in the front.

paths are similar. In vacuum, twisted wires are a good way to do this and reduce crosstalk at the same time. Additionally, there are trimming capacitors added to the RF generation boxes. The RF generation scheme can be seen in Figure 4.11, the realization of the RF generator in Figure 4.12.

In order to tune the RF, formerly oscilloscope probes were used. This has the disadvantage that adding the probes changes the capacitive loading and therefor the tuning. Additionally, oscilloscope resolution of 8 bit and amplitudes above 400 Volt, tuning the sum signal to below a volt is not possible. Therefor, a RF analysis system [Ayet, 2015] has been included into the RF generation box as well. It consists of capacitive voltage dividers, input amplifiers and amplitude, amplitude difference and phase detectors. Additionally, the buffered input signal can be measured on an oscilloscope.

While a high Q-factor of the setup allows to generate high RF amplitudes at low input powers, the narrowness of the tuning makes the system prone to mistuning and drift. In order to reduce this, a Q reduction load was included.

4.5.3. RF-DC-Mixing

Since the RFQ potentials in the TITAN MR-TOF-MS are typically at above 1 kV and several electrodes can be driven by the same RF due to identical geometry,
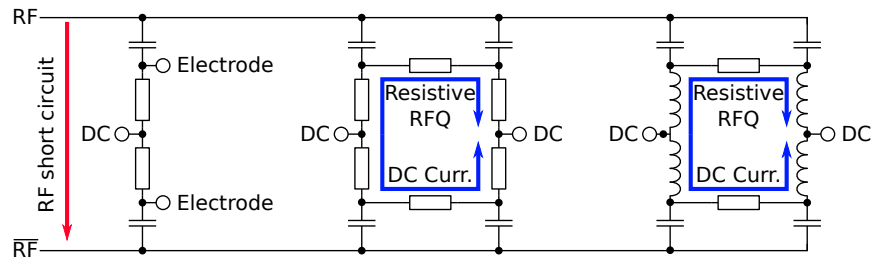
Figure 4.13.: RF DC mixing: Resistors for mixing - Resistors for resistive RFQs - Coils for resistive RFQs.

the DC component for the electrodes is mixed in separately. While it is possible to do this at air, this requires $2 \cdot N$ feedthroughs for N RFQ segments or $N/2$ resistive RFQ electrodes. By performing the mixing in vacuum, the number of require feedthroughs reduces to $N + 2$.

The basic concept of RF mixing is to use the low impedance for RF and high impedance for DC of capacitors to feed RF from a bus to the electrode and another component possessing a high impedance for RF to stop the RF from shorting out through the DC path (Figure 4.13). In the case of RFQ segments, this can be a resistor with its high impedance for both RF and DC. This becomes problematic for resistive electrodes. Here, the current that is needed to generate the potential gradient over the electrode will effect a voltage drop over the mixing resistors as well. For typical values for coupling resistors ($\approx 10\,\text{k}\Omega$) and the resistive electrodes ($\approx 1\,\text{k}\Omega$), most of the applied voltage is 'lost' over the coupling resistors, generating power dissipation and exact RFQ entrance potential problems. A solution to this problem is to employ inductors instead. Here, the DC impedance is negligible compared to the rod resistance. Disadvantage is typically the need to wind those inductors, their larger volume and surface area.

A second problem arises from the need for fast switching of potentials on electrodes. Here, the coupling capacitor has to be charged to the desired new potential through resistors or coils. This influences the dimensioning of both capacitor and DC coupling components. The capacitors must not be chosen too small due to the RF voltage drop over the mixing circuit including parasitic capacitance. Choosing small impedance for the DC coupling components as well results in low RF amplitudes.

4.5.4. Potential Switching

For the operation of the instrument, fast switching of electrode potential is required. The needed switching capabilities depend on the use case, for pulsed electrodes whose fields directly affect ions in their vicinity, fast switching ($\ll 1\,\mu\text{s}$) is needed. For pulsed electrodes where the ions are shielded by other electrodes from the changing fields, slower switching on the time scale of instrument cycles
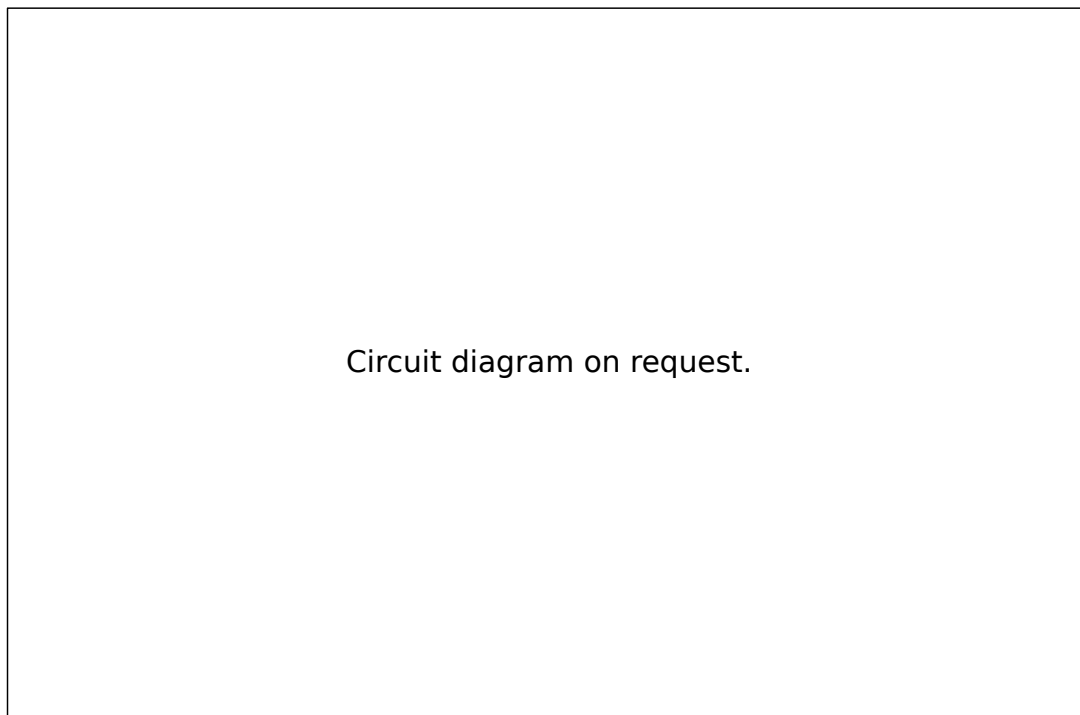
Circuit diagram on request.

Figure 4.14.: Voltage Stabilization diagram. MT voltages are filtered with RC filters before being supplied to HV pulsers and the analyzer electrodes E1-E4 and E9-E6 respectively.

is sufficient ($\ll 1\,\text{ms}$). Additionally it has to be considered that the load in the case of electrodes or RFQ segments is almost purely capacitive while, for resistive RFQs, considerable resistive loads have to be driven.

In the system, IGBT bridges are used as pulsers between two potentials. These switches are controlled over isolation devices [Ayet, 2015]. Depending on requirements, the pulsers have to be modified with pulse shaping resistors, resistive loads and capacitors to work as intended. For example, putting a pulser in series to another pulser to achieve three levels that can be switched to an electrode, the capacitor and resistor in the input of one pulser has to be removed.

4.5.5. Voltage Stabilization

The total time-of-flight in the analyzer is strongly influenced by the actual voltages supplied to the electrodes of the analyzer. Electrodes that are passed just once like the steerer and lens in front of the analyzer are less critical. While the used ISEG power supplies are already rather stable, some noise is still present from switching inside the power supply, ADC changes and as well from differing loads in the event of switching in the instrument. This would lead to peak broadening and loss of resolution.

A stabilization in form of RC filters has been included [Ayet, 2015, Lang, 2016]. They consist of 4th order RC filters with a cutoff frequency of $f_C = 1.6\,\text{Hz}$. The size of the capacitors was chosen to stay within safe limits for humans in the case of an unintended discharge. For E4, a higher voltage required a change in the design, here it is a 1st order filter with a $f_C = 5.3\,\text{Hz}$.

Included into the two boxes built for the MR-TOF-MS and shown in Figure 4.14 are the pulsers needed for the operation of the analyzer. Only the voltages for the multiple turn settings are stabilized in this fashion.

A disadvantage of the RC-structure of the system is an operation-dependent voltage drop over the filter. The output therefore has to be measured and tuned for the right settings. In the future, a measurement system can be included as well as a variable load making a stable and precise setup for various operating conditions.

4.5.6. Trigger System

In previous work [Dickel, 2010], National Instruments NI 6602 PCI cards [NI-6602, 2016] were used to generate TTL signals to control the instruments. Unfortunately, the 80 MHz clock, the limitation to 8 channels, additional jitter should one couple several cards, the inability to generate a pulse sequence with a fixed phase to a second signal and a rather large frequency drift due to temperature changes make this solution problematic. Additionally, external components were needed to derive a monitor signal and combine signals of several channels into derived signals.

A new solution should be a stand-alone operation, controlled via ethernet or serial port. 16 channels from one system are minimum, 32 channels optimal. Timing errors have to be negligible compared to the typical peak widths of some 10 ns. Ringing has to be controlled. The new device marks the change from BNC to Lemo connectors for the group's setups as well as the change from parallel termination to serial termination.

Signals needed for instrument control range from RF generation at about 2 MHz and the control of ion gates or traps for mass selective interaction with timing resolution better than the peak widths. On the other hand, instrument cycles down to 10 Hz or even below 1 Hz are needed. This results in a counter system capable of counter frequencies better than 200 MHz and counter widths of at least $2 \cdot 10^8 \approx 27\,\text{bit}$.

The trigger system was developed on an Altera DE2 board, containing a Cyclone II EP2C35F672 FPGA. This board provides a sufficient number of input and output devices (Switches, push buttons and LEDs) to test the parallel bus and counter operation. The device used in production is an Altera DE0-Nano with a

Power, Clock, Interface and Distribution Board

Power Conditioning Logic

Input Connector

Power Conditioning
FPGA

Serial Port

Oven Controlled
Oscillator and
Power Conditioning

FPGA Connectors

Monitor Connector
to Logic Analyzer

Output Connectors 0-3

Output Board

2 Outputs per Channel, Independently Driven

Power Conditioning

Level Conversion, Output buffer
and 50 Ohm Termination

Terasic DE0-Nano Development Board

Input and LED Board

LEDs for Status
and Communication

Input Connectors

Ribbon Cable
Connection for
Signal and Power
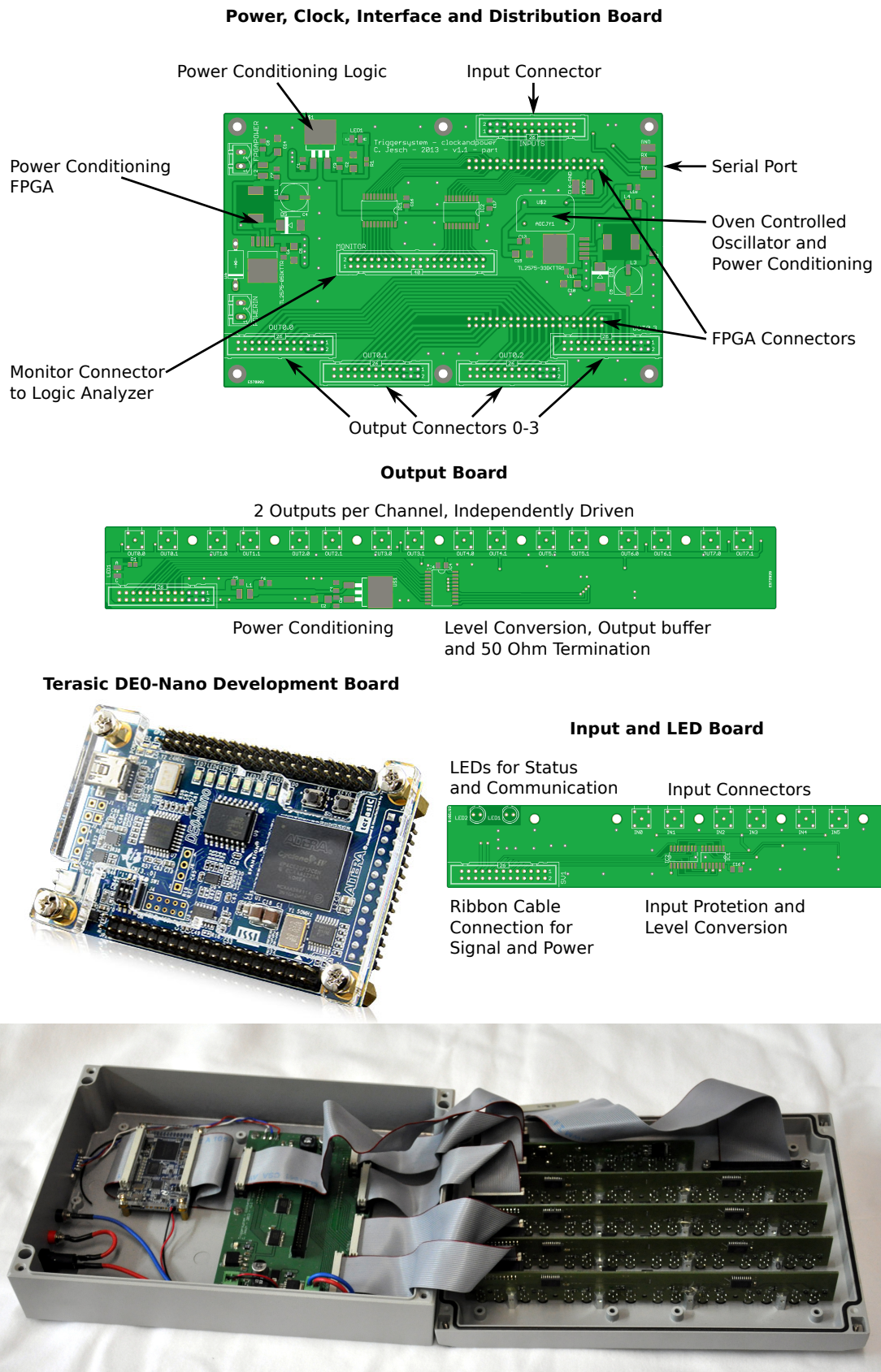
Input Protetion and
Level Conversion

Figure 4.15.: Electrical Blocks of the Triggersystem.

Cyclone IV EP4CE22F17C6N FPGA. Since the frequencies produced are not very high and timing between different lines is not too critical, transport with ribbon cables is possible and the production of a custom FPGA board with its BGA soldering, multilayer setup and power and EMC considerations is not needed.

The hardware is shown in Figure 4.15. It consists of the of-the-shelf FPGA board, the power, clock and distribution board, four output boards and an input and LED board which were designed and built. The power, clock and distribution board provides power conditioning for the FPGA board, a TTL monitor output that can be connected to a logic analyzer included in some of the oscilloscopes used in the setups, serial interface converter, an 10 MHz oven controlled oscillator with a stability of down to 50 ppb and connectors for power and signal to the in- and output boards. The FPGA board is connected with ribbon cables. On the output board, separate power filtering and conditioning is implemented in order to minimize crosstalk. The signal is first converted from LVTTL to TTL after which output buffers and the serial 50 ohms termination feed the Lemo connectors. On the input board, Schmitt trigger inputs provide clearly defined signals for TTL to LVTTL conversion. Both input and output boards have circuit protection included.

On the FPGA side, the trigger system was written in VHDL without the use of IP cores. Clock is separated between a 50 MHz clock for instrument control and currently a 250 MHz clock derived from the 10 MHz OCXO via PLL block. Main connecting element is a parallel bus with 8 bit data (bidirectional) and 10 bit address. Handshake signals are read/write selection, strobe and acknowledge. An RS232 communication block consisting of UART, character decoding and state machine to parse commands and send replies controls the bus master which in turn controls the states of the bus. The 10 bit address space is divided into 4 bit = 16 locations for each blocks, allowing to address 64 blocks.

A 64 channel wide signal bus collects the output signals of the devices as well as the 6 inputs and constant high and low signals. The devices connected to the bus are 32 delay blocks, 16 logic boxes and multiplexers for the 32 outputs and the signal monitor (Figure 4.16).

The delay blocks (Ctr from counter) consist of the control logic, a bus slave state machine that reads and writes the configuration memory of the block. The timing logic is driven by the faster PLL clock. From the signal bus, a signal is selected with a multiplexer and fed into a edge detector and afterwards into the counter itself. Figure 4.17 shows both the block setup and the flowchart of the counter. The counter is 32 bit wide. Aside from setting the off-time after the trigger and the subsequent on time, the counter can be configured to be disabled, to react to falling or rising edges, to run just once after a trigger event or to keep running as long as the input condition stays valid and to invert the output signal as can be seen in Figure 4.18.

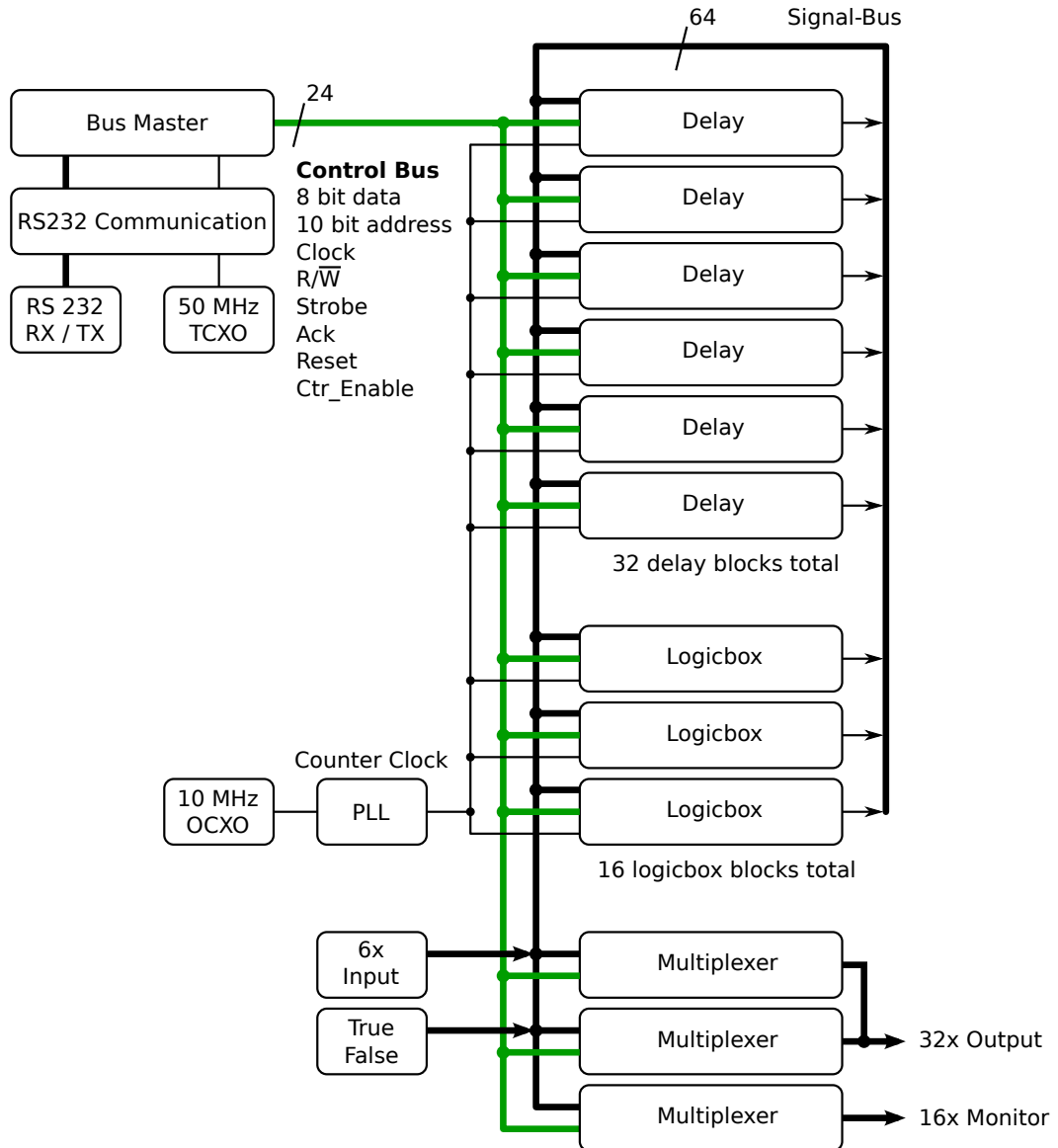In some cases, boolean logic combinations of signals are desirable in order to

Figure 4.16.: Block scheme of the FPGA setup of the trigger system.

simplify timing schemes. The former solution were dedicated hardware boxes containing logic ICs. Included in the trigger system are 16 so called logicboxes (LB). Each box again consists of bus slave, configuration memory and the timing logic. Here, four signals are selected via multiplexer. The desired logic operation, available are AND, OR and XOR, is performed on the four signals. The inputs and output can be selectively inverted with XOR gates.

The values transferred over serial interface are in the form of hexadecimal numbers encoded in ASCII in order to allow communication via terminal sessions and to keep control characters available. A Labview program was written to allow control including saving states in a XML format. The simple command structure allows integration into different control setups as well.
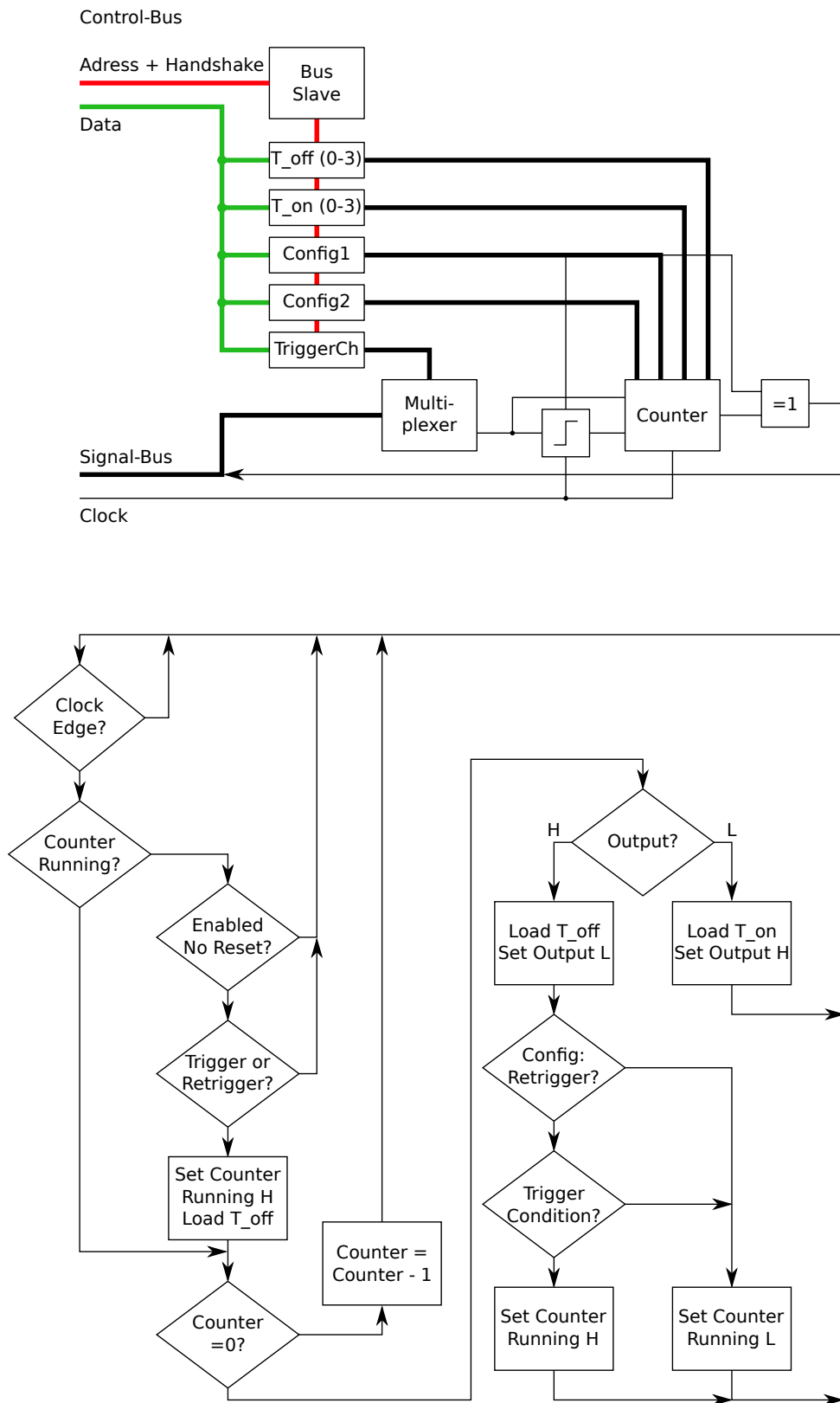
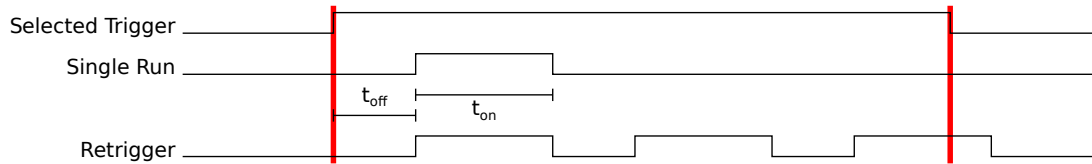Figure 4.17.: Setup and of the delay blocks of the trigger system.

Figure 4.18.: Function of single trigger and retrigger channels.

Options for future enhancement are inclusion of a version number handshake, further increase of frequency capability. For RF generation, especially in the case of high quality resonance circuits or for mass selective square wave RF systems, tuning to a kHz or below is required. The current 4 ns steps result for example in 8 kHz steps at a generated frequency around 1 MHz. Since no longer timing intervals are required here, specialized channels for RF generation with smaller counter widths could allow for higher frequencies. Another option that also high resolved channels could profit from are transceiver devices, usually employed for high speed serial buses.

Further enhancements are possible in terms of the sequence control. For example, in the case of isobar separation devices, performing a drift check every n-th shot can be beneficial. For this, additional counters that count the cycles of the instrument could be added. Another interesting option are flip flops, devices that can be set by one pulse and cleared by another, allowing clearer and more intuitive trigger schemes.

5. Results with the TITAN MR-TOF-MS

5.1. Ions on Detectors

After assembly, the preparations for the first tests with ions were done. For the analyzer, DC sparking tests had to be conducted due to the small gaps and high potential differences. For protection, all neighboring electrodes were grounded and the electrode under test connected directly to a power supply. All electrodes reached their test potential, in the case of E4 and E6 some fluctuation in current were noticeable, this suggests reworking the electrode edges at a fitting time might be worthwhile.

All three RF generation systems were tuned for symmetric RF. The resonances were found to be at the frequencies of 0.982 MHz for the RFQs, 1.360 MHz for the switchyard and 1.510 MHz for the trap segment of the trap system. Amplitudes have been set to 280 Vpp, this results in RFQ parameters as shown in Table 5.1.

DC gradients across the RFQs were 2 V for RFQ-In and RFQ-Out and 5 V for the transfer RFQ. Since no pulsed operation for the injection into the MR-TOF-MS was attempted yet, the switchyard was operated without DC gradient.

Operation at high potential was not possible due to the Faraday cage for the DC power supplies not being ready yet, the following preliminary tests were conducted at a trap potential of 285 V as opposed to the planned 1,300 V. The available power supplies limited the kinetic energy of the ions to 650 eV, half the design value of 1,300 eV. Increasing the kinetic energy will reduce the relative energy spread of the ions, reducing their aberrations.

The ion current of the external ion source was tested on the internal aperture. Afterward, detection of the ions on the MCP detector was tested, without and

Area	q	V_{pseud} (Surface)	V_{pseud} (1 mm)
RFQs	0.43	15 V	0.6 V
Trap Segment	0.63	22 V	1.8 V
Switchyard	0.33	11.6 V	0.7 V

Table 5.1.: Calculated Mathieu parameter q and pseudopotential depths at electrode surface and 1 mm from optical axis for the RFQs used throughout the experiments.

	E1 + E9	E2 + E8	E3 + E7	E4 + E6
MT	490 V	240 V	−150 V	−2010 V
ST	400 V	240 V	50 V	−1380 V
Open	−150 V	−370 V		

Table 5.2.: Typical voltages for the analyzer at 650 eV drift energy and a potential of −365 V of the drift tube of the analyzer (E5).
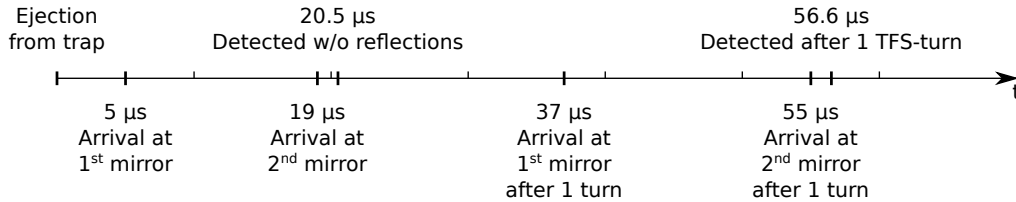

Figure 5.1.: Measured times for certain analyzer positions and 650 eV drift energy.

with RF on the RFQs. With RF applied to the RFQs, the count rate increased strongly, showing the presence of RF and at least no crude mistakes in RFQ cabling.

Buffer gas was added and after some DC testing, storage and bunching of ions in the transfer RFQ, the pre-trap and the main trap was achieved. The path to the ejection trap and pulsed ejection onto the MagneTOF detector was shown as well.

With the basic transport paths working, operation of the analyzer was attempted, first while connecting the corresponding electrodes of both analyzer halves (E1-E9, E2-E8 etc), later with separate stabilizer boxes for both halves. Typical voltages of the analyzer can be seen in Table 5.2. In order to check the timing in the analyzer, it was put into the first mode the ions are injected in (open / TFS) and ions were projected onto the MCP detector. Then, the closing time of the first mirror was scanned and the time at which ions were first shifted in their arrival time and then blocked taken as the time in which they arrive in the influence area of the mirror. A similar approach was pursued for the closing time of the second mirror. After setting the closing times in order to minimize influence on ions for the pass in the first and the reflection in the second mirror, timing for the arrival in the first mirror and passing of the second mirror is checked as can be seen in Figure 5.1 and used as a basis for the analyzer timings. Schematics of the electrical setup for the ion optics can be found in Appendix A.

5.2. Timing Scheme

The TTL control scheme was developed in a way that the least number of timings have to be adjusted to tune for different turn numbers or switch between mass
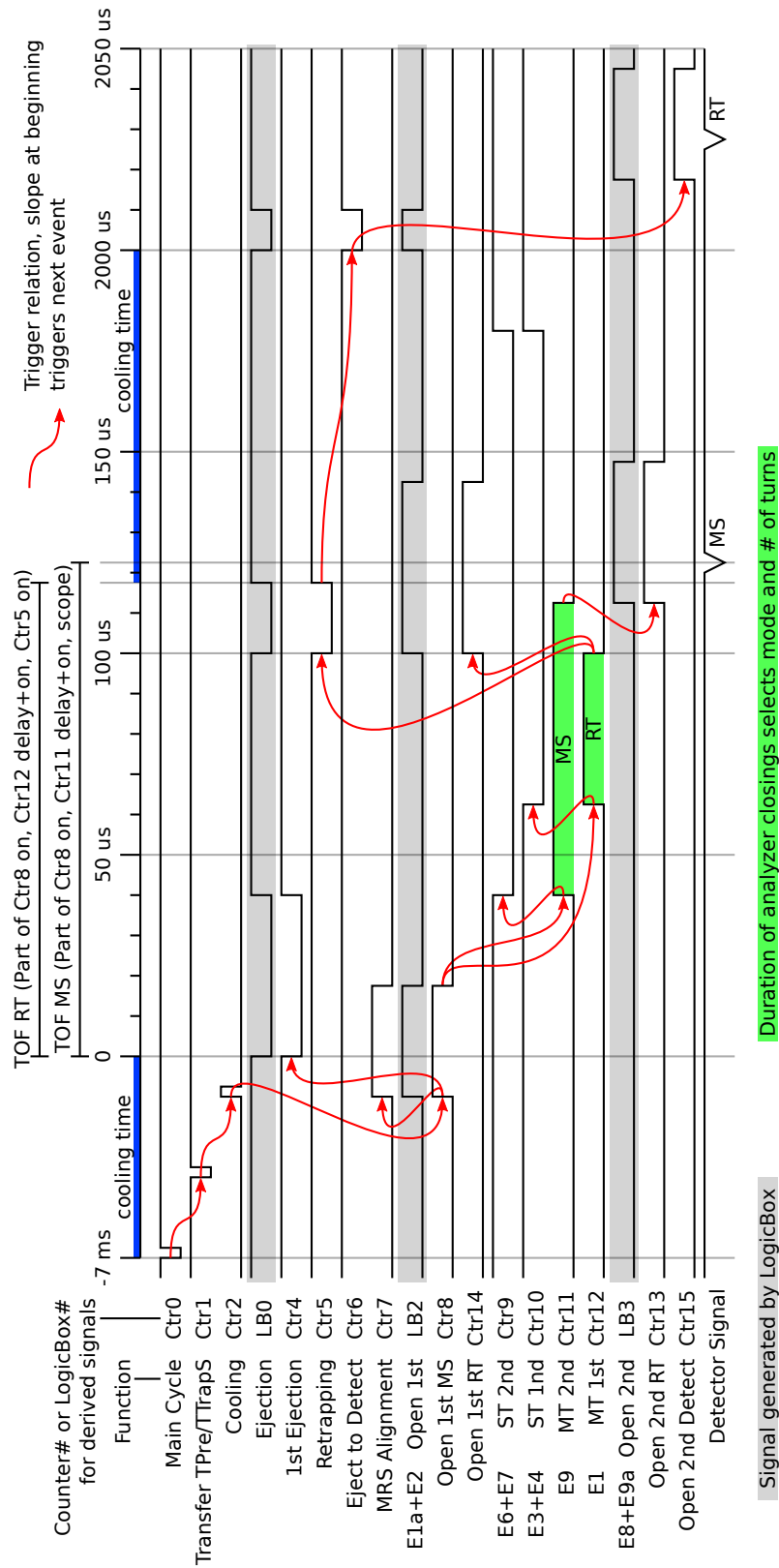
Figure 5.2.: Schematic sequence for operation of the full instrument. See text for further explanation.

spectrometry and retrapping mode. It is shown in Figure 5.2. The ions are transported into the pretrap and afterwards into the trap. In order to minimize switching effects, the analyzer state for injection into the analyzer is prepared already a bit ahead of time. At a set time after ejection, the 1st reflector is closed for the TFS mode turn. While the ions are in the non-affected half of the analyzer, first the second mirror is switched to MT mode. Once the ions make their first reflection in MT mode, the first mirror is switched.

The analyzer is held in the closed state by two timer channels (Ctr11 and Ctr12). Mass spectrometry mode is performed when second mirror is opened first in order to eject the ions onto the detector. By opening the first mirror before the second one, retrapping can be achieved. In this mode, the trap system is opened again as well to allow retrapping. Scanning the trap's closing time (Ctr5) selects the species to be trapped from the analyzer.

After the ions are trapped again, some cooling time is allotted. Then, the ions can either be transported back into the switchyard (not implemented yet) or ejected again into the analyzer. To allow precise peak area estimation, the ions are allowed to perform another TFS turn to produce a narrow peak on the detector. Afterwards, the initial state of the instrument is restored and a new cycle begins.

Three TTL signals (Open 1st, Open 2nd and the Trap Ejection signal) are generated by logic operations from several counter channels in order to achieve a flexible setup that is still easy to operate.

5.3. Mass Spectrometry

Starting with voltages from ion-optical simulations, optimization was performed including all analyzer voltages for TFS and MT, both steerers, the two lenses and the trap itself. Due to the large parameter space, no full scan of all parameters is possible.

A resolving power (FWHM) close to 50,000 as shown in Figure 5.3 was achieved with ≈ 8.2 ms time of flight, corresponding to 256 turns in the analyzer at $650\,\text{eV}$ kinetic energy. For extraction, the electrodes of the trap were pulsed $\pm 173\,\text{V}$ above and below the potential of the trap segment. This results in an extraction field strength of $37\,\text{V/mm}$. According to Equation 2.26, the turn-around time for ^{133}Cs at this extraction voltage is $12\,\text{ns}$ assuming an ion temperature of $300\,\text{K}$. At present, aberrations are therefore the limitation for the resolving power.

Simulations and experiences with the other MR-TOF-MS instruments produced in this group indicate that a significantly higher resolving power of about $100,000$ should be achievable with the present electronics. Up to $600,000$ have been achieved, however this requires specialized power supplies [Dickel et al., 2015].
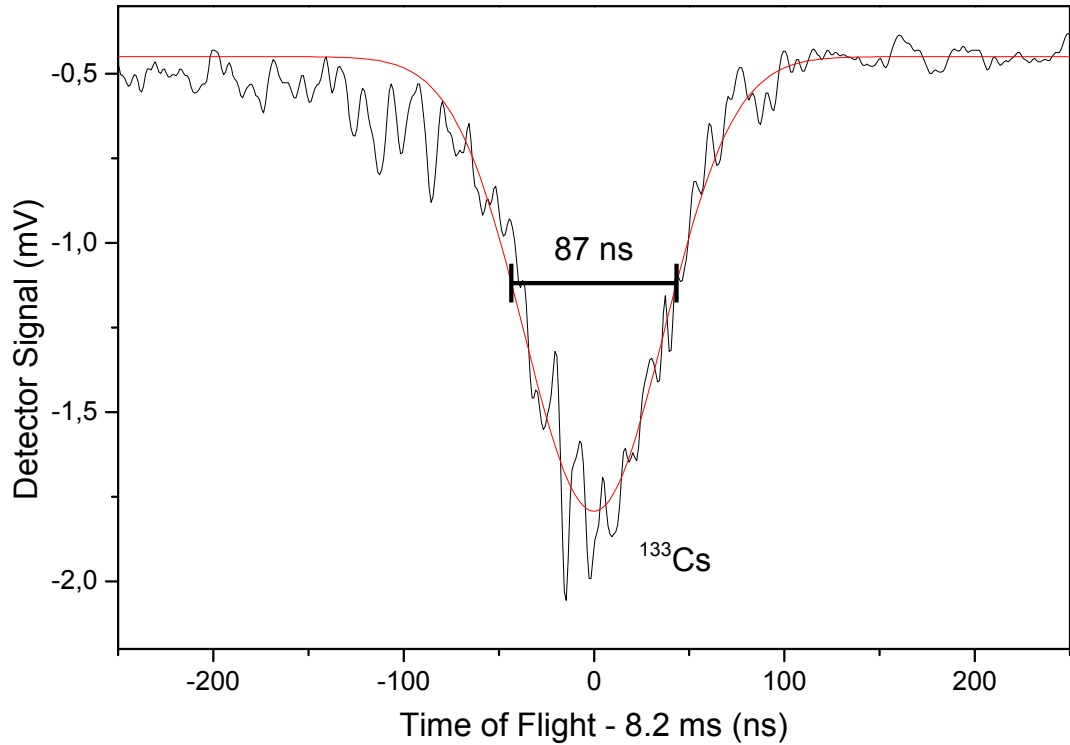
Figure 5.3.: Mass spectrometry peak of ^{133}Cs with a width of 86.5 ns after $\approx$ 8.2 ms TOF resulting in a mass resolving power of $m/\Delta m_{\mathrm{FWHM}} \approx$ 47, 000.

Possible reasons for the reduced resolving power are misalignments in the analyzer and trap system, instabilities in the electronics and optimization in a local optimum without finding the global optimum. Increase in the kinetic energy of the ions to the nominal value of 1, 300 eV is going to reduce the relative energy spread by a factor of two. This will increase the resolving power as well. However, limitations in available time made it impossible to perform all measures to achieve the envisioned mass resolving power.

At a different optimization point, several spectra with increasing turn number and consequently time-of-flight were taken (Figure 5.4). The increase of resolving power as predicted by Equation 2.33 can be seen with a fit result of $\Delta T_0 = 13$ ns well in agreement with the theoretical turn-around time and $\Delta T_{\mathrm{turn}} = 0.54$ ns. Also, the double exponential decrease of ions due to residual gas collisions with decay constants of 0.1 ms and 7.3 ms are shown. The faster component is likely the adaption of the injected ion population to the analyzer acceptance, indicating misalignment. The slower component is due to collisional losses with gas in the analyzer. This corresponds to losses of 50 % in 5 ms which can be improved by reduction of the buffer gas pressure in the trap system and by increasing the pumping speeds.
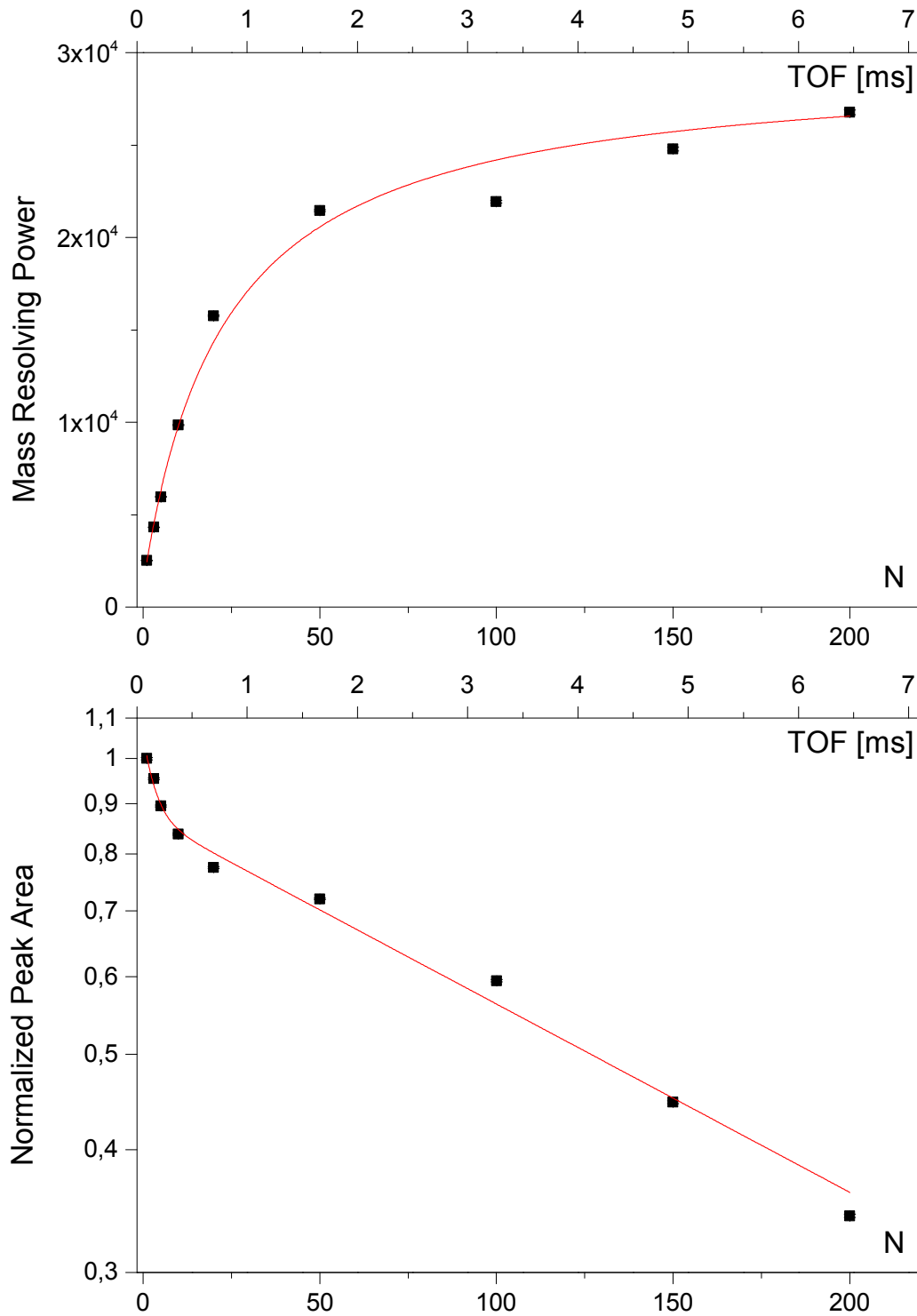
Figure 5.4.: Mass resolving power and relative efficiency vs TOF. The correspond-
ing multiturn number performed N is shown as well. Additional to
this, one TFS turn is performed. Fits included are Equation 2.33 for
resolving power with the results $\Delta T_0 = 13\,\text{ns}$ and $\Delta T_{\text{turn}} = 0.54\,\text{ns}$
and double exponential decay with time constants of $0.1\,\text{ms}$ and
$7.3\,\text{ms}$ for relative efficiency. This is likely to be caused by adaption
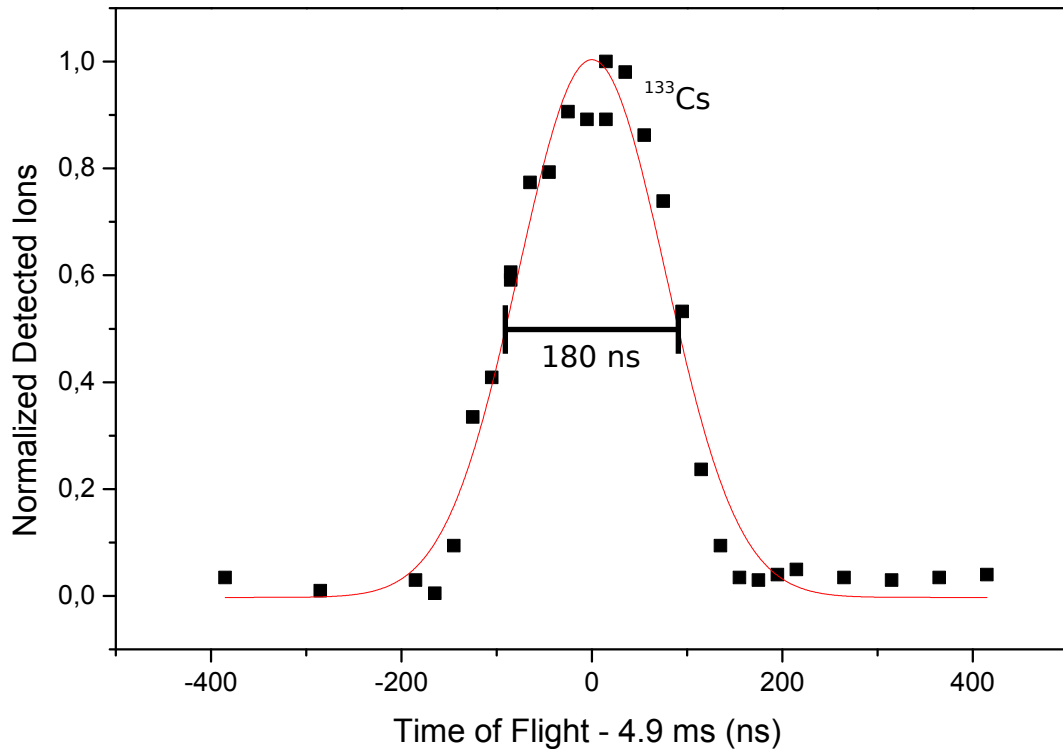of the injected ions to the analyzer acceptance and due to collisional
losses.

Figure 5.5.: Mass-selective retrapping of ^{133}Cs after 4.943 ms TOF corresponding to 154 turns. Ions were separated, retrapped and ejected into the analyzer for one turn. Shown is the peak area of the ions versus the delay time at which the trap was closed. Peak width (FWHM) is 181 ns resulting in $13,650$ mass resolving power.

5.4. Separation by Mass-Selective Retrapping

In order to demonstrate retrapping of temporally separated ions, the ions were injected into the analyzer, separated in a variable number of turns, then retrapped. Either full operation with transport into the ejection trap and detection on the MagneTOF detector or ejecting the ions onto the MCP detector were possible. Using the MCP detector has the advantages of reduced complexity and the ability to compare efficiencies without taking detector differences into account. Direct ejection onto the detector would result in a spread out signal since the time focus is not achieved. Therefore, for this measurement, the ions were stored in the analyzer for one additional TFS turn to produce a narrow peak that allows easy peak area determination.

The measurement was performed with ^{213}Cs at a flight time of about 5 ms (153 MT turns, 1 TFS turn) with a shallower trap depth (± 10 V as opposed to the usual ± 20 V) in order to allow more selective trapping as described in subsection 3.3.5. In the current setup, the trap depth can not be changed during ion flight. Therefore also the injection into the analyzer was performed with the shallow trap setting. In Figure 5.5, a plot of the peak area in dependence of trap
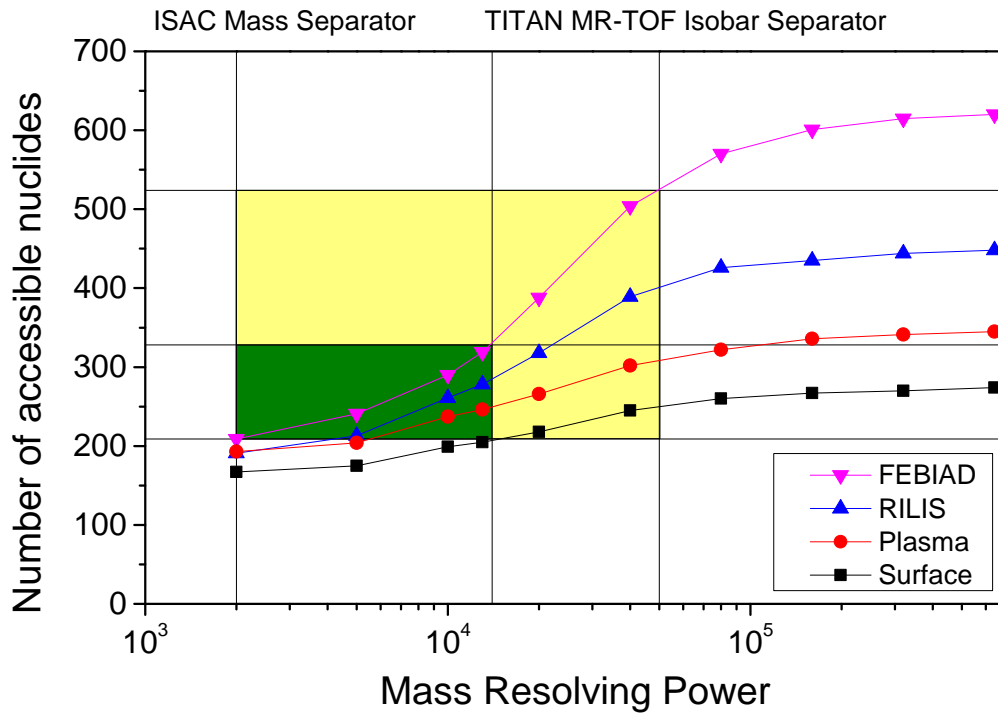
Figure 5.6.: Recap of Figure 2.8, showing the accessible nuclides as defined before for an ISOL facility in dependence on available mass resolving power for the various ion sources. Shown here is the resolving power of the ISAC mass separator and the presently reached resolving power for the MR-TOF-IS, giving an increase in accessible nuclides as shown by the green rectangle. The expected resolving power of 50,000 and its number of accessible nuclides are shown in yellow.

closing delays can be seen, showing the peak form of the trap acceptance over time and demonstrating a resolving power for mass-selective retrapping of close to 14,000.

Figure 5.6 shows a comparison of accessible nuclides in ISOL facilities with the resolving power available from the ISAC mass separator compared to the presently achieved for separation of the MR-TOF-MS Isobar Separator. It can be seen that, depending on the ion source, the accessible nuclides for the TITAN setup increases approximately by factor of 1.5. Shown as well is the gain in accessible nuclides for the expected resolving power of $50,000$ [Lang, 2016].

6. Direct Mass Measurements at the FRS Ion Catcher MR-TOF-MS

The experimental capabilities of an MR-TOF-MS was shown at the FRS Ion Catcher at GSI during a beamtime in 2012 [Plaß et al., 2013]. Here, heavy projectile fragments were produced, separated, stopped in a cryogenic stopping cell and direct mass measurement and separation performed.

In addition to the characterization of the cryogenic stopping cell, a group of nuclides was measured as a demonstration experiment. This served to showcase the capability of multiple-reflection time-of-flight mass spectrometers to perform precise mass measurements in a hybrid in-flight setup for the challenging case of heavy, short-lived and rare nuclides. These where ^{211}Rn, ^{211}Po, ^{211}Fr, ^{213}Rn and ^{213}Fr. As part of this thesis, the measurement and analysis of the ^{213}Rn and ^{213}Fr measurement is presented.

6.1. Experimental Setup

The FRS Ion Catcher is an experiment situated at the GSI FRS, which is a precursor of the future low-energy branch of the Super-FRS at FAIR. As a hybrid in-flight experiment, it consists of four components, the fragment separator with its detectors and degrader systems, the cryogenic gas-filled stopping cell, an RFQ based beam transport and diagnostics unit and the MR-TOF-MS. The setup is schematically shown in Figure 6.1 and as a photograph in its 2012 configuration in Figure 6.2.

6.1.1. Fragment Separator FRS

Relativistic ions from the production target of the FRS (see also subsection 2.2.1) are first separated by magnetic rigidity ($B\rho$). In the middle focal plane, a set of disc, wedge and uniform degraders perform both isotropic and position-dependent slowing of the ions (ΔE) which can be chosen to result in an optimum separation of the species of interest in the second part of the magnetic rigidity separation, in an optimum range bunching in the gas cell or in a compromise of both. In the Super-FRS, two stages of $B\rho - \Delta E - B\rho$ separation will be combined with a
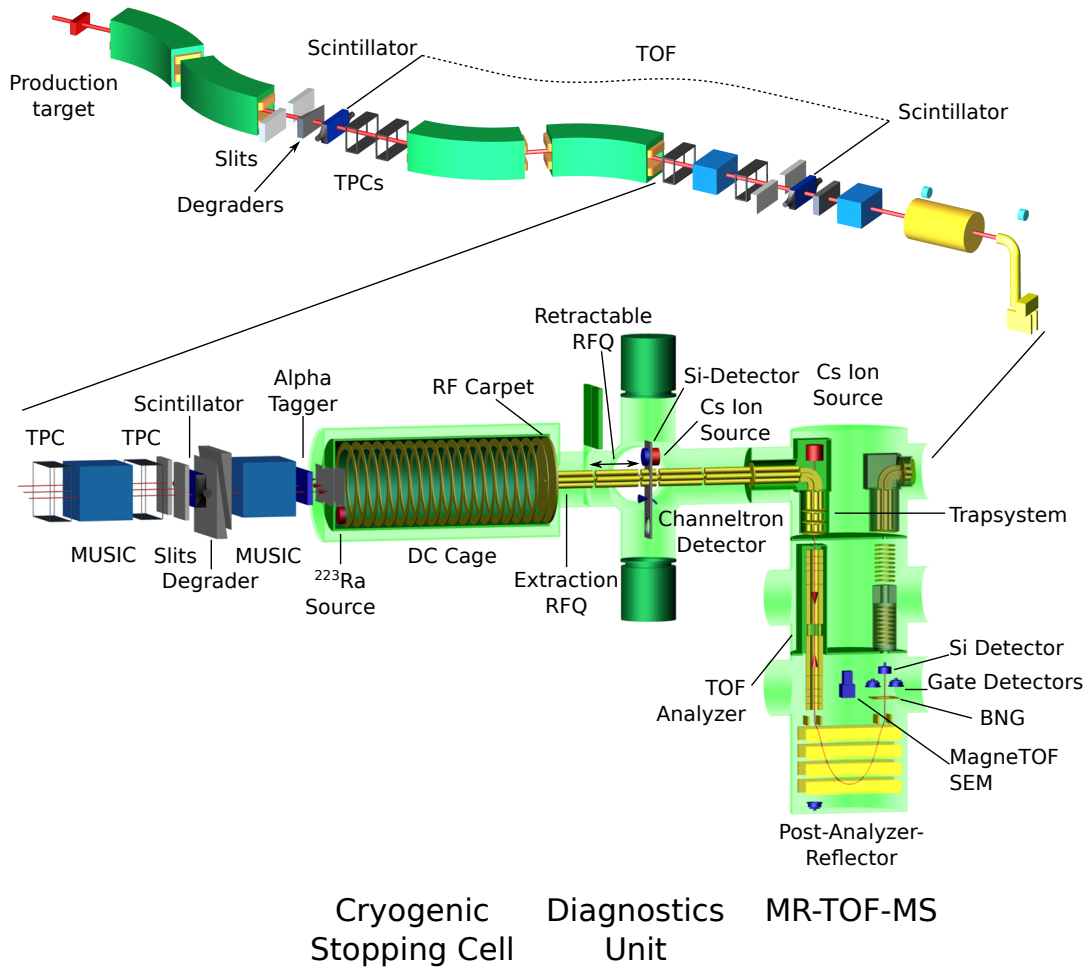
Figure 6.1.: Ioncatcher schematic overview 2012.

separate range bunching to achieve both optimum separation and optimum range bunching into the stopping cell.

A series of detectors in the FRS allow particle identification as well as optimization of the instrument settings. Two scintillators situated in the middle focal plane and before the stopping cell provide TOF information, four time-projection chambers (TPC), two each at the middle focal plane and at the end of the FRS allow information about the magnetic rigidity of the particles to be gathered while a multiple sampling ionization chamber (MUSIC) gives information about the energy loss in gas of the fully stripped particles and therefore about the element via the Z-dependency of the energy loss. The combined information allows ion-by-ion identification of the particles passing the FRS. Slits both at the middle and the end focal plane remove the unwanted particles [Geissel et al., 1992].

In front of the stopping cell, a homogenous adjustable degrader allows to shift
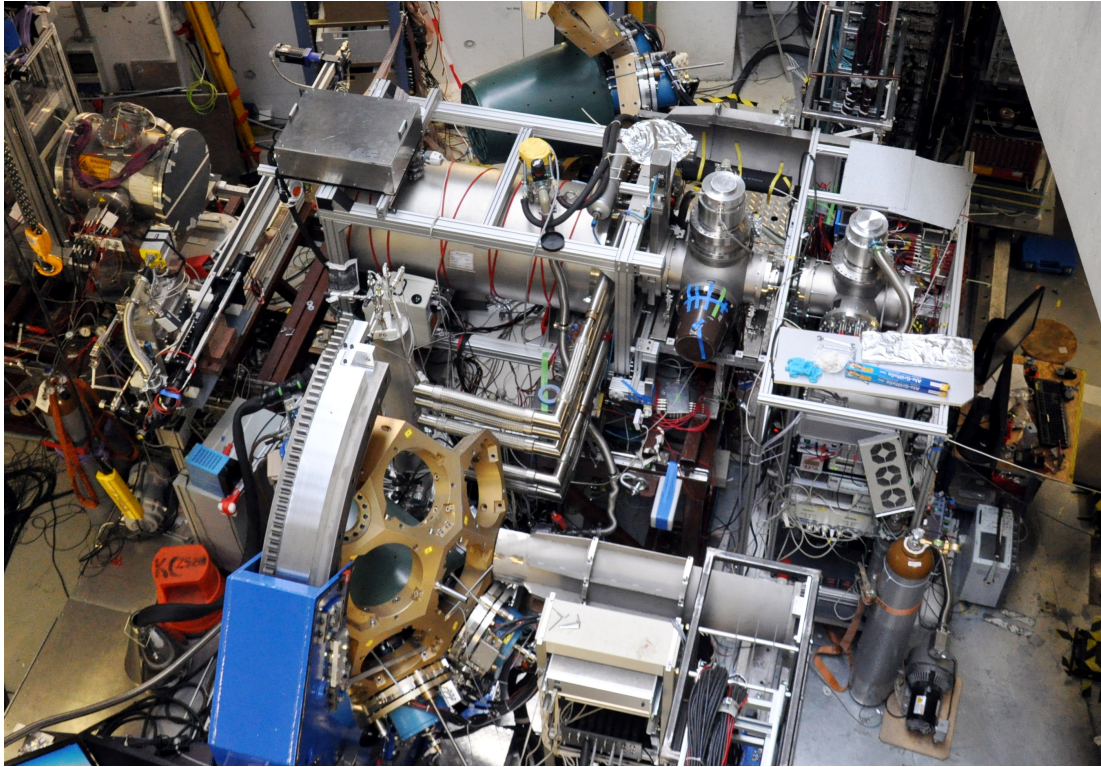
Figure 6.2.: Photo of the Ion Catcher Setup 2012. On the left, the degrader wedges, the last MUSIC and the Alpha Tagger can be seen, in the middle the Cryogenic Stopping Cell and on the right Diagnostics Unit and MR-TOF-MS.

the particle range into the acceptance of the stopping cell. This is performed by scanning the number-distance-curve with the MUSIC directly in front of the gas cell and adjusting the degrader accordingly. An additional option to identify the particles is the alpha tagger, a double-sided silicon strip detector that can be moved into the beam in front of the stopping cell.

6.1.2. Cryogenic Stopping Cell

The overall efficiency of a stopping cell consists of the stopping efficiency and the extraction efficiency. The stopping efficiency describes the amount of particles that are stopped in usable charge states in the gas and depends on the beam characteristics (mainly its size and energy distribution) and the corresponding active area of the stopping cell and the areal density available. The extraction efficiency is the ratio of particles that can be transported out of the cell afterwards.

In order to improve the cleanliness of the cell, leading to less ionized products and losses due to charge exchange reactions, the Ion Catcher stopping cell was constructed as a cryogenic stopping cell (CSC). In an inner, superinsulated vessel, Helium can be kept at temperatures as low as $70\,\mathrm{K}$ and at pressures up to

125 mbar resulting in an areal density of $7\,mg/cm^2$, equivalent to a pressure of 430 mbar at room temperature [Plaß et al., 2013]. Ions are injected through two metal windows into the gas volume in which part of the energy distribution is stopped and thermalized. A set of DC cage electrodes drags the ions to the extraction end, reaching shorter extraction times. Here, a set of concentric rings with applied RF, the RF carpet, repulses the ions. A superimposed DC gradient guides the ions to the extraction nozzle through which they are transported by the gas flow [Ranjan et al., 2011, Purushothaman et al., 2013].

A ^{223}Ra recoil source is integrated in the stopping cell to generate testing and calibration ions.

6.1.3. Diagnostics Unit

Ions passing the nozzle enter the extraction RFQ of the diagnostics unit. Here, differential pumping is performed with two 1000 l/s turbomolecular pumps. The pumping speed allows to reach a pressure of 10^{-2} mbar, needed for transport of the ions in RFQs.

Part of the transport RFQ can be moved by means of an elevator setup and replaced by a either a silicon detector, a channeltron detector or a Cs ion source. This mechanism as well allows the retract the extraction RFQ from the stopping cell in order to separate the stopping cell with a gate valve [Plaß et al., 2013].

6.1.4. Multiple-Reflection Time-Of-Flight Mass Spectrometer

The MR-TOF-MS in the Ion Catcher setup differs from the TITAN system described in chapter 3 due to lower transport potentials in the RFQ system, an injection trap system that also performs potential shifting of the ions inside, the larger size of the analyzer and the presence of a post analyzer reflector which allows to project a time focus on the following detector or Bradbury-Nielsen Gate [Bradbury and Nielsen, 1936]. In the deflection direction of the BNG, two small MCP detectors are placed that allow to detect the ions deflected by the BNG. In the final setup, a system consisting of Energy Buncher, Deceleration and Accumulation Trap will allow to trap separated particles and transfer them to further experiments. In the beamtime, a Silicon detector was placed after the BNG to allow mass selective alpha spectroscopy [Dickel et al., 2015].

6.2. FRS Ion Catcher Beamtime 2012

In the beamtime, a primary beam provided by the GSI accelerator system of ^{238}U at an energy of $1\,\mathrm{GeV/u}$ was directed on a beryllium target with an areal density of $1.6\,\mathrm{g/cm^2}$, producing exotic nuclides via fragmentation reactions. A niobium stripper foil with an areal density of $0.2\,\mathrm{g/cm^2}$ ensures a full ionization of the products.

The FRS provides two-fold magnetic-rigidity analysis. By placing a monoenergetic degrader in the middle, energy-dispersive plane, both spatial separation of single nuclides as well as a reduction of the energy spread of the particles is possible. This is required for efficient stopping in the CSC due to overly large areal density that would be required without.

A homogenous degrader of variable thickness is used to adjust the energy of the selected fragments so that they are stopped in the CSC. For this, the degrader thickness is scanned and the particles stopped in the MUSIC in front of the CSC. Afterward the degrader thickness is reduced so the fraction, that is stopped in the gas of the CSC, is maximized.

Position-sensitive detectors and scintillators in the middle and end focal planes of the FRS allow to measure the magnetic rigidity and velocity of the particles, respectively. A MUSIC allows to infer information about the nuclear charge and therefore the element. This set of detectors allows event-by-event identification of the nuclides transported through the FRS. Further identification is performed by α-spectroscopy in the diagnostics unit and finally by the MR-TOF-MS.

During the 21 shifts of 8 hours each in the 2011 and 2012 beamtimes, the FRS Ion Catcher setup was commissioned, marking the first on-line operation of a cryogenic gas filled stopping cell. Mass measurements were performed on ^{211}Po, ^{211}Fr and ^{213}Fr and the radon isotopes ^{211}Rn and ^{213}Rn with ^{211}Pb serving as calibrant. For some nuclides this was the first direct mass measurement [Purushothaman et al., 2013].

For this thesis, the measurement and evaluation of ^{213}Fr and ^{213}Rn, using ^{211}Pb for calibration, will be shown.

6.3. Data Evaluation Method

MR-TOF-MS has been shown as excellent method of mass measurement for exotic nuclides. This directly entails low count rates and possibly overlapping, non-Gaussian peaks at strong intensity differences. Since the standard method of binning the data and χ^2-fitting a Gaussian distribution to the data would result
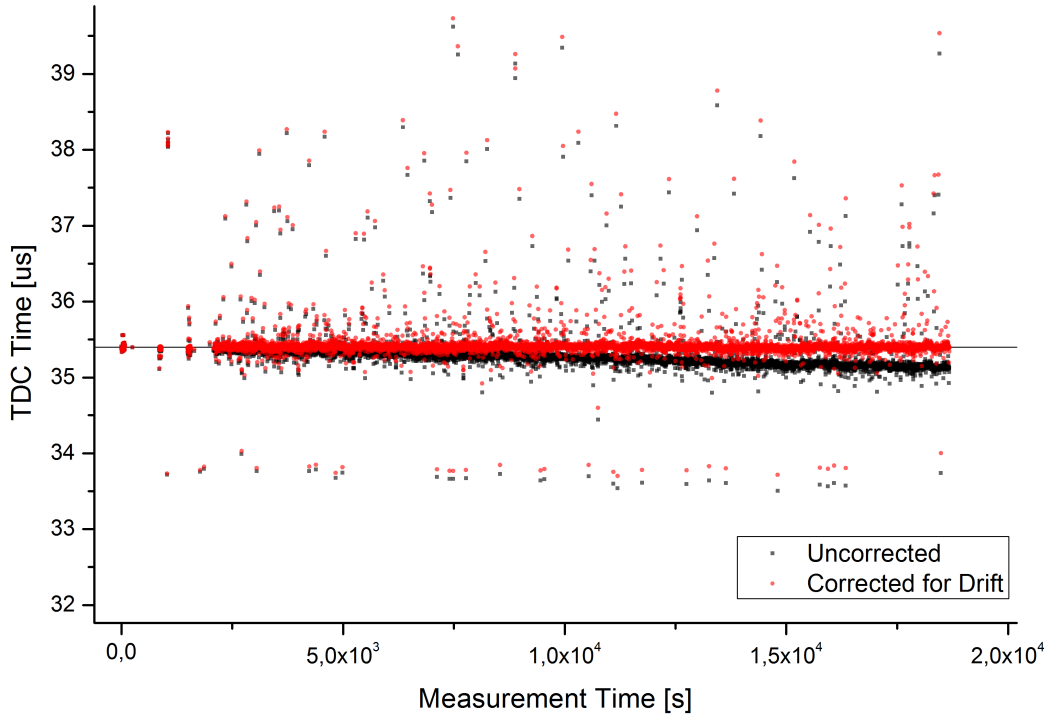
Figure 6.3.: Flight times of the ^{213}Rn measurement plotted against the measurement time. Shown in black is raw data and in red events corrected for the drift of the calibrant peak.

in a strong loss of accuracy, a special data evaluation method is required and will be presented here.

6.3.1. Mass Calibration and Drift Correction

Measurement durations of several hours with just a few events make consideration of instrument drift relevant. To compensate this drift, calibrant spectra are taken in chosen intervals and used to time-dependently calibrate the full spectrum.

In order to arrive at mass values for time-of-flight data, Equation 2.15 can be rewritten as

$$\frac{m}{Q} = a \left(t_{\text{TOF}} - t_0 \right)^2 \tag{6.1}$$

with t_0 the data acquisition delay and a a constant to be determined from calibration spectra. For MR-TOF-MS with differing turn numbers for the species in the analyzer and the additional requirement of measurements over longer times, the calibration formula is extended in the following way [Haettner, 2012]:
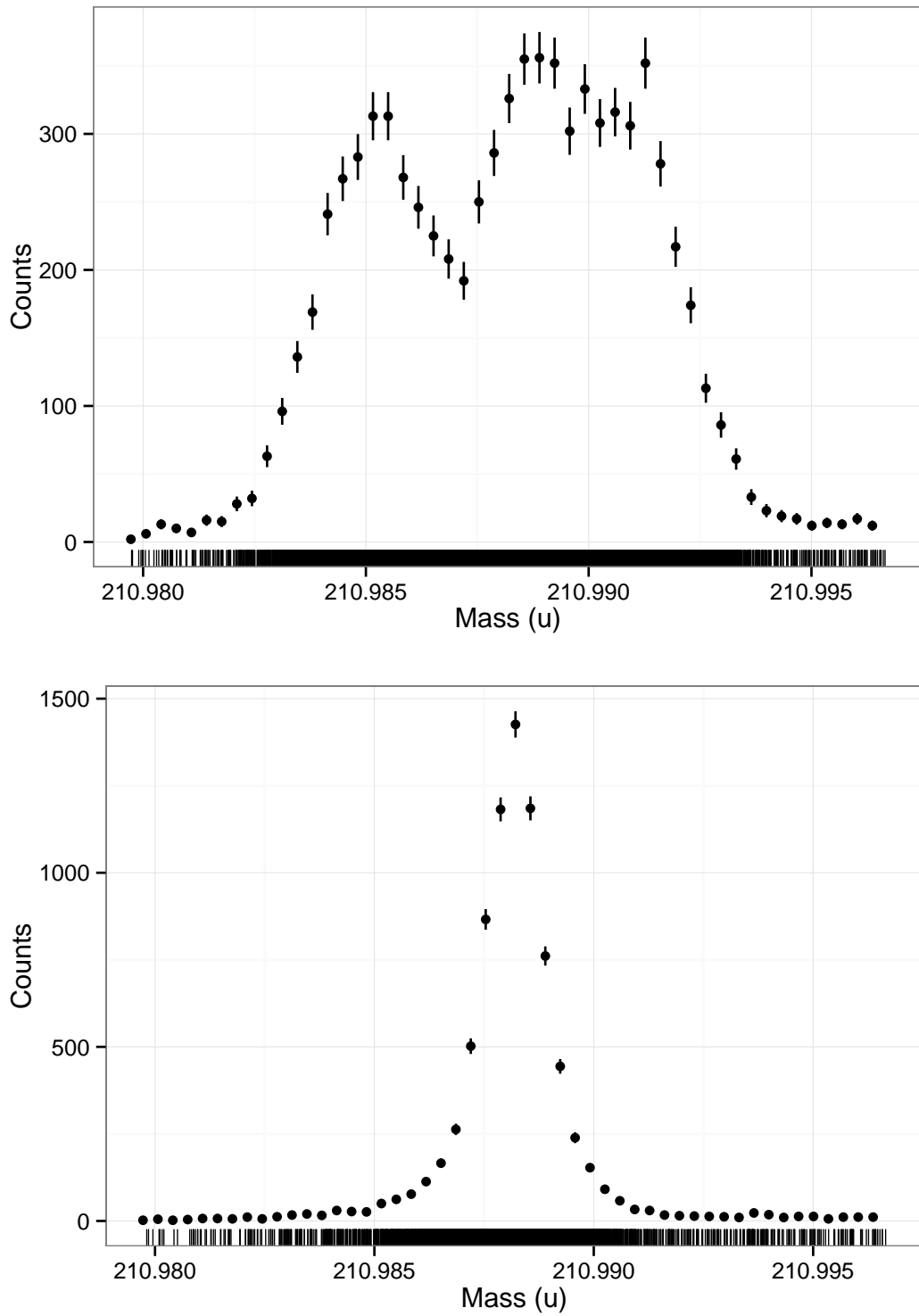
Figure 6.4.: Peakform for the ^{211}Pb from the ^{213}Rn measurement without (top) and with drift correction (bottom). The improvement can be clearly seen.

$$\frac{m}{Q} = c \, \frac{(t_{\mathrm{TOF}} - t_0)^2}{(1 + Nb)^2} \tag{6.2}$$

Here, N is the number of turns, c the calibration factor for the shoot-through time of flight, while b is representing the difference of one turn in the analyzer to the shoot-through mode. Due to the stronger influence of the applied voltages in multiturn mode, b is treated as time dependent and used for time resolved calibration while c is assumed to be time-independent. This calibration also assumes that the time for one turn is constant for each shot.

In order to account for the drift of the spectrum which can be seen in Figure 6.3, calibrant spectra are taken in certain intervals. The peak is fitted with a Gaussian using Origin [OriginLab, 2016] to obtain the time-of-flight and, with the predetermined parameters c, t_0 and the calibrant mass, b is calculated for every calibration point.

For calibration of the spectra, both the time-of-flight and the measurement time is read for each event. b is linearly interpolated between the calibration points and the corresponding mass for the event written into the file for the calibrated spectrum, arriving at a time resolved calibration. In Figure 6.4 the effect on the peak can be seen in the restoration of the narrow width.

6.3.2. Peak Shape

In the case of overlapping peaks with strongly different abundances, the information available for the tails of the distribution of the intense peak limits the information about the less intense peak, being in many cases the nuclide of interest. Therefore, a distribution has to be found that closely describes the peak shape also in the tails.

The probability density function used for the peak fits is an exponentially modified Gaussian (EMG) [Foley and Dorsey, 1984] with multiple exponential components on each side [Purushothaman et al., 2016]:

$$\mathrm{EMG}(x, \mu, \sigma, \vec{\eta}, \vec{\tau}) = \frac{1}{4} \sum_{i=1}^{N} \frac{\eta_i}{\tau_i} \exp\left(\frac{1}{2} \left(\frac{\sigma}{\tau_i} \right)^2 + \zeta_n \frac{x - \mu}{\tau_i} \right) \cdots$$
$$\cdots \mathrm{erfc}\left(\frac{1}{\sqrt{2}} \left(\frac{\sigma}{\tau_i} + \zeta_i \frac{x - \mu}{\sigma} \right) \right)$$
$$\mathrm{with} \sum_{i=1}^{k} \eta_i = \sum_{i=k+1}^{N} \eta_i = 1 \, ; \, \zeta_{1\ldots k} = +1 \, ; \, \zeta_{k+1\ldots N} = -1 \tag{6.3}$$
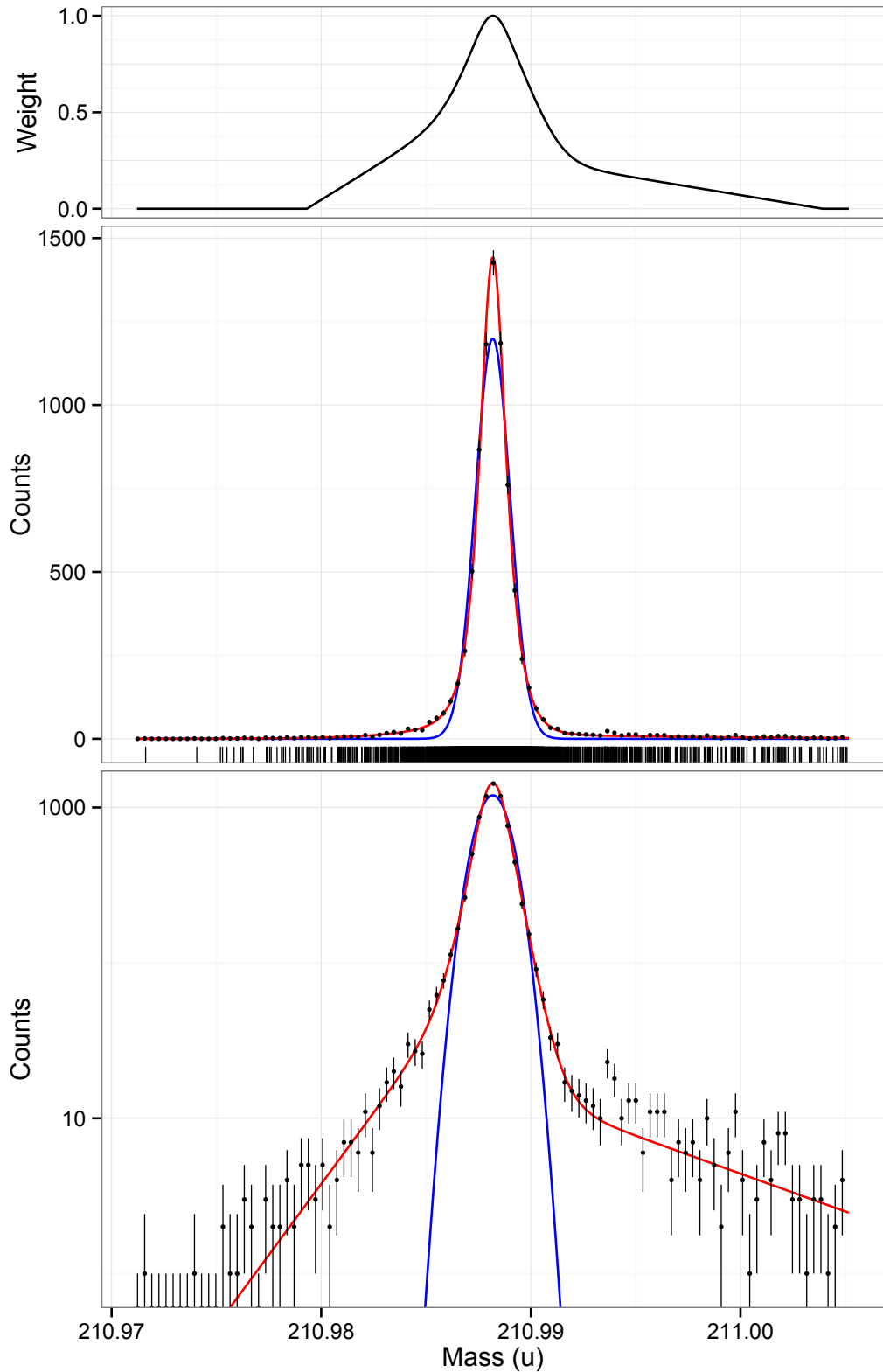
Figure 6.5.: Comparison of a normal distribution and the EMG with the parameters shown in Equation 6.4 and the high statistics ^{211}Pb peak taken from the ^{213}Rn measurement. Error bars are computed as $\sqrt{N+1}$. Shown are both linear and logarithmic y-axes. Additionally, the weighting function for the MLE fit is visualized.

with the parameters x_0 for the mean of the normal distribution, σ^2 the variance of the normal distribution, the weights of the exponential components η_n, normalized to 1 for each side, and the relaxation times τ_n.

In former measurements, the stability of the peak form for different masses in the same measurement and over time was shown (Figure 6.6). This allows to assume identical peak shapes for all measurements, estimating only the mass of the measured particles.

Using the software Igor [WaveMetrics Inc., 2015] for a fit with the high statistics ^{211}Pb peak taken during the ^{213}Rn measurement, the peak parameters can be determined to be [Purushothaman, 2015]

$$
\begin{aligned}
\sigma &= (3.5 \pm 0.3) \cdot 10^{-4}\,\mathrm{u} & N &= 4 \quad k = 2 \\
\eta_1 &= (0.80 \pm 0.03) & \eta_2 &= (0.20 \pm 0.03) \\
\eta_3 &= (0.90 \pm 0.01) & \eta_4 &= (0.10 \pm 0.01) \\
\tau_1 &= (5.32 \pm 0.37) \cdot 10^{-4}\,\mathrm{u} & \tau_2 &= (2.37 \pm 0.22) \cdot 10^{-3}\,\mathrm{u} \\
\tau_3 &= (5.85 \pm 0.21) \cdot 10^{-4}\,\mathrm{u} & \tau_4 &= (8.91 \pm 0.89) \cdot 10^{-3}\,\mathrm{u}
\end{aligned}
\tag{6.4}
$$

The number of exponential components was chosen by fitting increasing numbers of components and rejecting the first set with parameter errors larger than the parameter. A fit of the ^{211}Pb peak from the beamtime with EMG and a Gaussian can be seen in Figure 6.5. The mass resolving power (FWHM) for the measurement was about 145,000.

6.3.3. Maximum Likelihood Estimation

Experiments with exotic nuclides typically amass only a very low number of events while still requiring a high accuracy of the derived mass value. The usual approach of binning the data and performing minimum χ^2 estimation requires a minimum number of counts per bin to arrive at meaningful statistics [Taylor, 1982]. This would require very broad bins which, in turn, makes the information loss through the binning unacceptable.

A solution for these problems is the estimation of the distribution parameters by unbinned fitting, namely with the maximum likelihood estimator (MLE) [Fisher et al., 1912, Aldrich, 1997].

Here, the corresponding parametric probability density function $f(x, \vec{\Theta})$ with the vector of parameters $\vec{\Theta}$ is searched. The value of $f(x_i, \vec{\Theta})$ represents the probability of measuring the value x_i. By multiplying the probabilities for the ensemble of observations $\vec{x} = x_1, x_2, ..., x_n$ the likelihood function
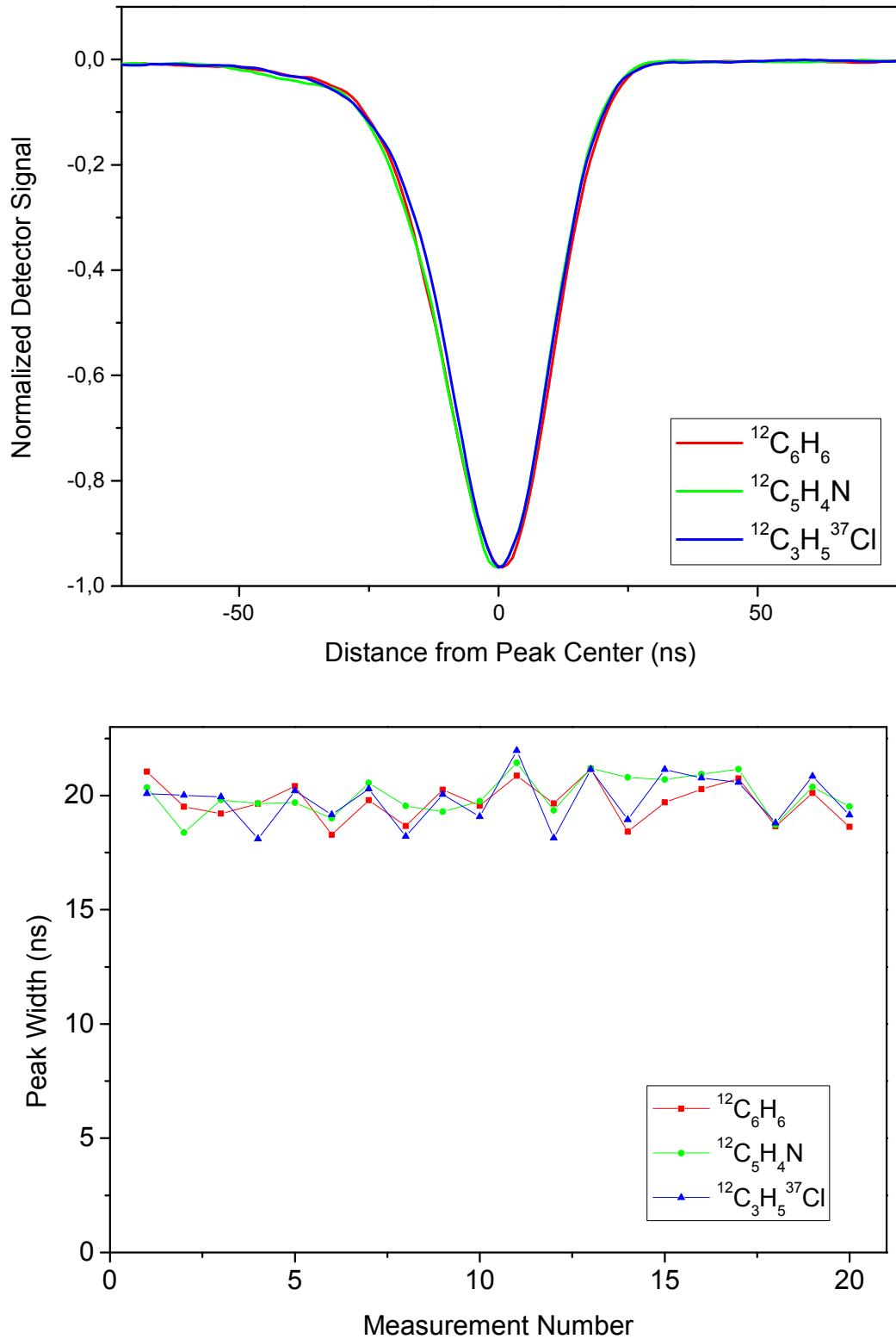
Figure 6.6.: Mass measurement of an isobar triplet allows to compare the peak form of different species in the analyzer at the same time. The peak form does not show dependency on the species or change significantly over time [Dickel, 2010, Dickel, 2016].

$$\mathcal{L}\left(\vec{\theta}, \vec{x}\right) = \prod_{i=1}^{n} f\left(x_i, \vec{\Theta}\right) \tag{6.5}$$

can be computed. It reaches its maximum when the probability density function $f(\Theta)$ describes the data best. Therefore, maximizing $\mathcal{L}(\theta, x_n)$ by variation of

represents the probability of the density function $f(\Theta)$ being the distribution responsible for generating the observations.

Often the negative logarithmic likelihood

$$-\ln\mathcal{L}\left(\vec{\theta}, \vec{x}\right) = -\sum_{i=1}^{n} \ln\left(f\left(x_i, \vec{\Theta}\right)\right) \tag{6.6}$$

is used. This allows minimizing a sum instead of maximizing a product which is computationally beneficial.

For a single peak fit, Equations 6.6, 6.3 and 6.4 are combined with a weighting function and the measurement mass events x_n. Used as a weighting function is the logarithm of the EMG function with an inital μ. Values below zero are set to zero. The remaining open parameter is μ, the mass of the measured nuclide. Minimization of Equation 6.6 by variation of the open parameter results in estimation of μ. Now, the result for μ is taken as parameter for the weighting function and the fitting is iterated until the value converges.

Further evaluation of the method and extension to multi-peaks can be found in [Ebert, 2016].

6.4. Results

For the measurements, the FRS was set to transmit ^{213}Fr and ^{213}Rn, respectively. Particles were identified by the FRS and additionally verified by alpha spectroscopy in front of the stopping cell. Counts in the MR-TOF-MS correlate with the injected beam into the stopping cell. Also, masses are in the correct range.

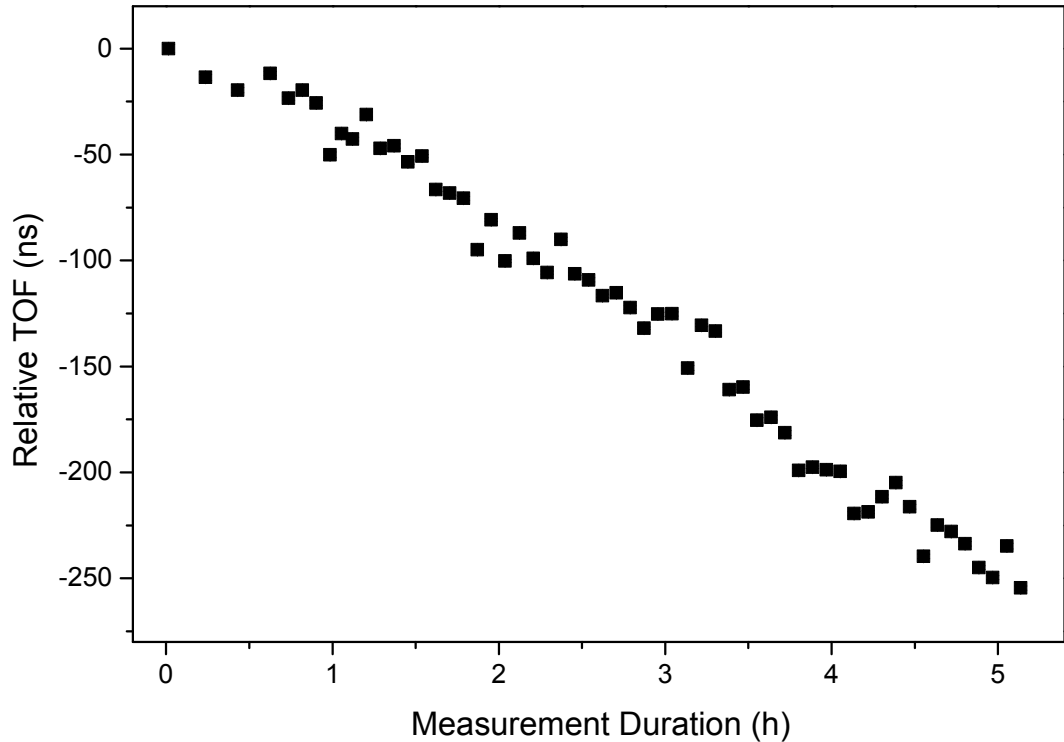The MR-TOF-MS was tuned to a resolving power of about $145,000$.

Figure 6.7.: Mean values of a Gaussian fitted to segments of the ^{211}Pb TDC data from the ^{213}Rn measurement, showing the drift. Error bars are smaller than the symbol.

6.4.1. Fitting Procedure

The TDC data from the experiment was segmented (by time or by active reference source) and the lead peak from the internal source fitted with a Gaussian using χ^2-fitting in Origin. The resulting drift can be seen in Figure 6.7. Utilized are the parameters t_0, c and N. While t_0 is taken from the electrical setup, N can be deduced from the measurement timing, c is taken from the broadband spectrum shown in Figure 6.8.

$$t_0 = 162.8\,\text{ns} \quad ; \quad c = 3.933727 \cdot 10^{-8}\,\text{u/ns}^2 \quad ; \quad N = 205 \tag{6.7}$$

With Equation 6.2, the b values for each calibration segment were calculated. Finally, the measured data was calibrated and drift corrected at the same time using $N = 205$ and $N = 204$ and linearly interpolating the b values between calculated segment values, arriving at a list of 'mass events'.

This list was consequently cut to a region ± 10 FWHM, loaded into the software environment for statistical computing and graphics R [R Core Team, 2015] and fitted by minimizing Equation 6.6 with variable μ and fixed parameters for the EMG found before (Equation 6.4). In order to minimize the influence of stray
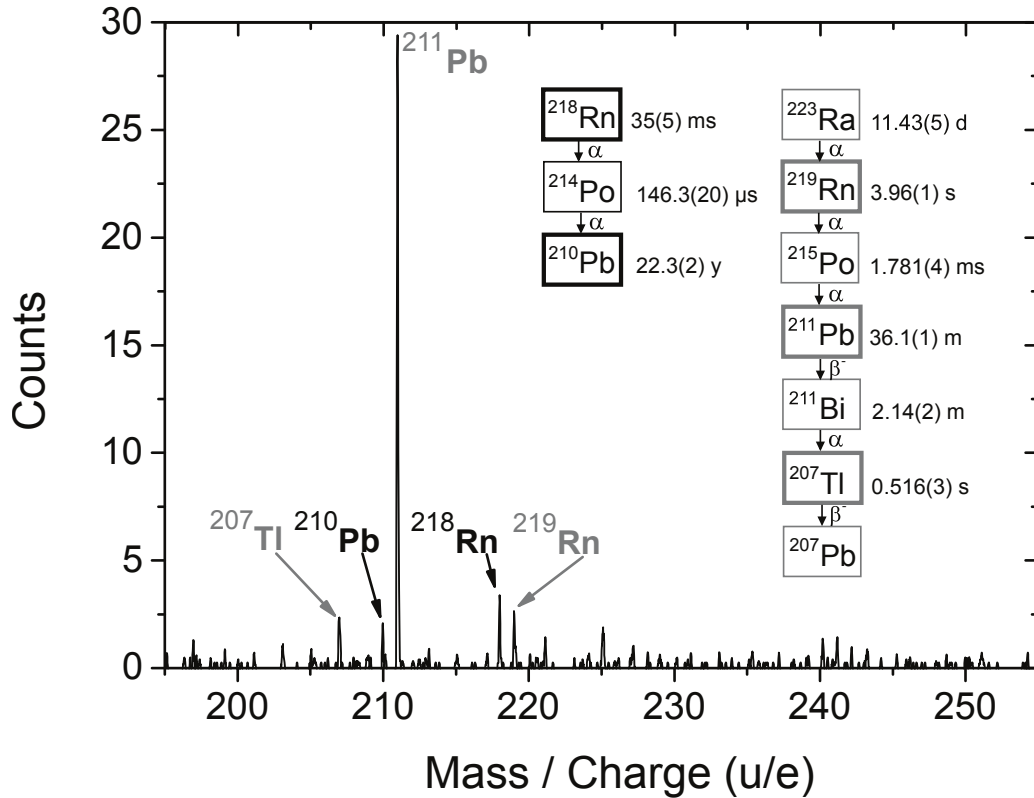
97

Figure 6.8.: Broadband spectrum from shoot-through mode of the CSC output with injected ^{218}Rn-beam, taken for a duration ≈ 35 min. Shown in black are the injected beam and its daughter, the identified nuclides from the internal source are shown in grey. This spectrum is used for determination of c, as proof for sufficiently fast and efficient transport of Rn and for estimation of background in the ^{213}Rn measurement [Purushothaman et al., 2013].

counts on the fit result, the log likelihood function itself was used as a weighting factor with the μ of the previous iteration as fixed parameter.

Figure 6.9 shows the fits for ^{213}Fr and the corresponding calibrant ^{211}Pb, Figure 6.10 those for ^{213}Fr and, again, the corresponding calibrant ^{211}Pb. The data is shown binned for visualization; the fit was performed unbinned as described before. The lead data shows good agreement with the fitted curves. For both the ^{213}Fr and ^{213}Rn measurement, an additional peak is visible to the lower and higher mass side, respectively. These peaks are positioned at low weighting function values and therefore not influencing the mass value.

The ^{213}Rn measurement may appear broadened slightly. This possibly a statistical effect due to the low count number. The broadband spectrum in Figure 6.8 shows one count in the mass area of ^{213}Rn at a measurement duration of about 35 minutes. Should this be an event of contamination and not a random dark
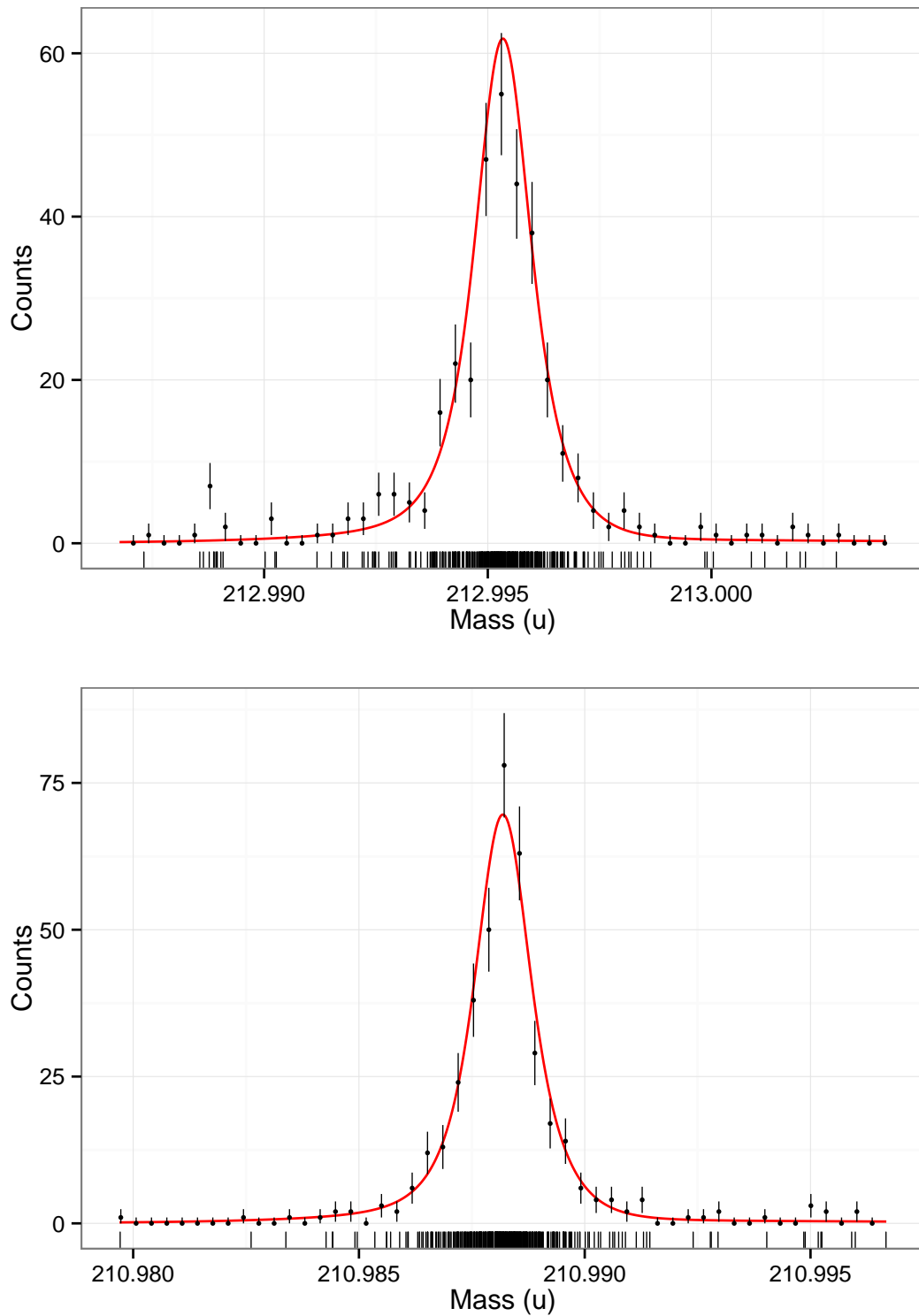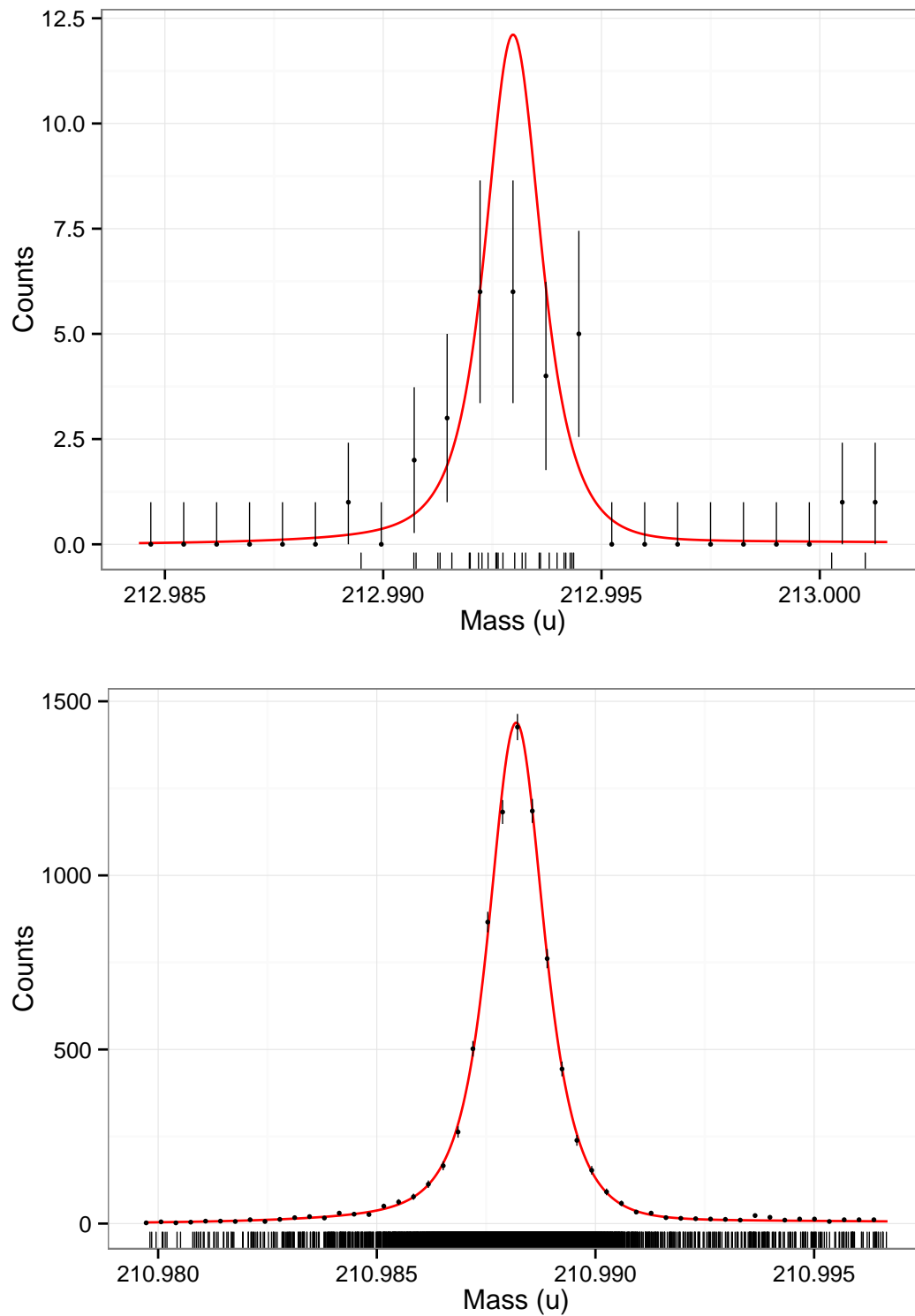
Figure 6.9.: Plots for the mass measurement of ^{213}Fr. Shown are the probability density function, raw and binned data with $\sqrt{N+1}$ error bars for both ^{213}Fr (top) and the corresponding calibrant ^{211}Pb (bottom). Binning was performed only for visualization and is not used for the fit.

Figure 6.10.: Plots for the mass measurement of ^{213}Rn. Shown are the probability density function, raw and binned data with $\sqrt{N+1}$ error bars for both ^{213}Rn (top) and the corresponding calibrant ^{211}Pb (bottom). Binning was performed only for visualization and is not used for the fit.

Nuclide Name	$^{211}\mathrm{Pb}^+$ (Fr)	$^{211}\mathrm{Pb}^+$ (Rn)	$^{213}\mathrm{Fr}^+$	$^{213}\mathrm{Rn}^+$
Counts	390	8100	346	29
Half-Life	36.1 min	36.1 min	34.82 s	19.5 ms
Fit Value (u)	210.9881668	210.9881863	212.9953162	212.9929724
Recalibrated (u)	210.9881886	210.9881886	212.9953382	212.9929747
Non-Ideal Eject. (u)			212.9954674	212.9931039

Table 6.1.: Fit results for the two calibration peaks and the measured masses in the +1 charge state. Shown are the number of counts in the spectrum, the fit value, fit value after recalibration and corection for non-ideal ejection potentials. Half-lifes taken from [Audi et al., 2012].

count, this contamination rate would scale to approximately 10 events within the 315 minutes duration of the ^{213}Rn measurement. This agrees well with the two additional counts that can be seen on the heavier side of the spectrum. No chemical compounds or isomers are known in the relevant mass range to explain a peak broadening. Additionally, the number of ions delivered to the MR-TOF-MS during measurement was estimated from FRS data and transport efficiency from gas cell to the diagnostic units α-detector [Reiter, 2013]. The estimated 60 ions agree well with the measured 27 counts.

Due to the skew of the EMG compared to the Gaussian, better statistics and the differing methods, a further calibration of the mass values is needed which is done linearily with

$$m_{\mathrm{IoI}} = m_{\mathrm{IoI,meas}} \cdot \frac{m_{\mathrm{cal,lit}}}{m_{\mathrm{cal,meas}}} \tag{6.8}$$

Additionally, during the beamtime, the stability of the analyzer voltages on ejection was deficient. Measurements with identical settings and Cs-ions were performed after the beamtime. The time of opening the mirror and therefore the position of the Cs-ions at opening time was scanned and their flight-time to the detector recorded. Simulations of this post-beamtime experiment allowed to estimate the shift introduced by this non-ideal ejection [Ebert, 2016] to be 0.607 ppm resulting in the mass values for the +1 ions as shown in Table 6.1.

The electron mass has been added for the final value of the neutral mass quoted in subsection 6.4.3.

6.4.2. Error Contributions

Systematic errors considered here are uncertainty of the shift due to the non-ideal ejection potentials of the analyzer, the precision of the interpolated drift correction, the effects of different turn numbers on the mass accuracy and the accuracy
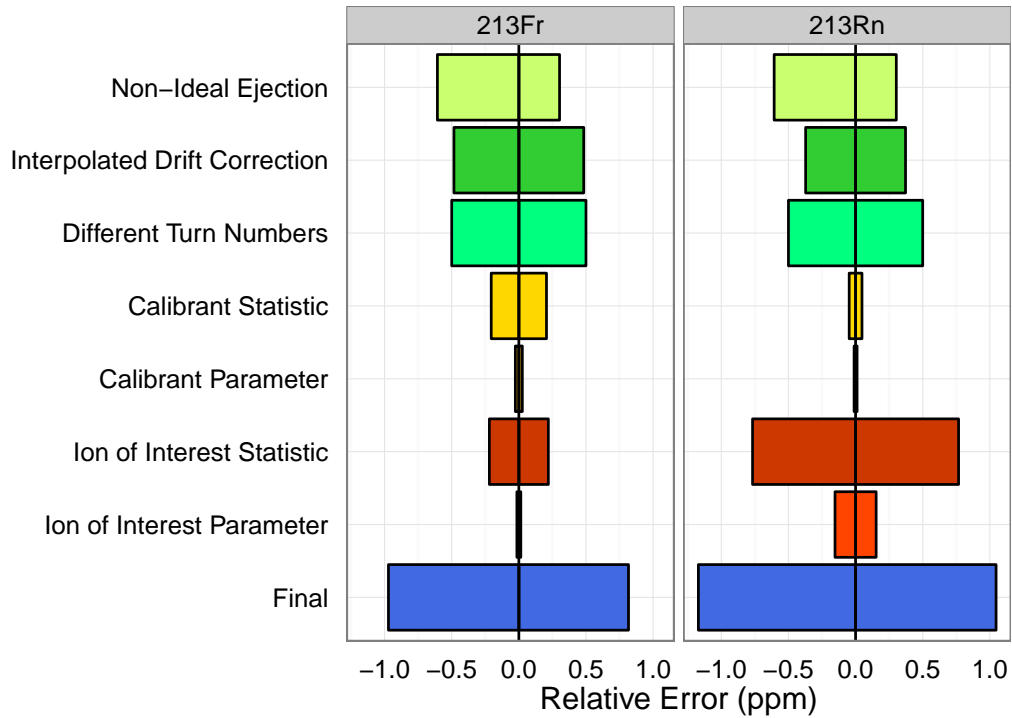
Figure 6.11.: Contributions of the different relative errors to the final error. Due to asymmetry, the errors for non-ideal ejection and the final error are given as two separate values for the positive and the negative error.

	Nuclidename	^{213}Fr	^{213}Rn
Systematic	Non-Ideal Ejection Pos	0.303	0.303
	Non-Ideal Ejection Neg	0.607	0.607
	Interpolated Drift Correction	0.483	0.372
	Different Turn Numbers	0.500	0.500
Fit	Calibrant Statistic	0.206	0.048
	Calibrant Parameter	0.026	0.011
	IoI Statistic	0.220	0.767
	IoI Parameter	0.015	0.153
Final	Pos	0.817	1.046
	Neg	0.971	1.171

Table 6.2.: Relative error contributions in 10^{-6} for the measured nuclides. Due to asymmetry, the errors for non-ideal ejection and the final error are given as two separate values for the positive and the negative error.

of the calibrant. The error of the correction for non-ideal ejection potentials has been estimated as half the correction in positive direction and the full correction in negative.

For the error of the interpolated drift correction, the set of flight times calibrant ^{211}Pb in the ^{213}Rn measurement were taken as basis. The standard deviation of the differences of subsequent calibration points is 0.408 mu. This was divided by the mass and scaled with the inverse square root of the number of drift correction pillars or the number of measured ions of interest, whichever is smaller.

The use of different turn number spectra for measurement and calibration introduces an additional error. Two parts were considered here: Error in estimation of the calibration parameters c, $\vec{b}$ and t_0 and the use of odd and even turn numbers in the same measurement. The latter is problematic as the analyzer is point-to-parallel projecting, creating an odd-even-effect in flight-times. In a simulation, ions were ejected straight and at an angle in both x and y direction so they hit the detector at the edge while still maintaining more than 50% efficiency. Comparison with the straight path, scaling from mass 133 to mass 213 and division by the flight time lead to a maximum error of about 1 ppm. Therefore, 0.5 ppm was estimated as standard error for the odd-even effect of turn numbers. Due to the recalibration and the use of neighboring turn numbers, errors in the calibration parameters are deemed small in comparison to the discussed odd-even error and are neglected.

To account for the uncertainty of the parameters of the fit, the EMG-parameters were each varied in their error and a fit performed with the varied parameter set. The differences to the original fit result are quadratically added.

For the statistical error, synthetic spectra with the same number of counts as the original spectra were generated from the distributions that were estimated in the fit. These were fitted again and the resulting mass value recorded. This was repeated for a large number of times ($100,000$ and $10,000$ in the case of the high statistics lead peak from the Rn spectrum). The standard deviation of those mass values then is assumed as the statistical error.

The contributions to the final error are listed in Table 6.2 and illustrated in Figure 6.11. As can be seen, the error of both measurements is dominated by the error for different turn numbers. This error can be reduced by tuning the instrument for reduction of odd-even effects or choice of even (or odd) turns for both ions of interest and calibrant. After this, the ^{213}Fr measurement is dominated by further systematic errors which can be improved by electronics improvements and instrument tuning. As well, number and statistics of the pillars used for the time resolved calibration can be improved rather easily. In the ^{213}Rn measurement, the measurement is dominated as well by by the statistics. Here, improvement can be found in increasing the resolving power of the spectrometer, reducing the uncertainty at the same time.
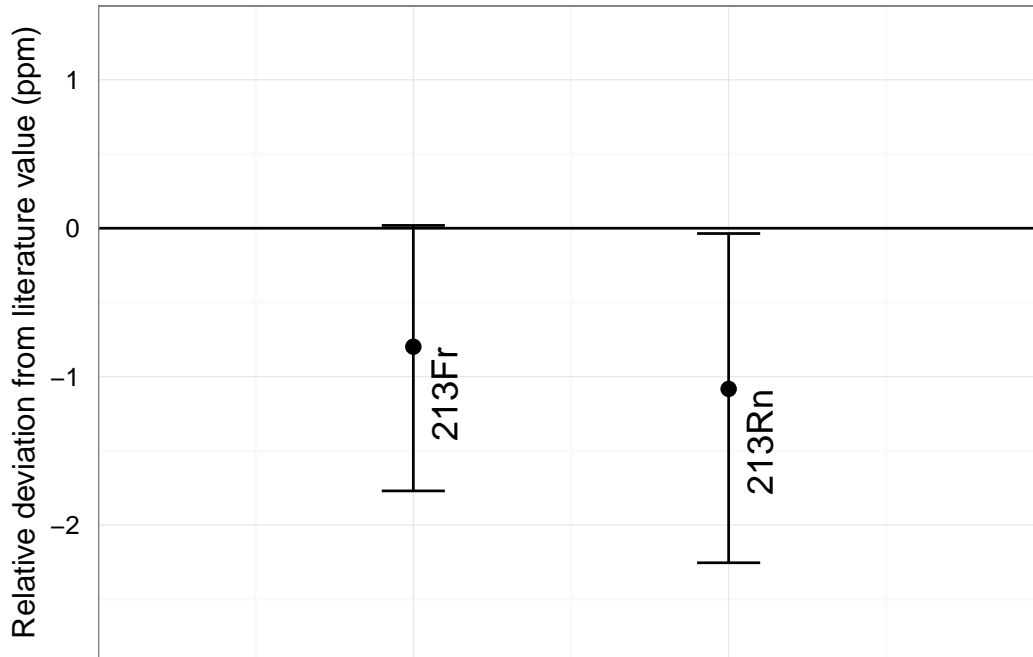
Figure 6.12.: Comparison of found mass values with literature values from AME 2012 [Wang et al., 2012].

6.4.3. Mass Values and Comparison to Literature

Result of the measurement are mass values for ^{213}Fr and ^{213}Rn. In order to obtain the neutral mass of the measured values, the mass of the electron has to be added again, resulting in the mass values with their error

	^{213}Fr	^{213}Rn
Mass (exp.)	$212.996016\,\mathrm{u} + 174 - 207\,\mu\mathrm{u}$	$212.993652\,\mathrm{u} + 223 - 249\,\mu\mathrm{u}$
ME (exp.)	$-3711 + 162 - 193\,\mathrm{keV}$	$-5913 + 208 - 232\,\mathrm{keV}$
ME (AME)	$-3553 \pm 5\,\mathrm{keV}$	$-5698 \pm 6\,\mathrm{keV}$

Figure 6.12 shows the relative deviation of the measured mass values to the AME 2012 values [Wang et al., 2012]. Relative deviations were calculated as

$$\mathrm{Dev_{rel}} = \frac{m_{\mathrm{exp}} - m_{\mathrm{AME}}}{m_{\mathrm{AME}}} \tag{6.9}$$

Errors of AME and the presented measurement were added quadratically.

The ^{213}Fr mass value is derived from direct mass measurement [Audi et al., 1982, Kowalska et al., 2009] as well as from α-spectroscopy [Valli et al., 1967, Hornshøj et al., 1974, Liu et al., 2005]. This measurement is in agreement with the AME

value. For ^{213}Rn, the mass in the AME 2012 is calculated with α-spectroscopy [Valli et al., 1970, Heßberger et al., 2000, Liu et al., 2005] exclusively, making this measurement the first direct mass measurement. Since α-spectroscopy carries the uncertainty of populating unknown isomeric states and therefore arriving at strongly deviating mass values, this measurement adds certainty to the previously known mass.

With a half-life of 19.5 ms, the measurement of ^{213}Rn shows the applicability of multiple-reflection time-of-flight mass spectrometry for heavy, very short-lived nuclides with present accuracies of $1.2 \cdot 10^{-6}$. Direct measurement of such short-lived, thermalized nuclides were not possible until now. It also demonstrates mass measurements with an MR-TOF-MS with differing turn numbers for the measured particles.

For future measurements, a reduction of the systematic uncertainties to $2 \cdot 10^{-7}$ [Ebert, 2016] is expected. In combination with operation at a mass resolving power of $400,000$ within 15 ms [Plaß et al., 2015] this will allow to measure masses of exotic nuclides with just 36 detected ions at accuracies of $3 \cdot 10^{-7}$.

7. Summary and Conclusions

The role of mass spectrometry in nuclear physics has been shown. A strong motivation exists to implement fast, efficient and universal methods for precision mass measurement and isobar separation; the latter is especially required at ISOL facilities. In this thesis, a new device for an ISOL facility was built and the first direct mass measurements performed with an MR-TOF-MS at an in-flight facility.

Based on the technology of an existing MR-TOF-MS, a novel isobar separator for TITAN at the ISOL facility ISAC at TRIUMF (Vancouver) has been designed, constructed and tested. First commissioning, both in Germany and in Canada, has been performed. A mass resolving power (FWHM) of about 47,000 for the mass spectrometry mode and about 14,000 for the isobar separation mode has been achieved. Already this result will extend the physics reach of TITAN. Doubling the kinetic energy to the design value as well as further optimization are expected to substantially increase the performance, surpassing a mass resolving power of 100,000 and a separation power of 50,000.

In the near future, the TITAN MR-TOF Isobar Separator will be included in the TITAN beamline and fully commissioned. There, it will provide isobar separation for TITAN, add additional capabilities to identify and quantify particles for beam diagnostics and beam development and perform direct mass measurements as a complementary method to the Penning trap. Envisioned experiments with contribution of the TITAN MR-TOF-MS include mass measurement of neutron-rich cadmium isotopes. These are relevant in order to locate the r-process nucleosynthesis paths.

In the second part of this thesis, direct mass measurements at the FRS Ion Catcher at GSI have been performed. Measured were the masses of ^{213}Fr and of ^{213}Rn, a nuclide with a half-life of 19.5 ms. For the latter, this was the first direct mass measurement. Mass accuracies of below $1.2 \cdot 10^{-6}$ were reached with just 27 events. This shows the excellent capabilities of MR-TOF-MS to measure very short lived, exotic nuclides at high accuracies.

Improvements in electronics and settings have already been realized and further progress is expected with application of the new data evaluation method. Relative mass accuracies of $3 \cdot 10^{-7}$ with less than 40 ions are in reach. With the gathered information, the design of the FAIR LEB instruments will be finalized and the instruments built.

A. Electrical Setup of the Instrument

Shown here is the electrical setup relevant for the ion optics of the TITAN MR-TOF-MS that was used in the commissioning of the instrument.
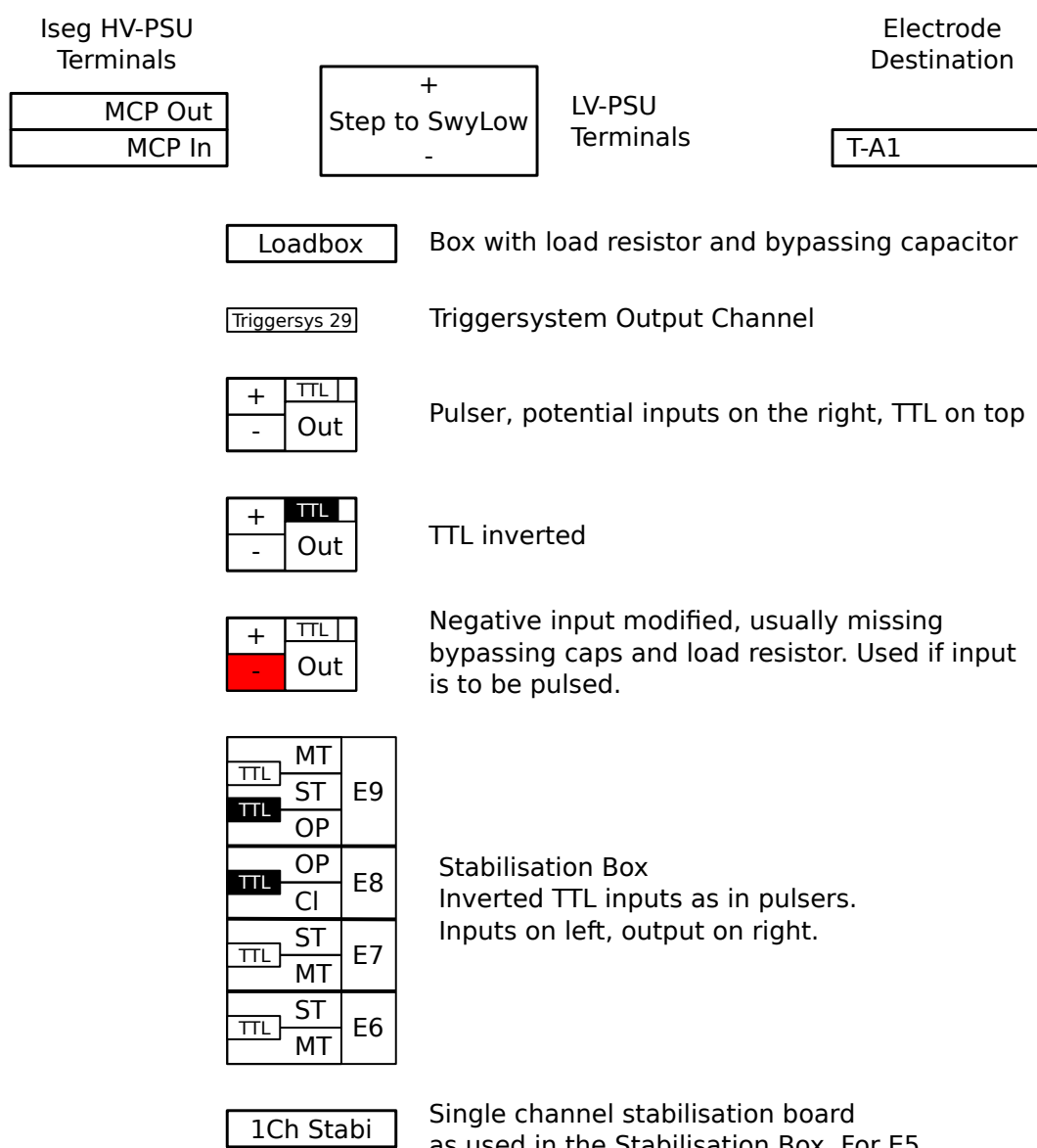

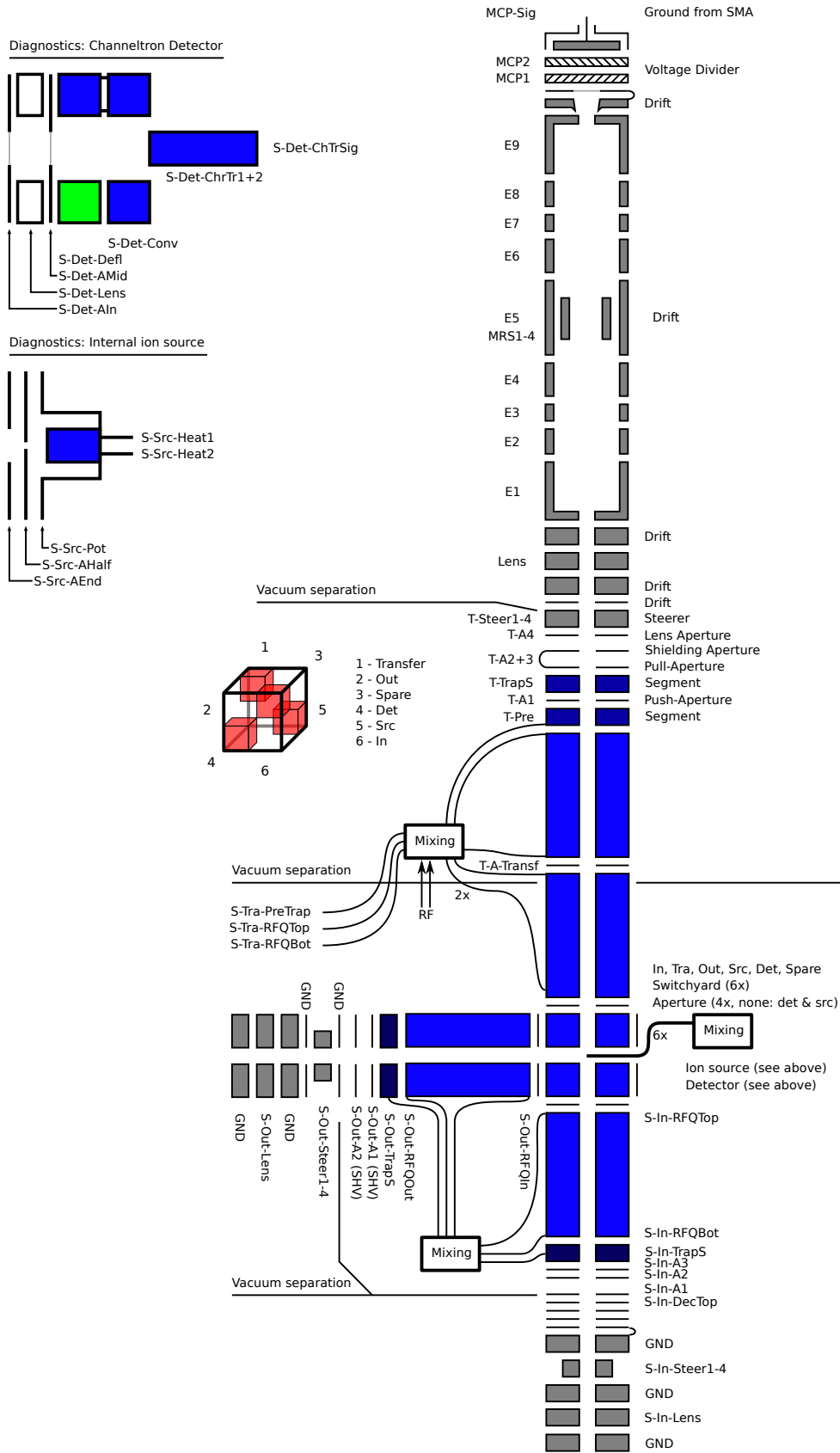Figure A.1.: Key for the cabling diagrams.

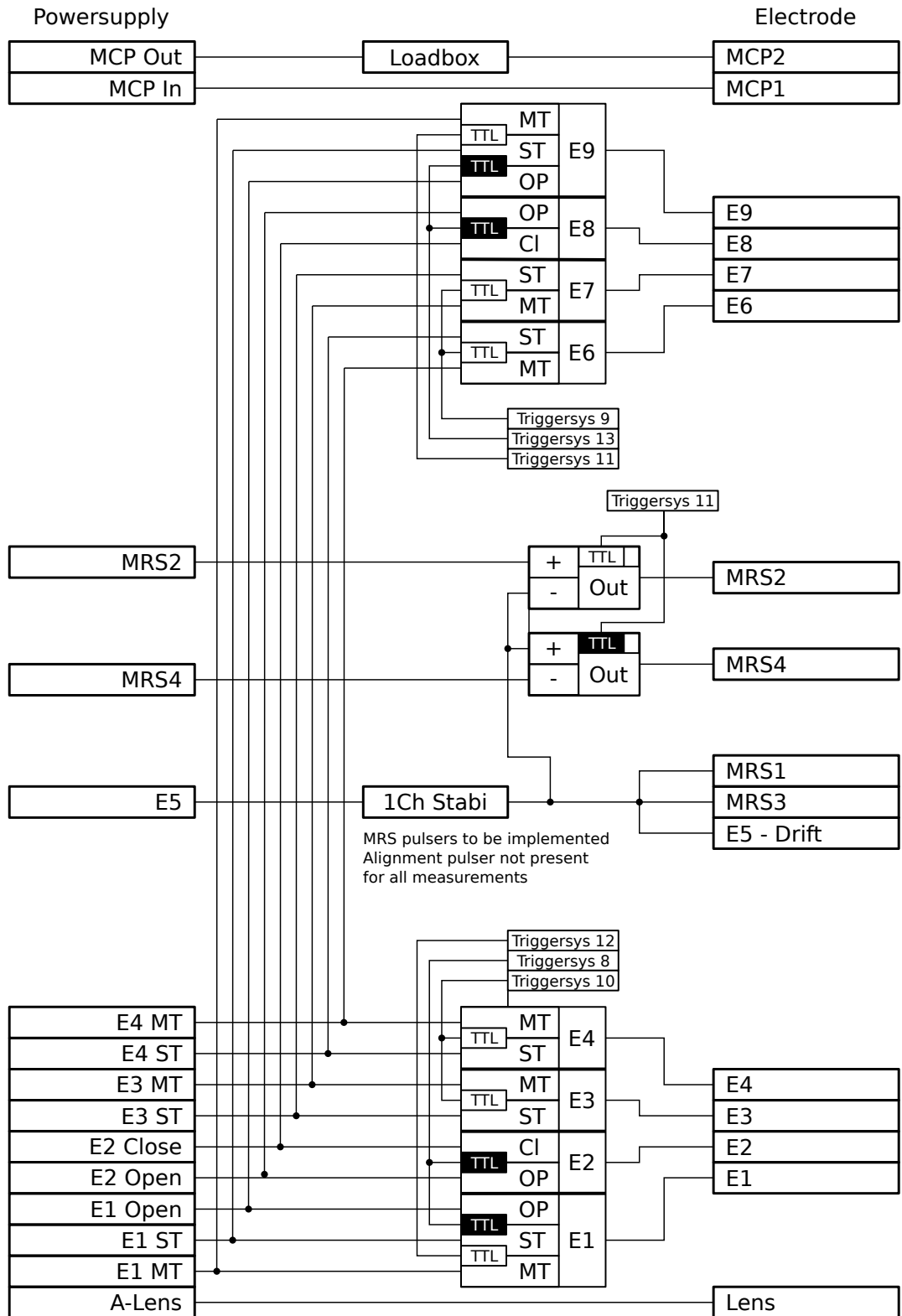Figure A.2.: Schematic of the electrodes including their names.

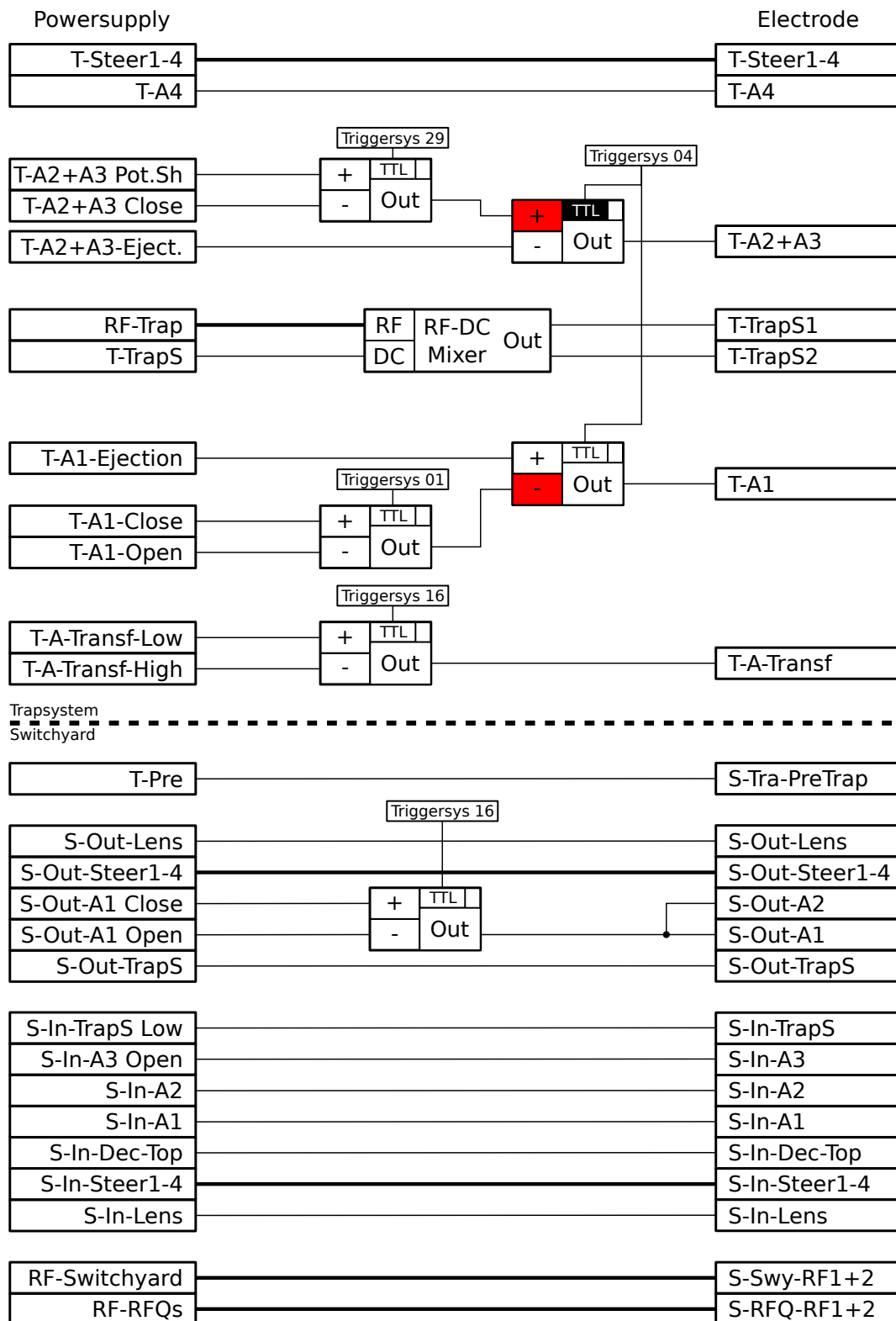Figure A.3.: Airside cabling of the analyzer.

Figure A.4.: Airside cabling of the trap system and part of the switchyard.
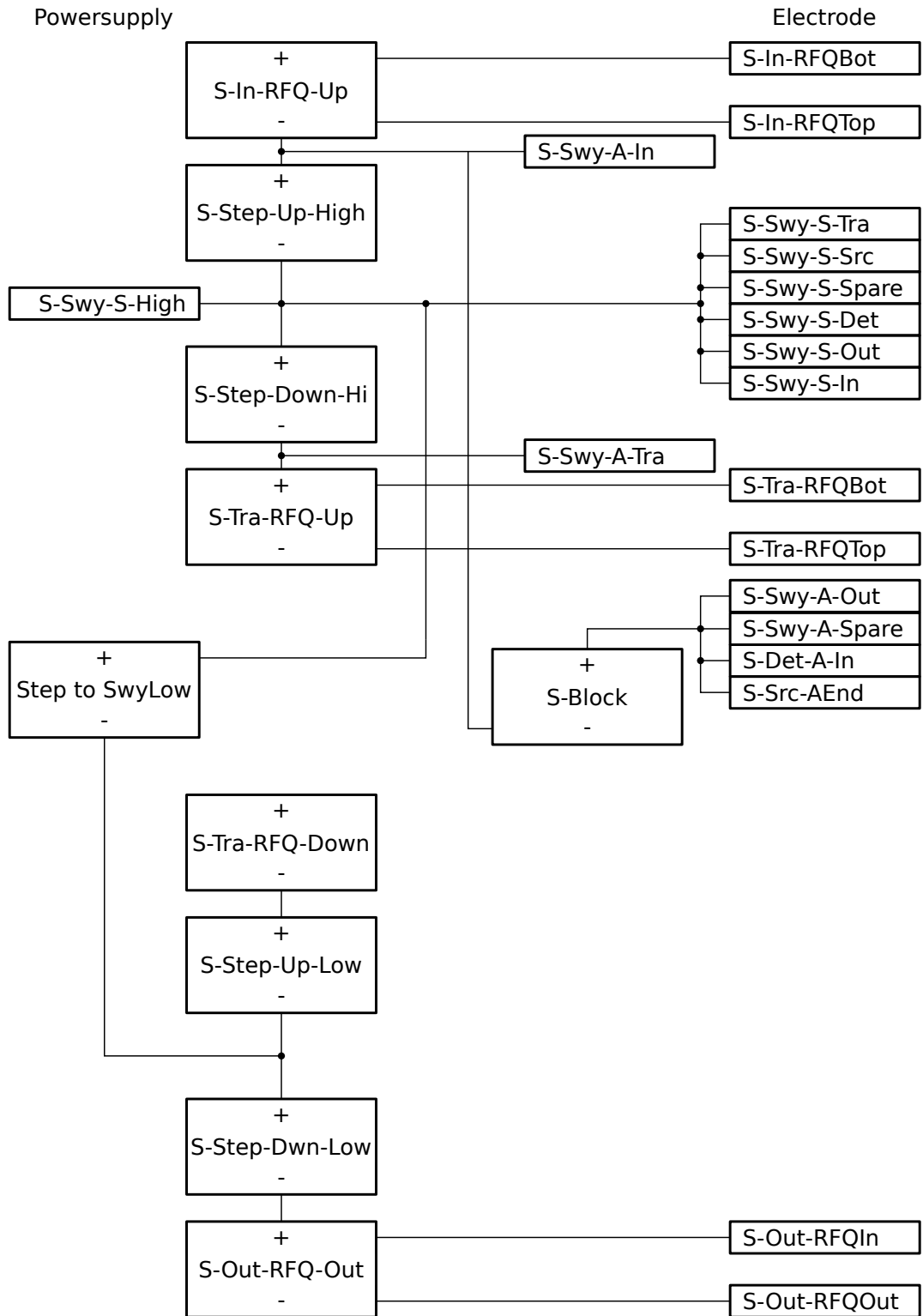
Figure A.5.: Airside cabling of part of the switchyard.

Bibliography

[Aldrich, 1997] Aldrich, J. (1997). R.A. Fisher and the making of maximum likelihood 1912-1922. *Stat. Sci.*, 12(3):162–176.

[Aston, 1922] Aston, F. (1922). Mass spectra and isotopes. Nobel lecture.

[Aston, 1920] Aston, F. W. (1920). The mass-spectra of chemical elements. *Philos. Mag.*, 39(233):611–625.

[Audi, 2006] Audi, G. (2006). The history of nuclidic masses and of their evaluation. *Int.. J. Mass Spectrom.*, 251(2–3):85 – 94.

[Audi et al., 1982] Audi, G., Epherre, M., Thibault, C., Wapstra, A., and Bos, K. (1982). Masses of rb, cs and fr isotopes. *Nucl. Phys. A*, 378(3):443–460.

[Audi et al., 2012] Audi, G., Kondev, F. G., Wang, M., Pfeiffer, B., Sun, X., Blachot, J., and MacCormick, M. (2012). The NUBASE2012 evaluation of nuclear properties. *Chin. Phys. C*, 36(12):1157.

[Ayet, 2015] Ayet, S. (2015). Personal communication.

[Bender et al., 2003] Bender, M., Heenen, P.-H., and Reinhard, P.-G. (2003). Self-consistent mean-field models for nuclear structure. *Rev. Mod. Phys.*, 75(1):121.

[Blaum, 2006] Blaum, K. (2006). High-accuracy mass spectrometry with stored ions. *Phys. Rep.*, 425(1):1 – 78.

[Bollen, 2001] Bollen, G. (2001). Mass measurements of short-lived nuclides with ion traps. *Nucl. Phys. A*, 693(1–2):3 – 18.

[Bollen et al., 1996] Bollen, G., Becker, S., Kluge, H. J., König, M., Moore, R. B., Otto, T., Raimbault-Hartmann, H., Savard, G., Schweikhard, L., and Stolzenberg, H. (1996). ISOLTRAP: A tandem Penning trap system for accurate on-line mass determination of short-lived isotopes. *Nucl. Instrum. Methods Phys. Res., Sect. A*, 368(3):675 – 697.

[Bosch, 2003] Bosch, F. (2003). Schottky mass-and lifetime-spectrometry of unstable, stored ions. *J. Phys. B*, 36(3):585.

[Bradbury and Nielsen, 1936] Bradbury, N. E. and Nielsen, R. A. (1936). Absolute values of the electron mobility in hydrogen. *Phys. Rev.*, 49:388–393.

[Bricault et al., 1997] Bricault, P., Dombsky, M., Schmor, P., and Stanford, G. (1997). Radioactive ion beams facility at TRIUMF. *Nucl. Instrum. Methods Phys. Res., Sect. B*, 126(1–4):231 – 235. International Conference on Electromagnetic Isotope Separators and Techniques Related to Their Applications.

[Bricault et al., 2014] Bricault, P. G., Ames, F., Dombsky, M., Kunz, P., and Lassen, J. (2014). Rare isotope beams at ISAC – Target and ion source systems. *Hyperfine Interact.*, 225(1-3):25–49.

[Brunner et al., 2012] Brunner, T., Smith, M., Brodeur, M., Ettenauer, S., Gallant, A., Simon, V., Chaudhuri, A., et al. (2012). TITAN's digital RFQ ion beam cooler and buncher, operation and performance. *Nucl. Instrum. Methods Phys. Res., Sect. A*, 676:32 – 43.

[Burbidge et al., 1957] Burbidge, E. M., Burbidge, G. R., Fowler, W. A., and Hoyle, F. (1957). Synthesis of the elements in stars. *Rev. Mod. Phys.*, 29(4):547.

[Chadwick, 1932] Chadwick, J. (1932). Possible existence of a neutron. *Nature*, 129(3252):312.

[Dawson, 1976] Dawson, P. (1976). *Quadrupole Mass Spectrometry and its applications*. Elsevier.

[Dehmelt, 1967] Dehmelt, H. G. (1967). Radiofrequency spectroscopy of stored ions I: Storage. *Adv. Atom. Mol. Phys.*, 3(53).

[Dickel, 2010] Dickel, T. (2010). *Design and Commissioning of an Ultra-High-Resolution Time-of-Flight Based Isobar Separator and Mass Spectrometer*. PhD thesis, Justus-Liebig-Universtität Gießen.

[Dickel, 2016] Dickel, T. (2016). Personal Communication.

[Dickel et al., 2013] Dickel, T., Plaß, W., Lang, J., Ebert, J., Geissel, H., Haettner, E., Jesch, C., Lippert, W., Petrick, M., Scheidenberger, C., and Yavor, M. (2013). Multiple-reflection time-of-flight mass spectrometry for in situ applications. *Nucl. Instrum. Methods Phys. Res., Sect. B*, 317, Part B:779 – 784. {XVIth} International Conference on ElectroMagnetic Isotope Separators and Techniques Related to their Applications, December 2–7, 2012 at Matsue, Japan.

[Dickel et al., 2015] Dickel, T., Plaß, W., Becker, A., Czok, U., Geissel, H., Haettner, E., Jesch, C., Kinsel, W., Petrick, M., Scheidenberger, C., et al. (2015). A high-performance multiple-reflection time-of-flight mass spectrometer and

isobar separator for the research with exotic nuclei. *Nucl. Instrum. Methods Phys. Res., Sect. A*, 777:172–188.

[Dilling et al., 2003] Dilling, J., Bricault, P., Smith, M., and Kluge, H.-J. (2003). The proposed TITAN facility at ISAC for very precise mass measurements on highly charged short-lived isotopes. *Nucl. Instrum. Methods Phys. Res., Sect. B*, 204(0):492 – 496. 14th International Conference on Electromagnetic Isotope Separators and Techniques Related to their Applications.

[Dilling et al., 2014a] Dilling, J., Krücken, R., and Merminga, L. (2014a). ARIEL overview. In *ISAC and ARIEL: The TRIUMF Radioactive Beam Facilities and the Scientific Program*, pages 253–262. Springer.

[Dilling et al., 2014b] Dilling, J., Krücken, R., and Merminga, L. (2014b). *ISAC and ARIEL: The TRIUMF Radioactive Beam Facilities and the Scientific Program*. Springer.

[Diwisch, 2015] Diwisch, M. (2015). *Present and Future Isochronous Mass Spectrometry at GSI-FAIR*. PhD thesis, Justus-Liebig-Universtität Gießen.

[Dodonov et al., 1997] Dodonov, A., Kozlovsky, V., Loboda, A., Raznikov, V., Sulimenkov, I., Tolmachev, A., Kraft, A., and Wollnik, H. (1997). A new technique for decomposition of selected ions in molecule ion reactor coupled with ortho-time-of-flight mass spectrometry. *Rapid Commun. Mass Spectrom.*, 11(15):1649–1656.

[Douglas et al., 2005] Douglas, D., Frank, A., and Mao, D. (2005). Linear ion traps in mass spectrometry. *Mass Spectrom. Rev.*, 24(1):1–29.

[Douglas and Konenkov, 2002] Douglas, D. and Konenkov, N. (2002). Influence of the 6th and 10th spatial harmonics on the peak shape of a quadrupole mass filter with round rods. *Rapid Commun. Mass Spectrom.*, 16:1425.

[Ebert, 2016] Ebert, J. (2016). *Thesis in preparation*. PhD thesis, Justus-Liebig-Universtität Gießen.

[Eddington, 1920] Eddington, A. S. (1920). The internal constitution of the stars. *The Scientific Monthly*, pages 297–303.

[ETP electron multipliers, 2006] ETP electron multipliers (2006). MagneTOF product data. http://www.sge.com/root/pdfs_local/product_data_sheets/pd-0257-a.pdf.

[Fisher et al., 1912] Fisher, R. et al. (1912). On an absolute criterion for fitting frequency curves. *Stat. Sci.*

[Foley and Dorsey, 1984] Foley, J. P. and Dorsey, J. G. (1984). A review of the

exponentially modified gaussian EMG function: evaluation and subsequent calculation of universal data. *J. Chromatogr. Sci.*, 22(1):40–46.

[FRS Group at GSI, 2016] FRS Group at GSI (2016). Schematic of SIS, FRS and ESR. `https://www.gsi.de/work/forschung/nustarenna/nustarenna_divisions/frs_super_frs.htm`.

[Fulton, 2011] Fulton, B. (2011). Present and future RIB facilities. *J. Phys. Conf. S.*, 312(5):052001.

[Gallant et al., 2010] Gallant, A., Brodeur, M., Brunner, T., Ettenauer, S., Good, M., Lapierre, A., Ringle, R., Simon, V., Delheij, P., and Dilling, J. (2010). TITAN-EBIT — Charge breeding of radioactive isotopes for high precision mass measurements. *J. Inst.*, 5(08):C08009.

[Geissel et al., 1992] Geissel, H., Armbruster, P., Behr, K., Brünle, A., Burkard, K., Chen, M., Folger, H., Franczak, B., Keller, H., Klepper, O., Langenbeck, B., Nickel, F., Pfeng, E., Pfützner, M., Roeckl, E., Rykaczewski, K., Schall, I., Schardt, D., Scheidenberger, C., Schmidt, K.-H., Schröter, A., Schwab, T., Sümmerer, K., Weber, M., Münzenberg, G., Brohm, T., Clerc, H.-G., Fauerbach, M., Gaimard, J.-J., Grewe, A., Hanelt, E., Knödler, B., Steiner, M., Voss, B., Weckenmann, J., Ziegler, C., Magel, A., Wollnik, H., Dufour, J., Fujita, Y., Vieira, D., and Sherrill, B. (1992). The GSI projectile fragment separator (FRS): A versatile magnetic system for relativistic heavy ions. *Nucl. Instrum. Methods Phys. Res., Sect. B*, 70(1):286 – 297.

[Geissel et al., 2003] Geissel, H., Weick, H., Winkler, M., Münzenberg, G., Chichkine, V., Yavor, M., Aumann, T., Behr, K. H., Böhmer, M., Brünle, A., Burkard, K., Benlliure, J., Cortina-Gil, D., Chulkov, L., Dael, A., Ducret, J. E., Emling, H., Franczak, B., Friese, J., Gastineau, B., Gerl, J., Gernhäuser, R., Hellström, M., Jonson, B., Kojouharova, J., Kulessa, R., Kindler, B., Kurz, N., Lommel, B., Mittig, W., Moritz, G., Mühle, C., Nolen, J. A., Nyman, G., Roussell-Chomaz, P., Scheidenberger, C., Schmidt, K. H., Schrieder, G., Sherrill, B. M., Simon, H., Sümmerer, K., Tahir, N. A., Vysotsky, V., Wollnik, H., and Zeller, A. F. (2003). The Super-FRS project at GSI. *Nucl. Instrum. Methods Phys. Res., Sect. B*, 204:71 – 85. 14th International Conference on Electromagnetic Isotope Separators and Techniques Related to their Applications.

[Gibson and Taylor, 2001] Gibson, J. and Taylor, S. (2001). Numerical investigation of the effect of electrode size on the behaviour of quadrupole mass filters. *Rapid Commun. Mass Spectrom.*, 15:1960.

[Greiner, 2013] Greiner, F. (2013). Aufbau und Inbetriebnahme einer RF-Quadrupol-Strahlweiche. Bachelor's thesis, Justus-Liebig-Universität Giessen.

[Greiner, 2015] Greiner, F. (2015). Personal Communication.

[Haettner, 2012] Haettner, E. (2012). Personal communication.

[HeatWave Labs, 2002] HeatWave Labs (2002). TB 108 specification. `http://www.cathode.com/pdf/tb-118.pdf`.

[Heßberger et al., 2000] Heßberger, F., Hofmann, S., Ackermann, D., Ninov, V., Leino, M., Saro, S., Andreyev, A., Lavrentev, A., Popeko, A., and Yeremin, A. (2000). Decay properties of neutron-deficient nuclei in the region z= 86–92. *Eur. Phys. J. A*, 8(4):521–535.

[Hofmann and Münzenberg, 2000] Hofmann, S. and Münzenberg, G. (2000). The discovery of the heaviest elements. *Rev. Mod. Phys.*, 72(3):733.

[Hornshøj et al., 1974] Hornshøj, P., Hansen, P., and Jonson, B. (1974). Alpha-decay widths of neutron-deficient francium and astatine isotopes. *Nucl. Phys. A*, 230(3):380–392.

[Itano et al., 1995] Itano, W., Bergquist, J., Bollinger, J., and Wineland, D. (1995). Cooling methods in ion traps. *Phys. Scripta*, 1995(T59):106.

[Javahery and Thomson, 1997] Javahery, G. and Thomson, B. (1997). A segmented radiofrequency-only quadrupole collision cell for measurements of ion collision cross section on a triple quadrupole mass spectrometer. *J. Am. Soc. Mass. Spectrom.*, 8(7):697–702.

[Konradi, 2013] Konradi, M. (2013). Personal communication.

[Kowalska et al., 2009] Kowalska, M., Naimi, S., Agramunt, J., Algora, A., Audi, G., Beck, D., Blank, B., Blaum, K., Böhm, C., Breitenfeldt, M., Estevez, E., Fraile, L. M., George, S., Herfurth, F., Herlert, A., Kellerbauer, A., Lunney, D., Minaya-Ramirez, E., Neidherr, D., Olaizola, B., Riisager, K., Rosenbusch, M., Rubio, B., Schwarz, S., Schweikhard, L., and Warring, U. (2009). Preparing a journey to the east of 208Pb with ISOLTRAP: Isobaric purification at a = 209 and new masses for 211-213fr and 211ra. *Eur. Phys. J. A*, 42(3):351–359.

[Kugler et al., 1992] Kugler, E., Fiander, D., Johnson, B., Haas, H., Przewloka, A., Ravn, H., Simon, D., and Zimmer, K. (1992). The new cern-isolde on-line mass-separator facility at the ps-booster. *Nucl. Instrum. Methods Phys. Res., Sect. B*, 70(1):41 – 49.

[Lang, 2016] Lang, J. (2016). *Thesis in preparation*. PhD thesis, Justus-Liebig-Universtität Gießen.

[Liu et al., 2005] Liu, Z., Kurcewicz, J., Woods, P., Mazzocchi, C., Attallah, F., Badura, E., Davids, C., Davinson, T., Döring, J., Geissel, H., et al. (2005). Decay spectroscopy of suburanium isotopes following projectile fragmentation of 238 u at 1gev/u. *Nucl. Instr. Meth. A*, 543(2):591–601.

119

Bibliography

[Loboda et al., 2000] Loboda, A., Krutchinsky, O., and Loboda, O. (2000). Novel linac II electrode geometry for creating an axial field in a multipole ion guide. *Eur. J. Mass Spectrom.*, 6:531.

[Lunney et al., 2003] Lunney, D., Pearson, J., and Thibault, C. (2003). Recent trends in the determination of nuclear masses. *Rev. Mod. Phys.*, 75(3):1021.

[Mamyrin et al., 1973] Mamyrin, B., Karataev, V., Shmikk, D., and Zagulin, V. (1973). The mass-reflectron, a new nonmagnetic time-of-flight mass spectrometer with high resolution. *Zh. Eksp. Teor. Fiz*, 64:82–89.

[Mané et al., 2011] Mané, E., Behr, J., Billowes, J., Brunner, T., Brodeur, M., Buchinger, F., Crawford, J., Dilling, J., Ettenauer, S., Levy, C., Voss, A., and Pearson, M. (2011). Collinear laser spectroscopy with reverse-extracted bunched beams at TRIUMF. *Hyperfine Interact.*, 199(1-3):357–363.

[Mansoori et al., 1998] Mansoori, B., Dyer, E., Lock, C., Bateman, K., Boyd, R., and Thomson, B. (1998). Analytical performance of a high-pressure radio frequency-only quadrupole collision cell with an axial field applied by using conical rods. *J. Am. Soc. Mass. Spectrom.*, 9(8):775–788.

[Marsh, 2014] Marsh, B. (2014). Resonance ionization laser ion sources for on-line isotope separators. *Rev. Sci. Instrum.*, 85(2).

[Marshall et al., 1998] Marshall, A., Hendrickson, C., and Jackson, G. (1998). Fourier transform ion cyclotron resonance mass spectrometry: A primer. *Mass Spectrom. Rev.*, 17(1):1–35.

[Möller et al., 1988] Möller, P., Myers, W., Swiatecki, W., and Treiner, J. (1988). Nuclear mass formula with a finite-range droplet model and a folded-Yukawa single-particle potential. *At. Data Nucl. Data Tables*, 39(2):225–233.

[Moriwaki et al., 1992] Moriwaki, Y., Tachikawa, M., Maeno, Y., and Shimizu, T. (1992). Collision cooling of ions stored in quadrupole radio-frequency trap. *Jpn. J. Appl. Phys.*, 31(11B):L1640.

[Neumayr et al., 2006] Neumayr, J., Beck, L., Habs, D., Heinz, S., Szerypo, J., Thirolf, P., Varentsov, V., Voit, F., Ackermann, D., Beck, D., Block, M., Di, Z., Eliseev, S., Geissel, H., Herfurth, F., Heßberger, F., Hofmann, S., Kluge, H.-J., Mukherjee, M., Münzenberg, G., Petrick, M., Quint, W., Rahaman, S., Rauth, C., Rodríguez, D., Scheidenberger, C., Sikler, G., Wang, Z., Weber, C., Plaß, W., Breitenfeldt, M., Chaudhuri, A., Marx, G., Schweikhard, L., Dodonov, A., Novikov, Y., and Suhonen, M. (2006). The ion-catcher device for SHIPTRAP. *Nucl. Instrum. Methods Phys. Res., Sect. B*, 244(2):489 – 500.

[NI-6602, 2016] NI-6602 (2016). NI 6602 PCI specifications. `http://sine.ni.com/nips/cds/view/p/lang/en/nid/1123`.

[OriginLab, 2016] OriginLab (2016). Origin. `http://www.originlab.de/index.aspx?go=PRODUCTS/OriginPro`.

[Pearson, 2007] Pearson, J. (2007). Nuclear mass models. `http://www.jinaweb.org/events/argonne07/lectures/pearson_MassSchool.pdf`. JINA Special School.

[Plaß, 2001] Plaß, W. (2001). *The Dependence of RF Ion Trap Mass Spectrometer Performance on Electrode Geometry and Collisional Processes*. PhD thesis, Justus-Liebig-Universtität Gießen.

[Plaß et al., 2008] Plaß, W., Dickel, T., Czok, U., Geissel, H., Petrick, M., Reinheimer, K., Scheidenberger, C., and I.Yavor, M. (2008). Isobar separation by time-of-flight mass spectrometry for low-energy radioactive ion beam facilities. *Nucl. Instrum. Methods Phys. Res., Sect. B*, 266(19-20):4560 – 4564. Proceedings of the XVth International Conference on Electromagnetic Isotope Separators and Techniques Related to their Applications.

[Plaß et al., 2013] Plaß, W., Dickel, T., and Scheidenberger, C. (2013). Multiple-reflection time-of-flight mass spectrometry. *Int. J. Mass spectrom.*, 349–350:134 – 144. 100 years of Mass Spectrometry.

[Plaß et al., 2015] Plaß, W. R., Dickel, T., Andres, S. A. S., Ebert, J., Greiner, F., Hornung, C., Jesch, C., Lang, J., Lippert, W., Majoros, T., Short, D., Geissel, H., Haettner, E., Reiter, M. P., Rink, A.-K., Scheidenberger, C., and Yavor, M. I. (2015). High-performance multiple-reflection time-of-flight mass spectrometers for research with exotic nuclei and for analytical mass spectrometry. *Phys. Scripta*, 2015(T166):014069.

[Plaß et al., 2007] Plaß, W., Dickel, T., Petrick, M., Boutin, D., Di, Z., Fleckenstein, T., Geissel, H., Jesch, C., Scheidenberger, C., and Wang, Z. (2007). An RF quadrupole–time-of-flight system for isobar-separation and multiplexed low-energy rare-isotope beam experiments. *Eur. Phys. J. Special Topics*, 150(1):367–368.

[Plaß et al., 2013] Plaß, W., Dickel, T., Purushothaman, S., Dendooven, P., Geissel, H., Ebert, J., Haettner, E., Jesch, C., Ranjan, M., Reiter, M., et al. (2013). The FRS ion catcher – A facility for high-precision experiments with stopped projectile and fission fragments. *Nuclear Instruments and Methods in Physics Research Section B: Beam Interactions with Materials and Atoms*, 317:457–462.

[Purushothaman, 2015] Purushothaman, S. (2015). Personal communication.

[Purushothaman et al., 2016] Purushothaman, S. et al. (2016). Manuscript in preparation.

[Purushothaman et al., 2013] Purushothaman, S., Reiter, M. P., Haettner, E.,

Dendooven, P., Dickel, T., Geissel, H., Ebert, J., Jesch, C., Plass, W. R., Ranjan, M., Weick, H., Amjad, F., Ayet, S., Diwisch, M., Estrade, A., Farinon, F., Greiner, F., Kalantar-Nayestanaki, N., Knöbel, R., Kurcewicz, J., Lang, J., Moore, I. D., Mukha, I., Nociforo, C., Petrick, M., Pfützner, M., Pietri, S., Prochazka, A., Rink, A.-K., Rinta-Antila, S., Scheidenberger, C., Takechi, M., Tanaka, Y. K., Winfield, J. S., and Yavor, M. I. (2013). First experimental results of a cryogenic stopping cell with short-lived, heavy uranium fragments produced at 1000 mev/u. *Europhys. Lett.*, 104(4):42001.

[R Core Team, 2015] R Core Team (2015). *R: A Language and Environment for Statistical Computing*. R Foundation for Statistical Computing, Vienna, Austria.

[Ranjan et al., 2011] Ranjan, M., Purushothaman, S., Dickel, T., Geissel, H., Plass, W. R., Schäfer, D., Scheidenberger, C., de Walle, J. V., Weick, H., and Dendooven, P. (2011). New stopping cell capabilities: Rf carpet performance at high gas density and cryogenic operation. *Europhys. Lett.*, 96(5):52001.

[Reiter, 2011] Reiter, M. (2011). Simulation der kryogenen stoppzelle des frs-ion-catchers-experiments und aufbau eines neuartigen frq-strahlführungssystems. Master's thesis, Justus-Liebig-Universität Giessen.

[Reiter, 2013] Reiter, M. (2013). Personal communication.

[Rodríguez et al., 2010] Rodríguez, D., Blaum, K., Nörtershäuser, W., Ahammed, M., Algora, A., Audi, G., Äystö, J., Beck, D., Bender, M., Billowes, J., Block, M., Böhm, C., Bollen, G., Brodeur, M., Brunner, T., Bushaw, B., Cakirli, R., Campbell, P., Cano-Ott, D., Cortés, G., Crespo López-Urrutia, J., Das, P., Dax, A., De, A., Delheij, P., Dickel, T., Dilling, J., Eberhardt, K., Eliseev, S., Ettenauer, S., Flanagan, K., Ferrer, R., García-Ramos, J.-E., Gartzke, E., Geissel, H., George, S., Geppert, C., Gómez-Hornillos, M., Gusev, Y., Habs, D., Heenen, P.-H., Heinz, S., Herfurth, F., Herlert, A., Hobein, M., Huber, G., Huyse, M., Jesch, C., Jokinen, A., Kester, O., Ketelaer, J., Kolhinen, V., Koudriavtsev, I., Kowalska, M., Krämer, J., Kreim, S., Krieger, A., Kühl, T., Lallena, A., Lapierre, A., Le Blanc, F., Litvinov, Y., Lunney, D., Martínez, T., Marx, G., Matos, M., Minaya-Ramirez, E., Moore, I., Nagy, S., Naimi, S., Neidherr, D., Nesterenko, D., Neyens, G., Novikov, Y., Petrick, M., Plaß, W., Popov, A., Quint, W., Ray, A., Reinhard, P.-G., Repp, J., Roux, C., Rubio, B., Sánchez, R., Schabinger, B., Scheidenberger, C., Schneider, D., Schuch, R., Schwarz, S., Schweikhard, L., Seliverstov, M., Solders, A., Suhonen, M., Szerypo, J., Taín, J., Thirolf, P., Ullrich, J., Van Duppen, P., Vasiliev, A., Vorobjev, G., Weber, C., Wendt, K., Winkler, M., Yordanov, D., and Ziegler, F. (2010). MATS and LaSpec: High-precision experiments using ion traps and lasers at FAIR. *Eur. Phys. J. Special Topics*, 183(1):1–123.

[Savard et al., 2003] Savard, G., Clark, J., Boudreau, C., Buchinger, F., Crawford, J., Geissel, H., Greene, J., Gulick, S., Heinz, A., Lee, J., Levand, A.,

Maier, M., Münzenberg, G., Scheidenberger, C., Seweryniak, D., Sharma, K., Sprouse, G., Vaz, J., Wang, J., Zabransky, B., and Zhou, Z. (2003). Development and operation of gas catchers to thermalize fusion–evaporation and fragmentation products. *Nucl. Instrum. Methods Phys. Res., Sect. B*, 204:582 – 586. 14th International Conference on Electromagnetic Isotope Separators and Techniques Related to their Applications.

[Schmidt et al., 2002] Schmidt, K., Benlliure, J., Enqvist, T., Junghans, A., Rejmund, F., and Ricciardi, M. (2002). Future prospects for secondary-beam production. *Nucl. Phys. A*, 701(1–4):115 – 122. 5th International Conference on Radioactive Nuclear Beams.

[Simon, 2008] Simon, A. (2008). Entwicklung und Test eines CFK-basierten RF-Quadrupols für ein Multireflektions-Flugzeitmassenspektrometer. Bachelor's thesis, Justus-Liebig-Universität Gießen.

[Simon et al., 2011] Simon, V., Delheij, P., Dilling, J., Ke, Z., Shi, W., and Gwinner, G. (2011). Cooling of short-lived, radioactive, highly charged ions with the TITAN cooler Penning trap. *Hyperfine Interact.*, 199(1-3):151–159.

[Takamine et al., 2007] Takamine, A., Wada, M., Nakamura, T., Okada, K., Yamazaki, Y., Kanai, Y., Kojima, T. M., Yoshida, a., Kubo, T., Noda, K., Katayama, I., Lioubimov, V., and Schuessler, H. (2007). Improvement of slow RI beam transport using carbon-OPIG. *RIKEN Accel. Prog. Rep.*, 40:147.

[Taylor, 1982] Taylor, J. R. (1982). *An Introduction to Error Analysis: The Study of Uncertainties in Physical Measurements*. Univ. Sci. Books, Mill Valley, Calif.

[Thomson and Jolliffe, 1998] Thomson, B. and Jolliffe, C. (1998). Spectrometer with axial field. US Patent 5,847,386.

[Tolmachev, 1997] Tolmachev, A. (1997). A collisional focusing ion guide for coupling an atmospheric pressure ion source to a mass spectrometer. *Nucl. Instrum. Methods Phys. Res., Sect. B*, 124:112–119.

[TRIUMF, 2016] TRIUMF (2016). Schematic of the ISAC facility. `http://www.triumf.ca/research-program/research-facilities/isac-facilities`.

[Valli et al., 1967] Valli, K., Hyde, E., and Treytl, W. (1967). Alpha decay of neutron-deficient francium isotopes. *J. Inorg. Nucl. Chem.*, 29(10):2503–2514.

[Valli et al., 1970] Valli, K., Hyde, E. K., and Borggreen, J. (1970). Production and decay properties of thorium isotopes of mass 221-224 formed in heavy-ion reactions. *Phys. Rev. C*, 1(6):2115.

[Wada, 2013] Wada, M. (2013). Genealogy of gas cells for low-energy RI-beam production. *Nucl. Instrum. Methods Phys. Res., Sect. B*, 317, Part B:450 –

456. {XVIth} International Conference on ElectroMagnetic Isotope Separators and Techniques Related to their Applications, December 2–7, 2012 at Matsue, Japan.

[Wada et al., 2003] Wada, M., Ishida, Y., Nakamura, T., Yamazaki, Y., Kambara, T., Ohyama, H., Kanai, Y., Kojima, T., Nakai, Y., Ohshima, N., Yoshida, A., Kubo, T., Matsuo, Y., Fukuyama, Y., Okada, K., Sonoda, T., Ohtani, S., Noda, K., Kawakami, H., and Katayama, I. (2003). Slow RI-beams from projectile fragment separators. *Nucl. Instrum. Methods Phys. Res., Sect. B*, 204:570 – 581. 14th International Conference on Electromagnetic Isotope Separators and Techniques Related to their Applications.

[Wallerstein et al., 1997] Wallerstein, G., Iben, I., Parker, P., Boesgaard, A., Hale, G., Champagne, A., Barnes, C., Käppeler, F., Smith, V., Hoffman, R., et al. (1997). Synthesis of the elements in stars: Forty years of progress. *Rev. Mod. Phys.*, 69(4):995.

[Wang et al., 2012] Wang, M., Audi, G., Wapstra, A. H., Kondev, F., MacCormick, M., Xu, X., and Pfeiffer, B. (2012). The AME2012 atomic mass evaluation. *Chin. Phys. C*, 36(12):1603.

[WaveMetrics Inc., 2015] WaveMetrics Inc. (2015). IGOR Pro. `https://www.wavemetrics.com/products/igorpro/igorpro.htm`.

[Weizsäcker, 1935] Weizsäcker, C. v. (1935). Zur Theorie der Kernmassen. *Z. Phys. A: Hadrons Nucl.*, 96(7):431–458.

[Wiley and McLaren, 1955] Wiley, W. and McLaren, I. (1955). Time-of-flight mass spectrometer with improved resolution. *Rev. Sci. Instrum.*, 26(12):1150–1157.

[Wollnik, 1987] Wollnik, H. (1987). *Optics of charged particles.* Elsevier.

[Wollnik and Berz, 1985] Wollnik, H. and Berz, M. (1985). Relations between elements of transfer matrices due to the condition of symplecticity. *Nucl. Instrum. Methods Phys. Res., Sect. A*, 238(1):127 – 140.

[Yavor, 2009] Yavor, M. (2009). *Optics of charged particle analyzers.* Academic Press.

[Yavor, 2011] Yavor, M. (2011). Simulation of retrapping. Internal Report.

[Yavor et al., 2015] Yavor, M., Plaß, W., Dickel, T., Geissel, H., and Scheidenberger, C. (2015). Ion-optical design of a high-performance multiple-reflection time-of-flight mass spectrometer and isobar separator. *Int. J. Mass Spectrom.*, 381–382:1 – 9.

Acknowledgment

Versicherung

Ich erkläre: Ich habe die vorgelegte Dissertation selbständig und ohne unerlaubte fremde Hilfe und nur mit den Hilfen angefertigt, die ich in der Dissertation angegeben habe.

Alle Textstellen, die wörtlich oder sinngemäß aus veröffentlichten Schriften entnommen sind, und alle Angaben, die auf mündlichen Auskünften beruhen, sind als solche kenntlich gemacht. Ich stimme einer evtl. Überprüfung meiner Dissertation durch eine Antiplagiat-Software zu.

Bei den von mir durchgeführten und in der Dissertation erwähnten Untersuchungen habe ich die Grundsätze guter wissenschaftlicher Praxis, wie sie in der „Satzung der Justus-Liebig-Universität Gießen zur Sicherung guter wissenschaftlicher Praxis" niedergelegt sind, eingehalten.

Gießen, 2016-04-04

_____
Christian Jesch